EPFL

Thèse n° 8407

A fast-moving Langmuir probe array for the divertor of the Tokamak à Configuration Variable

Présentée le 1er octobre 2021

Faculté des sciences de base
SPC - Physique des plasmas de bord
Programme doctoral en physique

pour l'obtention du grade de Docteur ès Sciences

par

Hugo DE OLIVEIRA

Acceptée sur proposition du jury

Prof. F. Mila, président du jury
Prof. C. G. Theiler, directeur de thèse
Dr D. F. Brunner, rapporteur
Dr J. P. Gunn, rapporteur
Prof. P. Ricci, rapporteur

École polytechnique fédérale de Lausanne

2021

Abstract

In next step tokamaks such as ITER and future fusion power plants, wall materials will be subjected to considerably higher heat and particle fluxes than in present-day machines. Maintaining plasma facing components in good condition and simultaneously assuring acceptable core performance will be an outstanding challenge. This situation is further complicated by the fact that extrapolations towards future tokamaks are difficult and the mechanisms governing transport of energy and particles are still being investigated. Proper diagnostic coverage of the boundary plasma of currently operational machines is therefore crucial.
In the Tokamak à Configuration Variable (TCV), wall-embedded Langmuir probes (LPs) are one of the most powerful diagnostics to describe local properties in the boundary region of the plasma. The present thesis work includes operation, maintenance and upgrades of this LP system. In particular, the TCV wall probe coverage has been extended from 114 to 194 probes. Furthermore, a new set of amplifiers has been installed, featuring a number of improvements, including protection against amplifier damage from transient plasma events.
In parallel, a novel fast probe array, the Reciprocating Divertor Probe Array (RDPA), has been designed, built and commissioned at TCV, providing unprecedented Langmuir probe measurements across the divertor volume. In contrast to reciprocating probes accessing the divertor region of other major tokamaks, the RDPA provides $2D$ measurements in a single reciprocation, enabled by a radial array of Mach probe tips moved vertically across an extended region of the divertor volume. The probe has been already operated reliably for more than 200 experiments. The physics results are consistent with other reference diagnostics (electron Thomson scattering upstream and wall embedded Langmuir probes downstream) for most plasma conditions, showing that the design is sufficiently compact to provide measurements representative of the unperturbed plasma parameters.
The RDPA capabilities have allowed for a detailed particle balance study in the outer TCV divertor in attached and detached conditions and both with and without the recently installed divertor baffles. It has been observed that the contribution of the $E \times B$ drift to the poloidal ion flux is comparable and sometimes larger than that due to the ion flux parallel to the magnetic field. The observation of upward parallel flux in the downward $E \times B$ region near the target further illustrates the important role of $E \times B$ flows in attached conditions. Except for strongly detached conditions, most of the particle flux arriving at the outer target is shown to be due to ionization along the outer divertor leg, justifying the 'closed-box approximation'

frequently used in detachment models and previously inferred on TCV from spectroscopic measurements. Likewise, the presence of the baffles results in a substantial increase of the divertor ionisation level.
$E \times B$ drifts also play an important role in terms of heat transport, as found from a divertor heat flux balance study in attached conditions. Together with parallel heat conduction, the ExB-convected heat flux dominates the poloidal heat flux, while parallel heat convection plays a lesser role in the example studied.
A new feature of RDPA is also to provide detailed, local measurements of fluctuation characteristics across the divertor volume of TCV, thanks to acquisition frequencies of up to 2 MHz. The first findings include the development of a strong poloidal gradient of the density fluctuation level, observed towards the onset of detachment, and the surprising presence of high fluctuation levels in the narrow region of downward $E \times B$ (on the high-field side of the peak electron temperature) for well attached reversed field discharges. Ongoing efforts focus on using RDPA results to validate the global 3D two-fluid code GBS in diverted TCV simulations and thus helping to improve its predictive capabilities.

Résumé

Dans les futurs tokamaks comme ITER et DEMO, les matériaux en contact avec le plasma seront soumis à des flux de chaleur et de particules considérablement plus élevés que dans les machines actuelles. Garantir le bon état des parois et assurer simultanément des performances acceptables pour le cœur du plasma est un défi majeur qui devra être considéré pour rendre possible la production d'énergie de fusion. Le comportement du plasma pour les futurs tokamaks est difficile à prévoir en se basant sur les expériences faites dans les machines actuelles et les mécanismes régissant le transport de l'énergie et des particules sont encore à l'étude. Une couverture complète du plasma avec des diagnostics appropriés est donc cruciale pour faire progresser la recherche sur les machines existantes.

Dans le Tokamak à Configuration Variable (TCV), les sondes de Langmuir (LP) sont parmi les diagnostics les plus utilisés pour décrire les propriétés locales du plasma dans la région du bord. Le présent travail de thèse comprend l'exploitation, la maintenance et la mise à jour de ce système. La couverture des sondes murales TCV a été étendue de 114 à 194. De plus, un nouvel ensemble d'amplificateurs a été installé, comportant un certain nombre d'améliorations, avec une protection renforcée contre les dommages dus aux événements transitoires du plasma.

En parallèle, une nouvelle sonde rapide, la Reciprocating divergeur Probe Array (RDPA), a été conçue, construite et mise en service sur TCV, fournissant des mesures Langmuir inédites dans le divergeur. Contrairement aux sondes rapides installées dans le divergeur des autres tokamaks principaux, la RDPA fournit des mesures 2D en un seul mouvement de va-et-vient, grâce à une batterie de 24 sondes distribuées radialement (organisées en une configuration 'Mach') qui se déplace verticalement à travers le divergeur. La sonde a fonctionné de manière consistante pour plus de 200 expériences. Les résultats physiques sont cohérents avec d'autres diagnostics de référence (diffusion Thomson pour le plasma en amont et sondes de Langmuir pour le plasma en aval) pour la plupart des conditions de plasma, montrant ainsi que la RDPA est suffisamment compacte pour fournir des mesures représentatives des paramètres du plasma non perturbé.

Les capacités de la RDPA ont permis une étude détaillée sur le bilan des flux de particules dans des conditions attachées et détachées, avec et sans les déflecteurs récemment installés dans le divergeur. Il a été observé que la contribution de la dérive néoclassique $E \times B$ au flux ionique poloïdal total est comparable et parfois plus importante que celle due au flux ionique parallèle

au champ magnétique. L'observation d'un flux parallèle ascendant dans la région descendante de la dérive $E \times B$ près du sol de TCV illustre le rôle dominant du flux $E \times B$ dans des conditions attachées. La majeure partie du flux de particules arrivant au sol est due à l'ionisation le long de la jambe externe du divergeur, ce qui justifie " l'approximation de boîte fermée " pour le divergeur, fréquemment utilisée dans les modèles de détachement et précédemment déduite sur TCV à partir de mesures spectroscopiques. De plus, la présence des déflecteurs entraîne une augmentation sensible du niveau d'ionisation dans le divergeur.
La dérive $E \times B$ joue également un rôle important en termes de transport de chaleur, comme le montre une étude sur le bilan du flux thermique dans le divergeur en conditions attachées sur TCV. La conduction thermique parallèle et la convection $E \times B$ dominent le flux thermique poloïdal tandis que la convection thermique parallèle joue un rôle moindre dans l'exemple étudié.
Une autre fonctionnalité de RDPA est de fournir des mesures locales détaillées des fluctuations du plasma à travers le divergeur de TCV, grâce à des fréquences d'acquisition allant jusqu'à 2 MHz. Les principaux résultats comprennent le développement d'un fort gradient poloïdal du niveau de fluctuation en densité, observé pendant la transition vers un plasma détaché, et la présence surprenante d'une région avec un niveau de fluctuation élevé dans la région étroite où la dérive $E \times B$ est dirigée vers le bas (sur le côté haut-champ du pic de température des électrons) dans le cas d'une décharge attachée. Plusieurs études en cours se concentrent sur l'utilisation des résultats de RDPA pour valider le code 3D à deux fluides GBS avec des simulations du divergeur de TCV et pour ainsi améliorer ses capacités de prédiction.

List of acronyms

DT	Deuterium Tritium
DSS	Divertor Spectroscopy System
DEMO	Demonstration Power Plant
ELM	Edge-Localised-Mode
FIR	Far Infra-Red interferometer
GBS	Global Braginskii Solver
H-mode	High confinement mode
HFS	High Field Side
IR	Infrared thermography
ITER	International Thermonuclear Experimental Reactor
L-mode	Low confinement mode
LCFS	Last Closed Flux Surface
LFS	Low Field Side
LPs	Langmuir Probes
LSN	Lower Single Null
MANTIS	Multispectral Advanced Narrowband Tokamak Imaging System
OMP	Outer Mid Plane
RDPA	Reciprocating Divertor Probe Array
RPTCV	Reciprocating Langmuir Probe for TCV
SOL	Scrape-Off-Layer
SPC	Swiss Plasma Center
TCV	Tokamak à Configuration Variable
TS	Thomson scattering

Contents

Abstract i

Résumé iii

List of acronyms v

1 Introduction 1
- 1.1 Increasing world energy demand . . . 1
- 1.2 Problems and limitations from current energy sources . . . 2
  - 1.2.1 Fossil fuels . . . 2
  - 1.2.2 Controllable renewable energies . . . 2
  - 1.2.3 Intermittent renewable energies . . . 2
  - 1.2.4 Nuclear fission . . . 3
- 1.3 Thermonuclear fusion . . . 4
  - 1.3.1 Fusion reactions . . . 4
  - 1.3.2 The DT fusion reaction . . . 5
  - 1.3.3 Confinement methods . . . 6
  - 1.3.4 The fusion reactor concept . . . 9
  - 1.3.5 The impact of nuclear fusion on modern society . . . 11
- 1.4 The heat exhaust challenge . . . 12
  - 1.4.1 Limitations from the materials used in plasma facing components . . . 12
  - 1.4.2 Geometrical consideration for the heat exhaust in diverted plasmas . . . 13
  - 1.4.3 Divertor cooling strategies . . . 15
  - 1.4.4 Concept of detachment . . . 17
- 1.5 The TCV tokamak . . . 17
- 1.6 Review of diagnostics relevant for heat exhaust studies . . . 18
  - 1.6.1 Wall embedded Langmuir probes . . . 18
  - 1.6.2 Fast scanning Langmuir probes . . . 18
  - 1.6.3 Infrared camera . . . 19
  - 1.6.4 Neutral pressure gauges . . . 19
  - 1.6.5 Divertor Thomson electron scattering . . . 19
  - 1.6.6 Line integrated spectrometer . . . 20
  - 1.6.7 Multi spectral tangential imaging . . . 20
  - 1.6.8 Bolometry . . . 20

1.7 Motivations and outline of the thesis 20

2 The wall-embedded Langmuir probe system at TCV and recent enhancements 23
2.1 Physical principles involved in Langmuir probe analysis 23
2.1.1 The plasma sheath 24
2.1.2 Ion and electron contributions to the sheath heat flux 24
2.1.3 The Bohm velocity 25
2.1.4 The ion saturation current measurement 26
2.1.5 Sweeping of the bias voltage for single Langmuir probe 26
2.1.6 TCV wall embedded LP system 27
2.2 Overview of the recent amplifier upgrade 27
2.3 Design of the Langmuir probes and characteristics of the transmission line . . 28
2.4 Design of the amplifier circuitry 33
2.4.1 Requirements 35
2.4.2 Power supplies 36
2.4.3 Amplification 36
2.4.4 Potential and current measurement system 37
2.4.5 Current limitation system 39
2.5 Protection against amplifier damage 40
2.5.1 Attempt to prevent amplifier damage with fuses 40
2.5.2 Attempt to prevent amplifier damage with surge protectors 41
2.5.3 Preventing amplifier damage by increasing the transmission line inductance 42
2.5.4 Preventing amplifier damage by decreasing the effective power supply capacitance 43
2.6 Possible future improvement to the current measurement system 44
2.7 Analysis routines 45
2.8 Inter-ELM analysis routines for H-mode studies 46
2.9 Conclusion 49

3 Design, construction and commissioning of the Reciprocating Divertor Probe Array (RPDA) 51
3.1 Overview of existing reciprocating divertor probes and probe arrays 51
3.2 Short presentation of RDPA 52
3.3 Main design constraints 53
3.3.1 Probe tip requirements for ion saturation and Mach number measurements 54
3.3.2 Bandwidth requirements 54
3.3.3 Spatial coverage requirements 55
3.3.4 Minimizing plasma perturbations: probe shadow and recycling 56
3.3.5 Minimizing impurity release and material erosion 57
3.3.6 Ensuring probe integrity during off normal events 59
3.3.7 Various external constraints 61

3.4 Probe design . . . 62
3.4.1 Probe head design . . . 62
3.4.2 Out-of-vessel mechanical structure and vacuum assembly . . . 68
3.4.3 Motion system . . . 69
3.4.4 Transmission lines . . . 70
3.5 Example results . . . 71
3.6 Future hardware improvements and theoretical models requirements . . . 74
3.6.1 Asymmetric floating potential and asymmetric electrical current drawn with grounded probes: an opportunity for an interpretative model ? . . . 74
3.6.2 Challenging interpretation of the electron pressure profile differences between RDPA and Thomson and a possible hardware improvement to isolate the effect of recycling on the probe body. . . . 76
3.7 Conclusion . . . 78

4 Particle balance in the TCV divertor **79**
4.1 SOL and divertor dynamics expected in TCV . . . 79
4.2 Experimental setup . . . 82
4.3 Parallel and ExB flow calculations with RDPA . . . 84
4.3.1 Parallel flow and ion flux measurements . . . 85
4.3.2 Measurement of ExB particle fluxes . . . 87
4.4 Divertor particle balance . . . 90
4.4.1 The influence of core density on the divertor particle balance . . . 90
4.4.2 The influence of core density on the divertor particle balance in the presence of baffles . . . 93
4.4.3 The effect of baffles for a given core density . . . 95
4.5 Conclusion . . . 96

5 Insights on the competition of conductive and convective heat fluxes in the TCV divertor **97**
5.1 Procedure for heat flux calculations . . . 97
5.2 Heat flux profiles . . . 98
5.3 Conclusion . . . 100

6 Insights on divertor fluctuations **103**
6.1 Procedure for the calculations of the RDPA density fluctuations measurement . 103
6.2 Effect of baffles and core density on fluctuation levels . . . 104
6.3 Ongoing contributions to turbulence code validation studies . . . 106
6.4 Conclusion and future work . . . 107

7 Conclusion **111**

A Appendix: RDPA user manual **115**
A.1 RDPA disassembly in TCV . . . 115

A.2 RDPA disassembly in the vacuum workshop 117
A.3 RDPA assembly in the vacuum workshop 118
A.4 RDPA assembly in TCV 121
A.5 Components relevant to RDPA operation 121
A.6 Software 122

Bibliography **125**

Acknowledgements **139**

Remerciements **141**

Curriculum Vitae **143**

1 Introduction

1.1 Increasing world energy demand

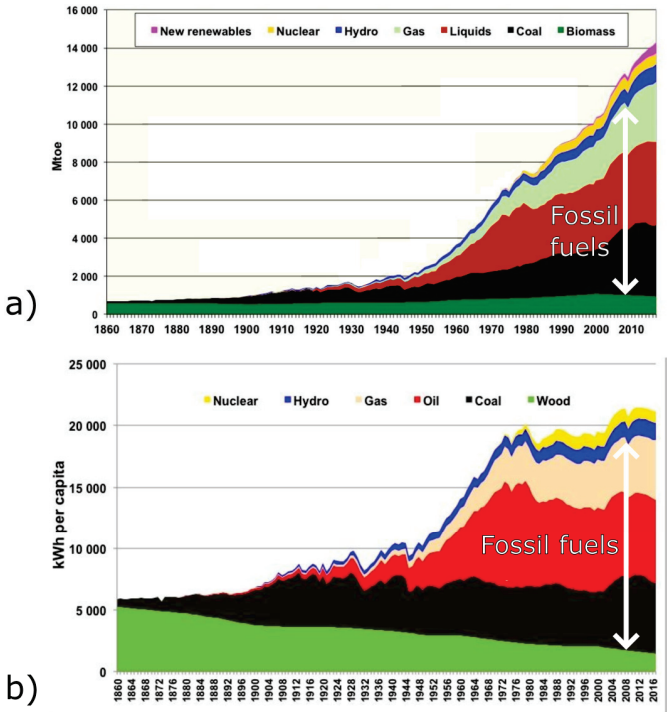

Figure 1.1: **a)** Historical world energy consumption 1860-2017 [1] and **b)** energy consumption per person, world average 1860-2017 [1]. *Mtoe* stands for Million Tonnes of Oil Equivalent.

There has been a strong increase in the world energy consumption from 1900 to 2010, see FIG. 1.1 **a)**. This trend is the combination of the increase in world population, as well as the increase in energy consumed per person, see FIG. 1.1 **b)**. In the strict physical sense, energy is not 'consumed', but rather converted from a concentrated state such as chemical energy into more diffuse states such as heat.

1.2 Problems and limitations from current energy sources

Humanity has shifted its energy use from the most readily available energy (wood) before the industrial revolution to a broader mix of sources, see FIG. 1.1 **a)**. Interestingly the modern energy sources are not replacing the historical sources but have been instead added to them. Both historical and modern energy sources have their own limitations and problems, as briefly discussed in the following.

1.2.1 Fossil fuels

The vast majority of the current energy mix comes from fossil fuels made of carbon rich molecules (oil, natural gas and coal), see FIG. 1.1 **a)**. Fossil fuels are problematic: they are responsible for the strong increase in atmospheric CO_2 concentration and can possibly lead to fierce competition and tension between the different consumers once the reserves are diminishing. The increase in the CO_2 concentration, from 280 ppm before the industrial revolution to 400 ppm in 2017 [2], has been shown to be responsible for negative effects to the environment such as global warming [2] and ocean acidification [3].

1.2.2 Controllable renewable energies

'Controllable' renewable energy sources, such as biomass, geothermal energy, hydroelectricity and tidal energy continuously deliver a predictable quantity of energy throughout the year. Their main disadvantage is that their capacity does not manage to follow the increasing energy demand because they rely on a a limited pool of specific sites. In the case of biomass (wood, ethanol, plant oil) a major increase in the production could lead to deforestation. Geothermal energy for house heating can be an attractive solution to mitigate seasonal temperature variation. However, extraction of high temperature steam to produce geothermal electricity is difficult because of the poor heat conductivity of the ground over large distances. Geothermal electricity can be cost competitive in a few specific locations such as in Iceland, near the rift in continental plates. In the case of hydroelectricity, most of the river sites in wild mountainous regions have been already occupied in industrialised countries and the realisation of new projects has been less frequent in recent years [4]. The suitable coast lines in shallow waters necessary for tidal energy are rare and potential improvements in tidal energy are much more limited than for conventional hydroelectricity.

1.2.3 Intermittent renewable energies

Intermittent renewable energy such as wind, photovoltaic, concentrated solar power and direct solar heating do not suffer from a limited pool of specific locations and could potentially grow with the energy demand. Their drawback, in contrast to controllable renewable energy sources, is their intermittent character. Modern society is used to spending energy when it is needed rather than when it is available. Balancing the grid becomes increasingly difficult

as the fraction of the intermittent energy grows [5] without any storage system providing the adequate capacity.

Energy storage has been historically done with pumped-storage hydroelectricity which can be cost competitive with fossil fuels [6]. However, as mentioned in SEC. 1.2.2, available sites for hydroelectricity are limited on the planet.

Some modern storage solutions are currently investigated such as battery storage (lithium ion battery, flow battery), thermal storage (concentrated solar power), synthetic fuels (hydrogen, synthetic natural gas, synthetic ammonia), compressed air and mechanical storage (flywheel, gravity storage). So far these solutions are not cost competitive with fossil fuels and remain strongly dependent on favourable policy environments [7]. Energy storage on a daily basis is believed to be feasible in the near future. However, seasonal energy storage will be an outstanding challenge to address.

1.2.4 Nuclear fission

Nuclear energy is exempt from some of the concerns discussed for the other energy sources, such as CO_2 emissions and intermittency. However, nuclear energy comes with its own set of challenges:

1) The nuclear fuel reserves are limited with the current reactor technology and the nuclear park should be replaced on the long term. Indeed the reserves strongly depend on the reactor technology being employed: only ≈ 90 years for the estimated ^{235}U land reserves with the current nuclear power installed [8] [9], using conventional water cooled reactors, and a much longer time, ≈ 12700 years, if the ^{238}U reserves are used with fast neutron breeder reactors [10] or CANDU breeder reactors [8]. Indeed ^{235}U represents only 0.7 % of natural uranium while ^{238}U represents 99.3 % of the total. ^{232}Th is another candidate fuel for nuclear fission breeder reactors but has not been included in this introduction because the Th reserves are currently less accurately evaluated than the uranium reserves.

2) Nuclear fission reactions produce long lived radioactive waste (plutonium, actinides). Their re-treatment in a breeder reactor would increase the overall cost of electricity and therefore underground waste storage is the currently used solution [11]. Nuclear energy can be unpopular among the public opinion in some countries, mainly due to the fear of the long term nuclear waste. For instance, Germany is currently phasing out nuclear energy [12]. The public perception of the nuclear waste problem is sometimes disproportionate due to a lack of readily available information on the issue.

3) A catastrophic runaway event can breach the containment building of the reactor and lead to the release of radioactive matter into the environment, e.g. the Chernobyl disaster. However, modern reactor designs (second generation and beyond) with thick reinforced concrete containment buildings are much safer in this regard [13] and nuclear energy is actually a relatively safe way of generating electricity with less causalities caused per unit of

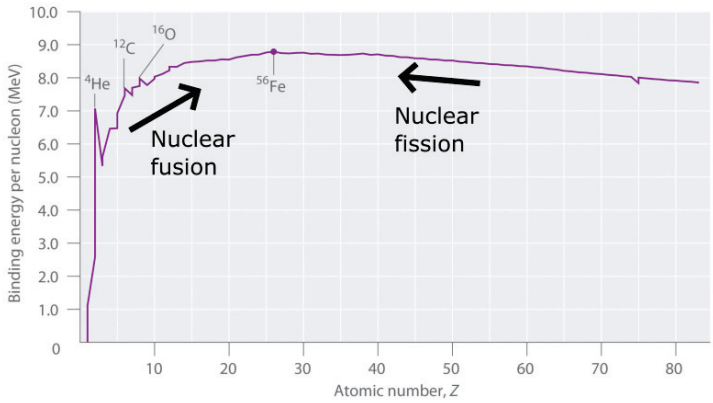

Figure 1.2: Binding energy per nucleon for the most stable isotopes of each elements [16].

energy produced than fossil fuels (mining, air pollution) or even hydroelectricity (dam failure).

4) Nuclear engineering knowledge and facilities can help in the process of creating a nuclear bomb. Indeed, the ^{235}U enrichment process required for conventional water cooled fission reactor employs the same technology as the enrichment process necessary for high ^{235}U content weapon grade fuel [14]. Consequently, nuclear power technologies are hardly transferred to developing nations, limiting the wide adoption of nuclear power.

1.3 Thermonuclear fusion

Thermonuclear fusion, the energy powering the stars, was proposed for the first time in 1920 as a potential source of energy for humanity by Arthur Eddington: *"A star is drawing on some vast reservoir of energy by means unknown to us. This reservoir can scarcely be other than the subatomic energy which, it is known exists abundantly in all matter; we sometimes dream that man will one day learn how to release it and use it for his service. The store is well nigh inexhaustible, if only it could be tapped."* [15].

In this section, we will introduce basic fusion concepts, discuss the different confinement schemes with a focus on magnetic confinement, the most promising confinement solution, and finally briefly introduce the future perspectives for fusion by comparison with the current nuclear fission industry.

1.3.1 Fusion reactions

All the nuclei found in the universe originate from one of the first stable particles from the primordial universe, the proton. The succession of nuclear reactions leading to the creation of the second most lightweight element, helium, is called the ¨Proton–proton chain reaction¨. Lightweight nuclei gain energy from fusion reactions and the reaction is said to be 'exothermic'. Fusion reactions leading to the formation of heavy elements beyond iron are 'endothermic',

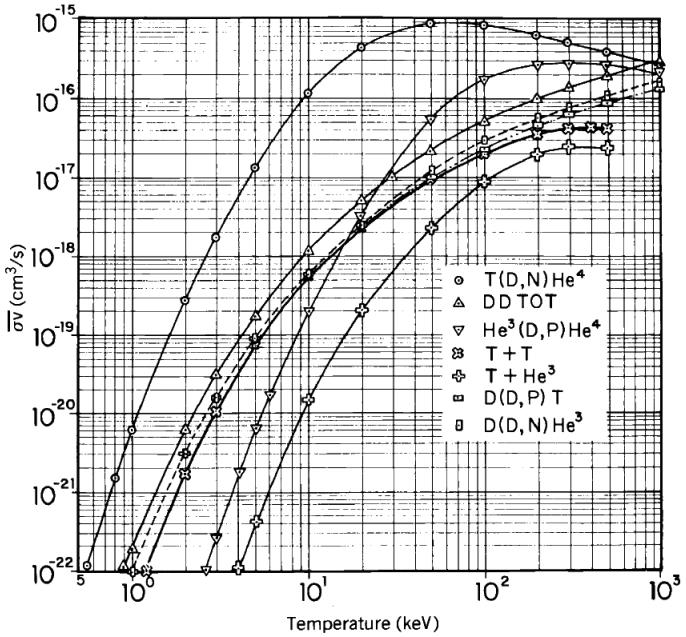

Figure 1.3: Values of the reactivity coefficient averaged over a Maxwell-Boltzmann energy distribution for various fusion reactions [17].

necessitating an energy input, see FIG. 1.2. This can be explained because the attractive nuclear strong interaction between protons and neutrons acts on a shorter distance than the coulomb repulsion and therefore is relatively less important in large nuclei. Fusion reactions only occur at high temperatures $> 1\ keV$ because of the coulomb repulsion between nuclei: particles require high kinetic energy to overcome the coulomb potential in order to attain the short distance necessary for the strong nuclear interaction to dominate. At these high temperatures $> 1\ keV$, electrons and nuclei are separated from each other and the matter is said to be in a ¨plasma¨ state.

1.3.2 The DT fusion reaction

Although many different fusion reactions are possible within the immense pressure found in the core of some stars, scientists are mostly interested in the DT (Deuterium Tritium) fusion reaction to generate a substantial amount of power. Indeed, the reactivity coefficient for this reaction is much higher than for the other reactions over a broad range of temperature, see FIG. 1.3: the reactivity of the DT reaction is ≈ 100 times higher than its competitors in the relevant temperature range $0\ keV < T < 50\ keV$. The formula for the DT reaction is [17]:

$$ {}^2_1D + {}^3_1T \rightarrow {}^4_2He(3.5\ MeV) + {}^1_0n(14.1\ MeV). \tag{1.1} $$

${}^4_2He$ products are also called α particles and are useful to heat the plasma and thus to sustain the fusion reaction. The fusion power per unit volume in a DT plasma, 50 % deuterium and 50 % tritium, scales with the plasma density squared and a reactivity coefficient $\langle \sigma v \rangle$ has been

introduced to describe the temperature dependence [18]:

$$P = \frac{1}{4} n^2 \langle \sigma v \rangle E, \tag{1.2}$$

where $E = 17.6\ MeV$ is the total energy released per DT reaction.

1.3.3 Confinement methods

A hot plasma does not hold together by itself and a force is necessary to oppose the plasma pressure. Sustained fusion energy must rely on a confinement scheme in order to succeed.

Gravitational confinement fusion is the process maintaining the plasma pressure in the stars. Interestingly, the gravitational confinement of the stars is not perfect. Indeed, in the case of the sun, stellar winds (fast particles) are able to separate from the sun surface and travel throughout the solar system. Gravitational confinement fusion is obviously considered to be impossible to recreate on earth.

Inertial confinement fusion

Inertial confinement fusion has been the first successful confinement scheme: fusion energy has been released in large quantities by mankind for the first time in 1952 with the detonation of the "Ivy Mike" US bomb [19]. Thermonuclear bombs are triggered with a nuclear fission runaway reaction that assures that the temperature in the vicinity of the explosion stays high enough during a sufficient time for fusion reactions to occur. A shield placed around the fusion fuel improves the confinement of particles and radiation in the first phase of the explosion. The heated volume expands, loses energy through radiation and the fusion reaction is stopped. There has not been any power plant built relying on the frequent triggering of a nuclear bomb so far, probably because it is impossible to design a containment building that can store both heat and radioactive particles even for the smallest bomb that can be built.

Another inertial confinement design relies on the use of lasers that concentrate the energy during a short pulse onto a small DT pellet. The record performance for such a design was achieved at the National Ignition Facility (NIF) [20] where a fusion power of 60 kJ was released while the pellet absorbed 100 kJ of external power. The actual electrical power required by the experiment systems is much larger than 100 kJ, because the process that converts electrical energy into laser light is highly inefficient. A high frequency of pellet explosions, 100 Hz, would only generate $\approx 60\ kJ \times 100\ Hz = 6\ MW$ with NIF explosion power levels. Therefore, even if the power gain of this process would permit net electricity production, the largest challenge for this design would remain: all the reaction products should be cleared and the new pellet installed in a fraction of a second for the next laser pulse to occur in the perfect conditions [20].

Magnetic confinement fusion

Finally, the last confinement scheme experimented so far is magnetic confinement. Beyond a certain temperature, matter is ionised, forming a gas of electrically charged particles (electrons and nuclei) called a plasma. These plasma particles interact with the ambient magnetic field through the Lorentz force. The Lorentz force is perpendicular to the velocity of the particles and they undergo helicoidal orbit along the magnetic field lines. The magnetic field can therefore be used as a tool to control the particles trajectories and to separate the plasma from the reactor walls.

It was quickly understood that in the case of straight magnetic field lines, most of the energy is lost at the walls at the extremities of the system due to the parallel velocity (parallel to the magnetic field vector) of the particles. A possible solution is to bend field lines into a loop in order for the particles to circle the machine indefinitely. The created magnetic volume has a torus shape. Scientists tried to build a first toroidal confinement machine prototype as early as 1938 [21].

The coils needed to generate a toroidal magnetic field are necessarily closer to each other near the center than at the periphery of the machine and the toroidal magnetic field is, therefore, higher near the center. The toroidal magnetic field is proportional to the inverse of the major radius according to the law $\nabla \cdot B = 0$:

$$|B(R)| = \frac{B_0 R_0}{R}, \tag{1.3}$$

where B_0 is the magnetic field at the major radius R_0. The change in magnetic field strength is sometimes used to name the different regions of the magnetic volume: the High Field Side (HFS), near the center of the machine and the Low Field Side (LFS) near the periphery of the machine.

This gradient in magnetic field is problematic for the confinement of the plasma because it is responsible for a vertical drift, see FIG. 1.4. The electron ∇B drift motion is directed in the opposite direction to the ion motion, creating a local vertical electrical field. The consequence is an outward radial $E \times B$ drift for both ions and electrons, leading to a rapid loss of particles to the walls.

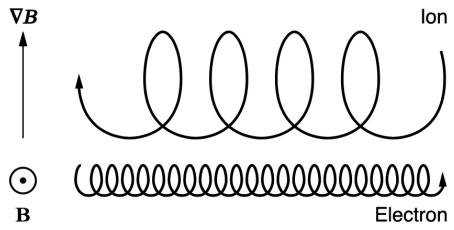

Figure 1.4: Illustration of the ∇B drift [22].

In 1951, Lyman Spitzer found a brilliant idea to solve the ∇B drift problem: the stellarator

concept, see FIG. 1.5. The field lines are twisted by the arrangement of the toroidal field coils (with a poloidal component). The twist is chosen to create a complete poloidal rotation of the field lines that cancel the net effect of drifts after a poloidal revolution. The drift effect in the vertical direction is directed away from the starting field line for half of the poloidal revolution and towards the initial field line for the remaining half. Interestingly, this poloidal revolution does not need to be completed within a single toroidal revolution but can be achieved over several toroidal revolutions.

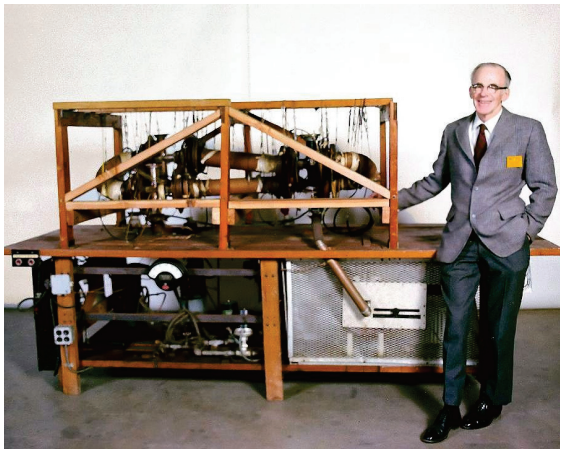

Figure 1.5: Lyman Spitzer in 1953 in front of the "Model A" stellarator at the Princeton Plasma Physics Laboratory [23].

The stellarator design represented a huge step in the history of magnetic confinement, but another design would soon revolutionize the field. Later in the 1950s, Andrei Sakharov and Igor Tamm introduced a new concept [20]: the tokamak (Toroidalnaya Kamera Magnitnaya, toroidal magnetic chamber in Russian). In the tokamak design, the poloidal rotation of the magnetic field line is provided by a toroidal electrical current carried by the plasma itself. This electrical current can be driven with external current sources, such as radio waves, or inductively, using a central primary coil, the inner poloidal field coil shown in FIG. 1.6. Outer poloidal field coils, shown in FIG. 1.6, are used to control the plasma position and shape in the poloidal plane.

After several years of improvements and various prototypes, the tokamak design became extremely efficient with the milestone of $T = 1\ keV$ being reached with the $T-3$ machine in 1968 [20]. Since the first Russian designs, tokamaks have dominated the competition in terms of confinement time and plasma pressure by an order of magnitude. As discussed later in SEC. 1.3.4 and FIG. 1.7, it is the product of these quantities that needs to be sufficiently high in order to attain sustained fusion energy.

A large part of the fusion community effort in the past 15 years has been invested in the construction of the largest tokamak to date, ITER [25], which is expected to deliver its first plasma in 2025 and first burning DT plasma in 2035. It is currently anticipated by the majority of the scientific community that a reactor design would then resemble the ITER project [26].

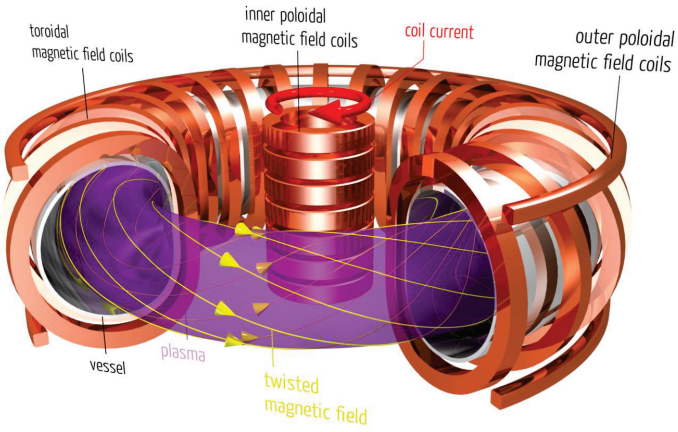

Figure 1.6: Schematic view of a tokamak [24].

This DEMOnstration reactor (DEMO) will need to be larger and/or have a stronger magnetic field in order to produce more fusion power and to be less dependent on external heating systems.

1.3.4 The fusion reactor concept

Net electricity production and the concept of ignition

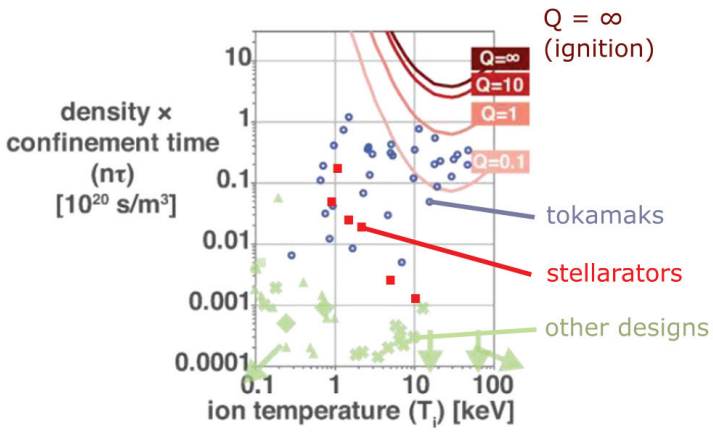

Figure 1.7: Product of the density and confinement time plotted as a function of ion temperature for the key magnetic confinement experiments performed [27].

A fusion reactor must produce more energy than it consumes in order to produce a net quantity of electricity. Since both external plasma heating systems (electron/ion cyclotron resonance heating, neutral beam heating, etc...) and electricity production systems (electric turbine) have limited conversion efficiencies, a reactor must have a power ratio $Q = P_{fusion}/P_{in} > 20$ in order to produce a sufficient amount of electricity [28]. The plasma heating should be ensured by α heating for the major part. If the reaction no longer relies on external heating

and is entirely sustained by α heating, the plasma is said to 'ignite'. A plasma state close to ignition $Q = P_{fusion}/P_{in} = \infty$ is therefore mandatory for fusion energy production.

In order to determine the plasma properties necessary to reach ignition, the confinement time concept can be introduced, which, in stationary condition is given by:

$$\tau = \frac{W}{P_{in}} = \frac{\int 3nTdV}{P_\alpha + P_{ext}}, \tag{1.4}$$

where $P_{in} = P_\alpha + P_{ext}$ is the sum of the power absorbed by the plasma from α particles and external heating sources and $W = \int 3nTdv$ is the thermal energy in a plasma where $T = T_e = T_i$ and $n = n_e = n_i$ are assumed.

In order to sustain the fusion reaction with minimal external energy input, a high confinement time is necessary in order to satisfy the power balance. The power balance equation is:

$$P_{in} > P_{out} \Leftrightarrow P_\alpha + P_{ext} > \frac{W}{\tau}. \tag{1.5}$$

Let us introduce the formula for the power from alpha particles P_α and assume that the plasma pressure is constant throughout the plasma volume, while neglecting P_{ext}. The condition for ignition then becomes [18]:

$$\frac{1}{4}n^2\langle\sigma v\rangle E_\alpha V > \frac{3nTV}{\tau} \tag{1.6}$$

$$n\tau > \frac{12T}{\langle\sigma v\rangle E_\alpha} \tag{1.7}$$

The reactivity coefficient is assumed to be proportional to the square of the temperature in the reactor relevant temperature range $10-20\ keV$ [18]:

$$\langle\sigma v\rangle = 1.1\cdot 10^{24}\ T^2 m^3 s^{-1}, \tag{1.8}$$

Further numerical application with $E_\alpha = 3.5\ MeV$ enables us to find the final criterion for ignition which is the product of ion density, temperature, and energy confinement time, also called the triple product:

$$nT\tau > 3\cdot 10^{21} m^{-3} keV s. \tag{1.9}$$

The product of density and confinement time as a function of the ion temperature for several key fusion experiments performed so far is shown in FIG. 1.7. The highest triple products attained are therefore located in the top right of this graph. It can be seen in this figure that tokamaks went close to $Q = 1$. Interestingly, the ITER planned reference at $Q = 10$ is not far from the ignition requirement $Q = \infty$.

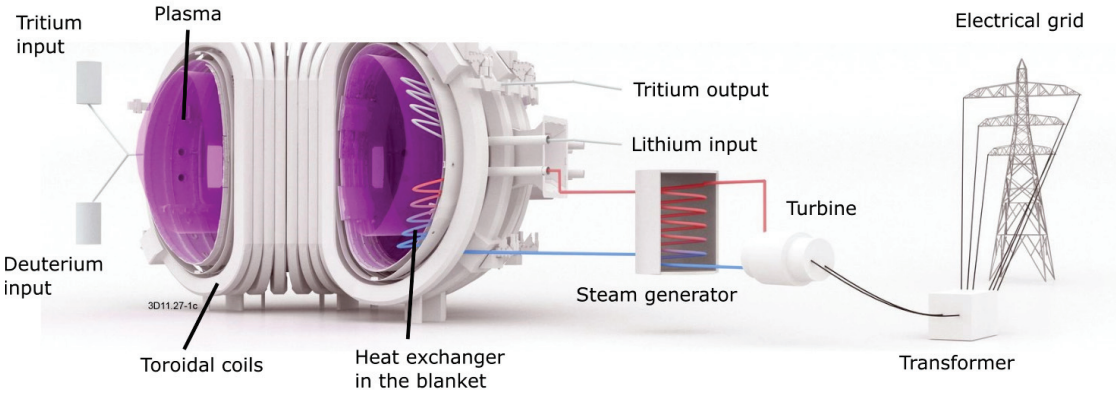

Figure 1.8: Scheme showing the most important components of a nuclear fusion reactor. Labels have been added onto the original figure [29].

Fusion power plant components

A nuclear fusion power plant does not only include the tokamak and the plasma. A long list of external systems is required such as a breeding blanket, a tritium plant, a cryogenic plant, a steam generator, a cooling tower, a turbine and a transformer. A simplified scheme represents how these systems are interconnected in FIG. 1.8.

1.3.5 The impact of nuclear fusion on modern society

The promise of nuclear fusion energy ?

Fusion is sometimes advertised as the energy of the future in public media [30]. Public communication is important for increasing interest and investments in fusion research to drive progress towards a possible reactor design.

However, the promise of nuclear fusion energy can also convey the idea that the unsustainable and increasing energy demand of modern society will be fulfilled by nuclear fusion, therefore reducing the incentive for a prompt reduction in the current energy consumption levels.

The fusion community should therefore try to find the right balance between securing enough funds to make scientific progress and avoiding the creation of false illusions among the public audience, that does not necessarily possess the technical competency to apprehend the outstanding difficulties involved in the realisation of a fusion reactor.

Advantages compared to nuclear fission ?

The advantages of fusion frequently mentioned [30] [25] are: a reduced risk of a catastrophic events, a reduced production of radioactive waste and abundant fuel reserves.

While these advantages when compared to nuclear fission will certainly become relevant on the long term, mentioning them implies that nuclear fission is a high-risk source of energy, producing dangerous waste and whose fuel supply is limited. While these implied statements are irrefutable, as discussed in SEC. 1.2.4, they might overshadow the larger problems caused by the other energy sources such as fossil fuels, see SEC. 1.2.1.

1.4 The heat exhaust challenge

At the time of writing, it is still unclear if the plasma facing components can withstand the steady state heat flux expected in a fusion reactor and the transient power loading for more than several seconds [31]. Experiments and simulations are continuously improved in order to strengthen the boundary plasma physics knowledge to design the most adequate heat exhaust system for future reactors. Improvements on the engineering design of plasma facing components are limited because of the intrinsic limits from material, see SEC. 1.4.1. The divertor concept and considerations on the effect of magnetic geometry on the heat exhaust are presented in SEC. 1.4.2. Finally some strategies employed to maximise divertor cooling are presented in SEC. 1.4.3 and the concept of detachment is discussed in SEC. 1.4.4.

1.4.1 Limitations from the materials used in plasma facing components

Tungsten is the candidate material for plasma facing components in future reactors such as ITER (International Thermonuclear Experimental Reactor) [32] and DEMO (DEMOnstration Power Station) [31] due to several intrinsic qualities such as a low tritium retention, a short half life for the radioactive products created upon neutron activation, the highest melting point of any known solid, a high thermal conductivity and a high resistance towards both physical and chemical sputtering. However, this material has some drawbacks such as a brittle behaviour, a high cost and the difficulty to make complex shapes. The maximum perpendicular steady state heat flux tolerated with water cooled tungsten mono-block is expected to be $\approx 16\ MW/m^2$ [32] for the ITER design.

Graphite is also extensively used as a plasma facing component in tokamak research [33] [34] due to an excellent thermal conductivity, absence of melting point, high sublimation temperature and simple machinability. Graphite was excluded from the ITER design [32] because of the high chemical affinity between hydrogen isotopes (tritium and deuterium) and carbon atoms which would produce unacceptable amounts of radioactive tritium retention. Moreover the erosion rate due to chemical sputtering would be unacceptable in a reactor even at low plasma temperature $\approx 1\ eV$ (temperature close to the energy required for chemical reaction).

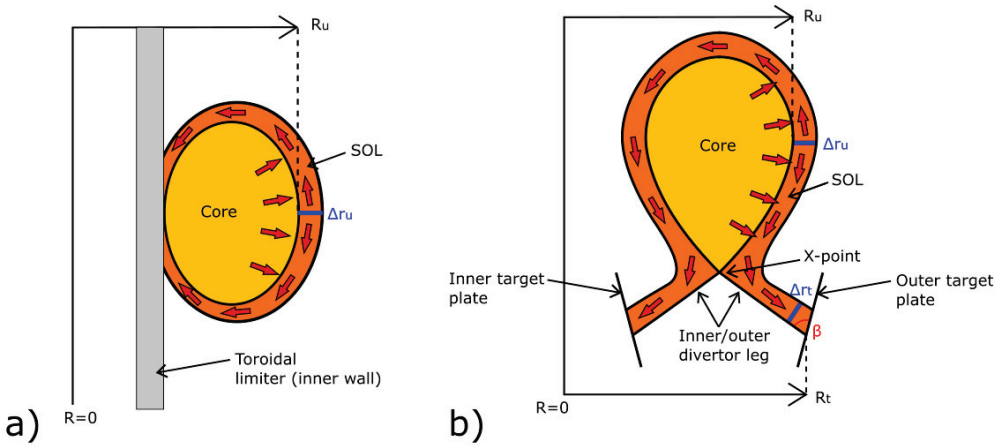

Figure 1.9: Scheme of the poloidal section in **a)** a limited plasma and **b)** a diverted plasma with two distinct regions, the core and the SOL, separated by the Last Closed Flux Surface (LCFS). Red arrows represent the direction of the main energy transport mechanisms: cross field transport from the core to the SOL and transport along the field lines from the upstream SOL to the targets.

1.4.2 Geometrical consideration for the heat exhaust in diverted plasmas

Historically, tokamaks had a limited plasma, see FIG.1.9 **a)**, where the last closed flux surface (LCFS) is in direct contact with the tokamak walls. Limited plasmas suffered from a feedback loop that prevented sufficient fusion power to be generated: once the core plasma power was increased, energetic particles in the SOL would cause increased sputtering of the wall materials and thereby cool down the core plasma through heavy impurities line radiation and reduce the fusion power through hydrogenic fuel dilution.

An ingenious solution to overcome the proximity between the core plasma and the plasma wetted areas was proposed for Stellarators by Lyman Spitzer in 1951 [35]: the divertor. In tokamaks, the divertor is created by a region of zero poloidal magnetic field, called an X-point, that defines the LCFS position. This X-point is obtained by driving an electrical current in the divertor field coil of approximatively the same magnitude and in the same direction as the plasma current. Electrical currents flowing in the same direction attract each other and therefore a subset of controllable poloidal field coils is required in order to stabilise the diverted plasma vertical motion, which adds some complexity as compared to a limited plasma tokamak.

In the diverted plasma, heat is continuously expelled from the core plasma into the Scrape-Off Layer (SOL), i.e. the region with "open" field-lines, through cross-field transport. In the SOL, this exhaust heat is then transported primarily along the magnetic field lines towards a relatively narrow width on the target plates, see FIG.1.9 **b)**.

Geometrical modifications of the magnetic equilibrium can be employed in the divertor region

(the region around and below the magnetic X-point) in order to reduce the peak heat flux. In the absence of volumetric power losses and cross-field heat transport in the divertor leg, the peak heat flux at the target can be written as [36]:

$$q^t_{\perp,peak} = \frac{P_{div}}{2\pi R_t \lambda_q} \frac{\sin\beta}{f_x}. \tag{1.10}$$

P_{div} is the power entering a single divertor leg, β is the angle of target tilting in the poloidal plane, R_t is the major radius at the target, λ_q is the radial e-folding length of the heat flux profile in the SOL at the outer mid-plane and f_x is the poloidal flux expansion defined as:

$$f_x = \frac{\Delta r^t}{\Delta r^u}, \tag{1.11}$$

where Δr^t and Δr^u are the perpendicular flux surface spacings at the target and upstream, see 1.9 **b)**.

From equation (1.10), it can be seen that both increasing f_x and decreasing β lead to a reduction of $q^t_{\perp,peak}$. The ratio $\frac{\sin\beta}{f_x}$ is proportional to $\tan\alpha$, with α the total grazing angle between the magnetic field and the divertor plate. Due to limited engineering precision, α is limited to ≈ 1 deg to 2 deg to avoid inhomogeneous heat flux deposition [36] and therefore, there is an upper bound for the heat flux reduction caused by wall tilt and flux expansion. Increasing R_t is another means to decrease $q^t_{\perp,peak}$ but is limited by the available space within toroidal field coils.

When applied to the ITER specifications, equation (1.10) yields an excessive peak heat flux at the target, about 20 times above the acceptable 10 MW/m^2 [36]. The $q^t_{\perp,peak}$ expected from the equation (1.10) is even larger for the generation of tokamaks beyond ITER, which will have a larger plasma volume and/or a higher magnetic field strength.

Additional reductions must therefore be achieved with the remaining parameters λ_q and P_{div} in equation (1.10). Increased cross-field transport will lead to larger λ_q. The turbulent spreading of heat along the divertor leg can often be described by a width S, the spreading factor, according to the Eich fitting procedure [37], and λ_q can then be replaced by $\lambda_q + 1.64S$ in equation (1.10). Since S is typically of the order of λ_q or smaller, the turbulent spreading effect is not sufficient in its own. P_{div} can be reduced by volumetric power/momentum losses such as impurity radiation, hydrogenic radiation, and charge exchange reactions. Besides reduced target heat fluxes, this results in a cooling of the divertor plasma and eventually pressure loss of the plasma near the target. In order to ensure adequate energy confinement and acceptable levels of plasma-wall interaction, one must therefore promote divertor geometries with both enhanced turbulent cross-field transport and increased volumetric losses.

1.4.3 Divertor cooling strategies

SOL physics is a complex interplay between heat transport channels, such as parallel electron conduction, parallel convection, $E \times B$ convection and turbulent cross field transport and volumetric losses such as ionisation, radiation and charge exchange reactions. Different strategies that can be pursued to enhance volumetric losses and to impede parallel heat transport channels are presented in this section.

Hydrogenic volumetric processes

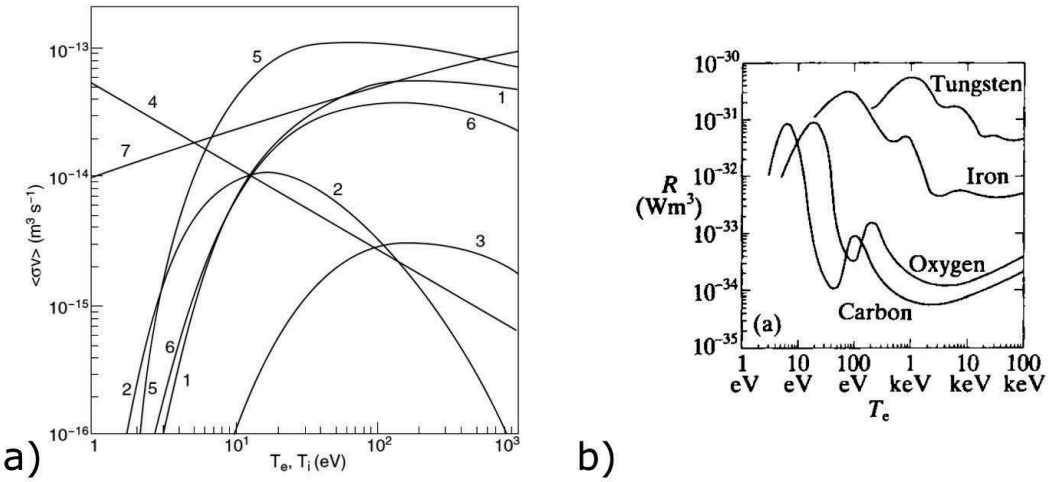

Figure 1.10: **a)** Rate coefficients for atomic and molecular hydrogen[38] and **b)** the radiation loss or power function R as a function of T_e for the elements C, O, Fe and W [38]. The numbered reactions in **a)** are **(1)**: $e + H_2 \rightarrow H_2^+ + 2e$, **(2)**: $e + H_2 \rightarrow 2H^0 + e$, **(3)**: $e + H_2 \rightarrow H^0 + H^+ + 2e$, **(4)**: $e + H_2^+ \rightarrow 2H^0$, **(5)**: $e + H_2^+ \rightarrow H^0 + H^+ + e$, **(6)**: $e + H^0 \rightarrow H^+ + 2e$, and charge exchange **(7)**: $H^0 + H^+ \rightarrow H^+ + H^0$.

The relative importances of some hydrogenic volumetric processes as a function of electron temperature are shown in FIG. 1.10 **a)** for a plasma in coronal equilibrium where $T_e = T_i$ is assumed. The rate coefficient for the various paths toward ionisation, **(1)**, **(3)** and **(6)** in FIG. 1.10 **a)** strongly increases with electron temperature for $T_e \approx 5\ eV$ and above. Interestingly the rate coefficient for charge exchange, **(7)** in FIG. 1.10, is higher than for ionisation processes over the entire temperature range. Recombination, a process that dominates only at very low temperatures $T_e < 1\ eV$, has not been shown in this plot.

Divertor fuelling and the density limit

Increasing the plasma density enables to increase the hydrogenic radiation and the rate of charge exchange reactions [38]. The local ion flux towards the divertor targets increases non linearly with the neutral fuelled flux. These ions recombine on the wall surfaces and travel back to the plasma as recycled neutral particles (single atoms or molecules). Once the

recycled neutral flux becomes much larger than the fuelled flux, the plasma is said to be in the high recycling regime. Above a certain fuelling rate, the plasma undergoes an edge radiative instability and disrupts [39], thereby setting an upper value for the amount of hydrogenic gas that can be fuelled. Note that the disruptive limit depends on other factors such as the impurity concentration.

Divertor geometry relative to the recycled neutrals

Increased neutral baffling can enhance volumetric losses in the SOL with little effect on the core plasma [40] [41]. The divertor plates can be inclined to redirect the neutrals from the relatively cold far SOL into the near SOL (near the LCFS). This configuration is called the vertical plate divertor and is the preferred choice for the most recently built large size tokamaks [40]. Advanced divertors, such as the snowflake, super-X, X-point target and double null plasmas are currently being investigated in medium sized tokamaks [36] [42]. These alternatives could enable stronger neutral confinement and higher volumetric losses than the vertical plate divertor design, albeit at potentially higher costs.

Impurity seeding

Above $\approx 10\ eV$, hydrogenic particles are almost entirely ionised and generate negligible volumetric losses. Another process, such as impurity radiation, is then required to drive the SOL towards a higher collisionality state where the hydrogenic volumetric losses can be activated.

Impurity radiation from low atomic number elements such as carbon, nitrogen and neon is one of the most promising tools to dissipate a substantial fraction of the power in the relevant reactor upstream SOL temperature range [38]. By chance, these lightweight impurities are fully ionised in the core region and generate negligible amounts of line radiation above a certain critical temperature, see FIG. 1.10 **b)**. Hydrogenic nuclear fuel dilution in the core can however become an issue at high impurity fraction [38].

Impurity transport is a complex process: the core impurity fraction does not necessary scale with the SOL impurity fraction. The divertor geometry is supposed to enhance the ratio of impurity concentration in the divertor SOL to that in the upstream SOL thanks to the friction with the main hydrogenic ion species which is streaming towards the walls near the divertor plates [43]. However, friction with the main ion specie is not necessarily the most important force acting on impurity ion [43], leading to possible impurity transport from the edge to the core plasma.

1.4.4 Concept of detachment

¨Detachment¨ is often referred to as the last stage of the divertor cooling process. Detached divertor regimes are experimentally characterized by large radiation losses and a “roll-over” of plasma flux to the targets [44] [38] [45]. The transition to detachment is correlated with a decrease in the electron temperature near the target and with a shift of the ionisation and impurity radiation fronts towards the X-point region [46]. Although a high level of detachment would be the ideal state for the divertor plasma in a fusion reactor, the potential cooling of the edge plasma would not be necessarily compatible with the best performing core confinement scenario. Therefore, the optimal operational point for a reactor in terms of divertor wall protection and core performance is still to be determined.

1.5 The TCV tokamak

The Tokamak à Configuration Variable (TCV) [47] at EPFL is a medium size machine with a major radius $R_0 = 0.88\ m$, toroidal magnetic field $B_0 \leq 1.5\ T$ and plasma current $I_p \leq 1\ MA$.

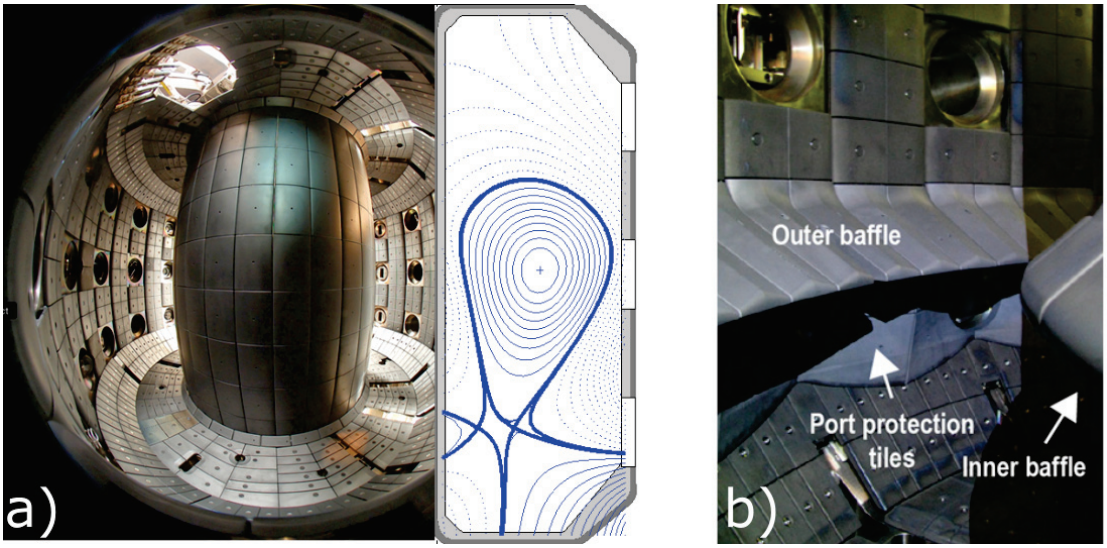

Figure 1.11: **a)** Picture of the TCV vacuum vessel covered with graphite tiles with a superimposed poloidal cross section with an advanced magnetic equilibrium (a snowflake 'minus' HFS plasma) shown as an example and **b)** recent baffles upgrade featuring an increased divertor closure [41] [48].

A picture taken inside the vacuum vessel highlights the full graphite tile wall coverage, see FIG. 1.11 **a)**. An advanced divertor magnetic equilibrium is superimposed to the real picture to illustrate an example of the TCV magnetic shaping capabilities. Thanks to its 16 individually powered poloidal field coils, TCV is one of the few tokamaks in the world able to provide the necessary magnetic flexibility needed to test the efficiency of advanced divertor geometries. A substantial amount of pioneering work in edge physics has been performed over the past years [49] [36] [50].

The heat and particle exhaust characteristics of the TCV tokamak have been recently modified with a divertor upgrade [41] [48] where an in-vessel structure of solid graphite baffles forms a divertor chamber of increased closure in order to decouple divertor and main chamber regions, see FIG.1.11 **b)**. Alternation between a closed and open divertor can be performed in between experimental campaigns in order to isolate the effect of the baffles on results by repeating experiments [41].

1.6 Review of diagnostics relevant for heat exhaust studies

A large panoply of diagnostics are required in order to give the most complete and accurate description of the boundary plasma as possible, needed to improve our physics understanding of this critical region and to validate numerical models. A non exhaustive list of the most relevant diagnostics to the context of this thesis is given in this section.

1.6.1 Wall embedded Langmuir probes

Among the edge diagnostics, Langmuir probes (LPs) are one of the most common tools to describe local SOL/divertor properties. They typically provide measurements of ion saturation current I_{sat}, electron density n_e, electron temperature T_e, floating potential V_{fl}, plasma potential V_{pl} and ion Mach number M. In the single probe arrangement (local measurement of the plasma properties), I_{sat}, V_{fl} and M can be easily measured with high time response, e.g. $200kHz$. On the contrary, T_e, V_{pl} and n_e are usually obtained by relatively slowly sweeping the probe voltage, resulting in a time response of $\approx 100Hz$ [51]. With considerably more effort, it is possible to use custom electronics in order to increase the time response of T_e, V_{pl} and n_e up to the highest frequency of relevant SOL fluctuation, i.e. $\approx 1MHz$ [52]. LPs, essentially consisting of a conducting wire exposed to the plasma, can be conveniently installed within the plasma facing components. Such wall-embedded LPs then provide local measurements of plasma parameters near the wall.

More details on the physical principles involved in the Langmuir probe analysis will be given in SEC. 2.

1.6.2 Fast scanning Langmuir probes

In order to obtain LP measurements in regions more distant from the walls, Langmuir probes are mounted on reciprocating systems, undergoing a fast radial motion. Such systems are typically installed at the outer mid-plane, accessing a region from the wall to the LCFS [53] [54] [55] [56]. The upstream profiles are usually cross checked with electron Thomson scattering results. The measurements of fluctuations in the outer mid plane region is highly valuable to understand the turbulent cross field transport and its impact on the SOL width [57] [58] [53] [59].

The divertor and X-point region have also been diagnosed with fast reciprocating Langmuir probes, more details on this subject will be given in SEC. 3.1.

1.6.3 Infrared camera

Infrared thermography (IR) is extensively used to monitor the plasma facing component surface temperature with high spatial and temporal resolution. In TCV, the thermography system consists of a vertical and a horizontal infrared camera [60]. The vertical camera is mounted on the top of the machine and covers the outer strike point of a typical single null plasma. The camera is sensitive in the wavelength range 1.5 to 5.1 μm. The typical frame rate and spatial resolution are 400 Hz and 2.5 mm in full frame respectively. The frame rate can be increased to 15 kHz for a sub-frame. The THEODOR code is used to solve the heat diffusion equation using the measured temperature as a boundary condition [60]. IR analysis can be challenging, depending on the target surface condition: the redeposition of carbon rich residue on top of the graphite surface necessitates the introduction of a correction factor in the analysis.

1.6.4 Neutral pressure gauges

There are many different types of neutral pressure gauges. In TCV presently, the neutral pressure measurements are performed with magnetically shielded and vibrationally isolated baratron pressure gauges [36]. Three baratrons are presently installed on the outer wall (at $Z = 0\ m$), on the floor (at $R = 0.75\ m$) and on the 45° tiles on the LFS. The neutral pressure can be used as a proxy to determine if the SOL plasma is in high recycling conditions. The neutral pressure measurement is difficult to accurately translate into a neutral atomic and molecular density measurement because of the complex interactions between heated neutrals and the tokamak surfaces [61].

1.6.5 Divertor Thomson electron scattering

Thomson electron Scattering (TS) is one of the most important diagnostics in a tokamak. The measurement of electron density and electron temperature over the full plasma range is obtained by recording the spectrum from laser light scattered by electrons. The laser pulses have a negligible effect on the plasma which is an advantage over intrusive diagnostics such as fast scanning Langmuir probes for example. A divertor Thomson electron scattering system has been recently installed in TCV [62]. 20 new TS spectrometers have been installed to measure electron temperatures down to $\approx 1\ eV$ with vertical spatial resolution of $15-18\ mm$ at the same radial position as the core TS, $R = 0.9\ m$.

1.6.6 Line integrated spectrometer

High resolution spectrometers can be used to measure the emission lines from hydrogenic and impurity species. The measurement of the line width and intensity enables the estimation of important quantities such as the plasma density and ionisation and recombination rate. In TCV, the Divertor Spectroscopy System (DSS) consists of vertical and horizontal viewing systems, each employing 32 lines of sight with spatial resolution of $\approx 13\ mm$ [63]. The spectrometer contains a triple grating turret which can be turned to change the grating used and to change the wavelength region covered, e.g. to enable measuring different Balmer lines [63]. Although current analysis is performed with line average measurements, a future version of the diagnostic could include a tomographic reconstruction by combining the two viewing systems.

1.6.7 Multi spectral tangential imaging

Cameras are often mounted tangentially in order to produce a high quality video of the divertor plasma. The light can be spread in several channels mounted with different filters. The desired frequency range of the incoming light is chosen to correspond with the most interesting atomic lines. The spectral resolution is obviously much lower than for a typical line integrated spectrometer and therefore choosing the appropriate filter to deduce basic plasma quantity is challenging. In TCV, a 10-channel Multispectral Advanced Narrowband Tokamak Imaging System (MANTIS) is currently installed [64], based on a similar principle as its 4-camera, predecessor system [65]. MANTIS coverage includes the inner and the outer divertor legs as well as the X-point in most experiments.

1.6.8 Bolometry

Bolometry is one of the solutions that can be used to measure the total radiated power from the plasma, including both hydrogenic and impurity radiation over a large wavelength range. The radiated power density is estimated from the changes in the resistance of a thin electrically conducting foil whose surface is exposed to the plasma. The foil should behave ideally as a black body in order to absorb the complete spectrum of radiated power. In TCV, the total radiated power is presently measured using a 64 channel system based on metal foil resistor bolometers [66]. Tomographic reconstructions of the poloidal emissivity distribution are routinely performed with a spatial resolution of $\approx 4\ cm$ and a temporal resolution of $\approx 10\ ms$, limited by the integration time of the metallic resistor bolometers.

1.7 Motivations and outline of the thesis

Langmuir probes provide detailed profiles at the mid-plane and at the target in TCV, see FIG. 1.12 **a)** and **b)**. The region in between the upstream plasma and the plasma at the target

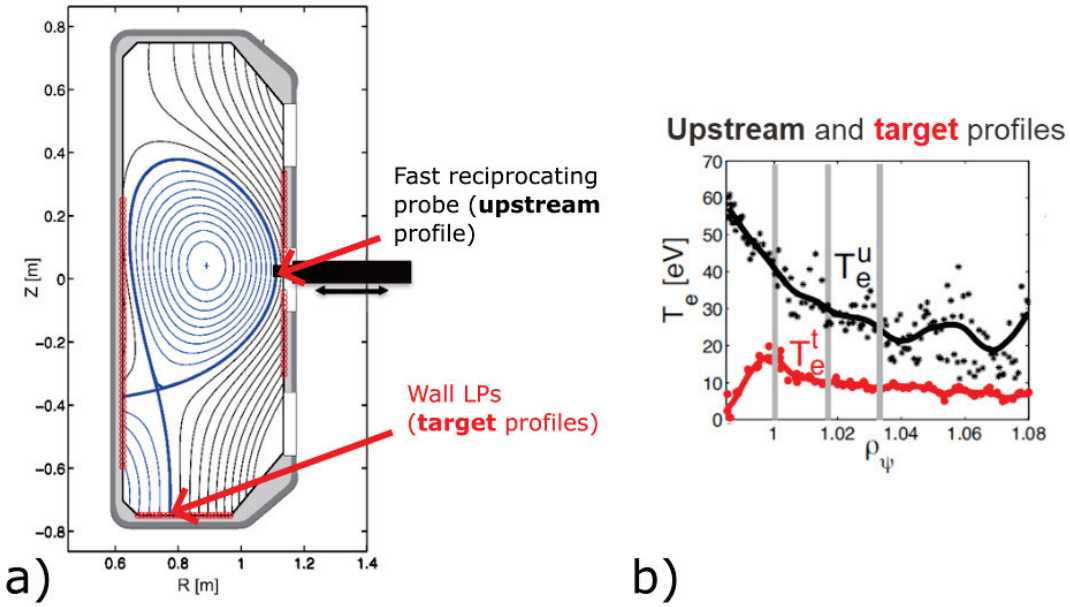

Figure 1.12: **a)** Poloidal cross section of the TCV tokamak with the Langmuir probe coverage and **b)** example of the difference between the electron temperature at the target and near the outer mid plane [36].

is not routinely diagnosed with Langmuir probes. Instead, this region is covered by other systems such as multispectral imaging [64], divertor electron Thomson scattering [62] and spectroscopic measurements [63]. However, these measurements differ in many aspects from the quantities obtained from Langmuir probes, e.g. different quantities measured and limited spatial and/or temporal resolution. In particular, these other diagnostics are not able to resolve the turbulent time scales.

In order to overcome this lack of probe coverage, the main focus of this thesis is to design and build a new probe diagnostic in the divertor of TCV, the fast-moving Reciprocating Divertor Langmuir Probe Array (RDPA). Unlike the $1D$ profiles given by the wall LPs and by the mid-plane reciprocating probe, the aim of RDPA is to provide $2D$ measurements of plasma quantities across a poloidal section of the divertor. Such a $2D$ probe scanning system has, to our knowledge, not been implemented in any major tokamak, which makes the RDPA project challenging and unique.

With the enhanced diagnostic capabilities provided by this new tool, the goal is to explore a number of key divertor plasma issues and to provide stringent benchmarks for numerical models. The main subjects of study where RDPA can provide unique insight include the particle and power balance in the divertor and in particular the assessment of the competition between parallel velocity and $E \times B$ drift velocity as a function of divertor regime, the spreading of heat and particle flux profiles along the divertor leg in different magnetic geometries, the spatial distribution of turbulence fluctuation levels in the divertor and the identification of the

nature of turbulence via cross-phase measurements between different quantities. In terms of code validation, such measurements can provide stringent tests for the models used both in edge transport codes such as SOLPS-ITER (a transport code that couples a multi-fluid solver with the kinetic Monte Carlo neutral code EIRENE [61]), and first-principles turbulence codes, such as the Global Braginskii Solver (GBS) code developed at the SPC [67]. Furthermore, the localised nature of LP measurements and the relatively large number of quantities obtained would allow a combination with the results from other divertor diagnostics, such as the multi-spectral imaging system (MANTIS) [64]), the divertor Thomson [62] and in particular the diagnostics relying on line-integrated measurements such as the Divertor Spectroscopy System (DSS) [63].

Some of these new possibilities opened up by the RDPA could already be explored within this thesis, others will be the subject of future work. The remainder of this thesis is organised as follows: Chapter 2 presents the TCV LP system in detail together with recent upgrades performed as part of this thesis. Chapter 3 discusses the RDPA diagnostic design, construction and commissioning. Chapter 4 presents divertor particle balance studies including detailed assessments of the role of parallel and $E \times B$ flows in different divertor regimes and in both baffled and non-baffled discharges. Chapter 5 covers the topic of heat flux profiles from both convection and conduction. Chapter 6 introduces the various fluctuation measurements that have been performed so far with RDPA. Finally the conclusions will be presented in Chapter 7.

2 The wall-embedded Langmuir probe system at TCV and recent enhancements

Part of the diagnostic responsibilities of this thesis work included the operation, maintenance, and upgrade of the TCV wall-embedded Langmuir probe system. This system, together with its recent upgrades, is presented in the following chapter. Some theoretical concepts required for Langmuir probe theory, their basic working principle and the system on TCV are briefly introduced in SEC. 2.1. An overview of an amplifier upgrade performed in 2018 is shown in SEC. 2.2, followed by a more in-depth description of the TCV wall-embedded LP design and the transmission lines connecting them to the amplifiers is presented in SEC. 2.3. The design of a new amplifier circuitry is presented in detail in SEC. 2.4, discussing in particular the amplification, the current limitation, and the voltage and current measurements circuit. Protection strategies against amplifier damage are discussed in SEC.2.5. A possible future improvement to the current measurement system is introduced SEC. 2.6. The Langmuir probe analysis routines are described in SEC. 2.7 and an introduction to inter-ELM analysis is given in SEC. 2.8. Finally, a summary of the chapter is presented in SEC. 2.9.

The following chapter content has been already partially published: SEC. 2.3, SEC. 2.4 and SEC. 2.5 are entirely based on the reference [68]. Co-authors of the paper have agreed to share the content for the chapter of this thesis.

2.1 Physical principles involved in Langmuir probe analysis

A Langmuir probe is a measurement apparatus made of an electrical conductor in contact with the plasma [69]. The electrical current passing through the probe depends on the probe voltage and on the local plasma properties. Some of the local plasma quantities can be experimentally deduced from the voltage and current measurements by using theoretical models [38] [70]. Applying a different voltage between a Langmuir probe and the neighbouring components in contact with the plasma requires an electrical insulation. In order to present the physical principles involved in Langmuir probe analysis, several concepts, related to the behaviour of

the plasma near a physical surface, need to be introduced first.

2.1.1 The plasma sheath

Hydrogenic ions, such as deuterium ions, are ≈ 3600 times heavier than electrons. In a sufficiently collisional plasma, the ion and electron distributions are close to thermal equilibrium $T_e \approx T_i$. In this case, the mean velocity of the electrons is $\approx \frac{\sqrt{m_i}}{\sqrt{m_e}} = 60$ times higher than the mean deuterium ion velocity. This velocity imbalance results in a somewhat counter intuitive process in the region where the plasma comes in contact with the wall: the formation of the plasma 'sheath', a narrow layer at the plasma-wall interface where quasi-neutrality is violated [38].

The plasma voltage increases relative to the wall voltage because the electron flux to the wall is initially larger than the ion flux. The resulting electric field is mostly confined in the sheath, whose dimension is equal to a few Debye lengths [38]. Indeed, the Debye length is the characteristic distance required for the plasma to screen an external charge [38]:

$$\lambda_{Debye} = \sqrt{\frac{\epsilon_0 T_e e}{n_e e^2}}, \tag{2.1}$$

where n_e is the plasma density, T_e is the electron temperature expressed in $[eV]$ rather than in $[J]$ and e is the elementary electron charge. Throughout this work, plasma temperatures are expressed in $[eV]$, which is why the multiplication with the elementary charge is required to obtain the correct numerical factor.

The charge equilibrium between the ion and the electron fluxes is attained once the plasma floats at $V_{sh} \approx +3T_e$ relative to the wall voltage for a deuterium plasma with $T_i = T_e$ and where secondary electron emission is absent [38]. The equilibrium between the plasma potential and the electrical current is attained on a short timescale, approximatively equal to the sheath dimension divided by the velocity of the electrons.

2.1.2 Ion and electron contributions to the sheath heat flux

Interestingly, the voltage drop across the sheath transfers energy from the electron population to the ion population. Let us consider the same deuterium plasma where $T \equiv T_i = T_e$ and where secondary electron emission is absent. If we neglect the energy deposited due to recombination at the target surface, the formula describing the different contributions to the *surface* heat flux according to the model described in [38], chapter 25.5 is:

$$q = q_e + q_i, \tag{2.2}$$

where q_e and q_i are the electron and ion contributions to the heat flux:

$$q_e = 2Te\Gamma_e, \tag{2.3}$$

$$q_i = (2.5T + V_{sh})e\Gamma_i \approx (2.5T + 3T)e\Gamma_i \approx 5.5Te\Gamma_i. \tag{2.4}$$

Γ_i and Γ_e are respectively the ion and the electron particle flux densities trough the sheath expressed in $[m^{-2}s^{-1}]$. In general, $\Gamma_i \approx \Gamma_e$ is respected in order to satisfy the overall charge balance. In this case the ion contribution is 5.5/2 times higher than the electron contribution to the total heat flux at the target. However, the assumption $\Gamma_i \approx \Gamma_e$ is not necessarily true locally in the presence of electrical currents that can be caused by drifts or thermal gradients [71]. In order to simplify the heat flux formula, the total sheath heat flux transmission factor γ_{sh} is usually introduced to account for both ion and electron contributions [38]. The expression of the target heat flux for the same plasma, as previously assumed, becomes:

$$q = \gamma_{sh}Te\Gamma_i = (\gamma_e + \gamma_i)Te\Gamma_i = (2 + 5.5)e\Gamma_i = 7.5Te\Gamma_i, \tag{2.5}$$

where γ_e and γ_i are respectively the electron and ion sheath heat transmission factors. The value of 7.5 is close to the experimental observations, e.g. $\gamma_{sh} \approx 6$ has been obtained from the comparison between Infrared thermography (IR) and LPs in TCV [72].

2.1.3 The Bohm velocity

In the presence of a wall, which acts as a particle sink, the plasma is strongly accelerated by the pressure gradient in a region of the plasma called the pre-sheath. The final ion velocity at the entrance of the sheath in many situations is equal to the plasma sound speed, the so-called Bohm velocity [38] [70]:

$$v_{se} = c_s = \sqrt{\frac{e(T_e + \gamma T_i)}{m_i}}, \tag{2.6}$$

where e is the elementary charge, T_e and T_i are the electron and ion temperature expressed in $[eV]$, m_i is the ion mass, and γ is the adiabatic index. $\gamma = 1$ is a default value, often used in previous TCV edge studies [51]. Since T_i is difficult to measure in the boundary plasma of tokamaks, the assumption that $T_i = T_e$ is also usually made [51]. It should be noted that in the presence of a magnetic field perpendicular to the wall, EQ. (2.6) remains unchanged. For small (but not too small) grazing angles between the magnetic field and the wall, another sheath forms on top of the Debye sheath, called the Chodura sheath or magnetic pre-sheath [73] [38] [74]. At the entrance to this sheath, the ions usually still satisfy the Bohm condition for their velocity parallel to the magnetic field. However, corrections to this velocity appear in case of spatial gradients of potential and pressure perpendicular to the magnetic field [38] [74].

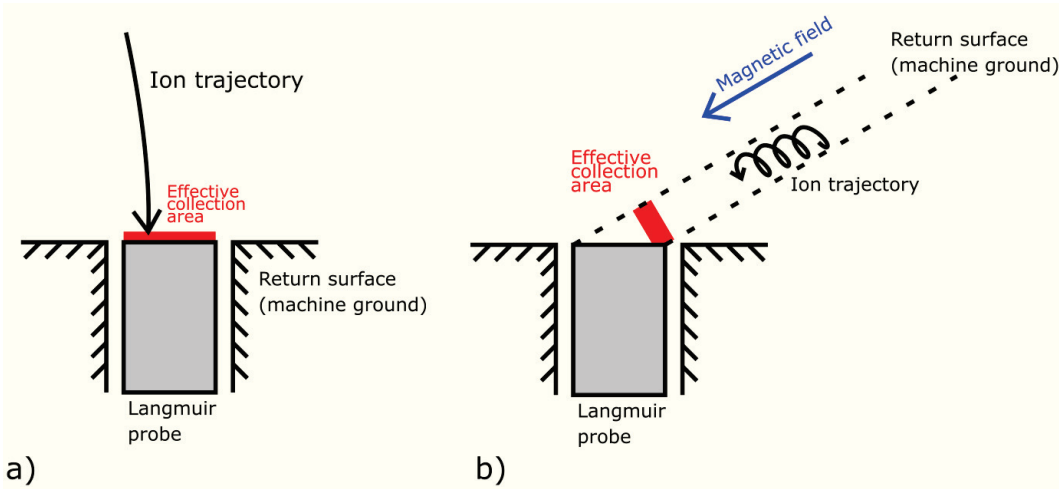

Figure 2.1: **a)** Langmuir probe facing an un-magnetised plasma and **b)** Langmuir probe facing a strongly magnetised plasma.

2.1.4 The ion saturation current measurement

Based on the Bohm condition, EQ. (2.6), we can deduce what a Langmuir probe will measure in case it is biased to a highly negative potential. The resulting change in voltage between the plasma and the Langmuir probe is taken up almost entirely by the probe sheath [38]. The highly negative bias voltage will repel the entire electron population such that essentially only ions are collected by the probe. The Bohm condition still remains valid in these conditions and the resulting probe current, called ion-saturation current, can be expressed as [38]:

$$I_{sat} = n_{e,se} e c_s S, \tag{2.7}$$

where $n_{e,se}$ is the electron density at the entrance of the sheath and S is the effective ion collection area of the probe. The later is reduced in the case of a magnetised plasma, see FIG. 2.1, because of the Lorentz force which limits ion trajectories perpendicular to the magnetic field. The ion saturation current is therefore equivalent to the ion flux in 'normal' conditions, i.e. when the probe voltage is referenced to ground. The heath flux formula can be expressed as a function of the ion saturation current density $J_{sat} = I_{sat}/S$:

$$q = \gamma_{sh} T e \Gamma_i = \gamma_{sh} T J_{sat} \tag{2.8}$$

2.1.5 Sweeping of the bias voltage for single Langmuir probe

Changing gradually the bias voltage of the probe from a negative value (ion saturation) to a positive value (electron saturation) enables to record the so called 'IV curve', characteristic of the local plasma conditions. The IV curve recorded with conventional electronics can not resolve the plasma characteristics at the turbulence time scale, because high frequency

sweeping with large voltage extrema poses many technical difficulties. A four parameters equation [75] [51] can be used to describe how the current flowing to the probe changes as a function of the bias voltage:

$$I_{pr} = I_{sat}\left[1 + \alpha(V_{pr} - V_{fl}) - e^{\frac{V_{pr}-V_{fl}}{T_e}}\right], \tag{2.9}$$

where V_{fl} is the potential at which there is no net current drawn from the plasma, α is a coefficient taking into account the increase in the effective ion collection area with voltage in the ion saturation domain due to sheath expansion, T_e is the electron temperature expressed in eV and I_{sat} corresponds to the ion current drawn at $V_{pr} = V_{fl}$. In the case of probe tips with relatively small ion collection area, e.g. flush probes, the parameter α is mandatory for the interpretation of measurements. It is less critical in the case of proud probes with a sufficiently large effective area. Once the electron temperature is determined, the plasma density at the sheath edge is obtained by combining the I_{sat} measurement with the Bohm condition:

$$n_{e,se} = \frac{I_{sat}}{ec_sS} \approx \frac{I_{sat}}{e\sqrt{\frac{2eT_e}{m_i}}S} \tag{2.10}$$

Moreover, the plasma potential can be deduced from the combination of the electron temperature measurement and from the floating potential measurement, as explained in SEC. 2.1.1:

$$V_{pl} \approx V_{fl} + 3T_e \tag{2.11}$$

2.1.6 TCV wall embedded LP system

There exist many different Langmuir probe types such as single probes, double probes, triple probes and mirror probes [52]. The wall-embedded LP system in TCV consists of 194 single probes with voltage sweeping capabilities thanks to a total of 216 dedicated amplifiers. The typical acquisition frequency for the voltage and current measurements is 200 kHz. The bias voltage is usually swept from -110 V up to 80 V at a frequency of 900 Hz. The system and its recent upgrades are presented in SEC. 2.2, SEC. 2.3, SEC. 2.4 and SEC. 2.5. The analysis routines and some example results are presented in SEC. 2.7 and SEC. 2.8.

2.2 Overview of the recent amplifier upgrade

A new amplifier circuitry to operate single LPs on TCV with an arbitrary bias-waveform or in floating potential mode has been recently developed at TCV [68]. Compared to the first generation of custom-built amplifiers, the new circuitry features an improved amplification final stage with simpler and cheaper components, an improved current measurement and a custom current limitation system based on suspended OP-amps. 180 of these third generation amplifiers have been built and tested in 2018, extending the total number of amplifier from 48 to 228 units. Before 2018, a limited number of probes could be connected at the same time,

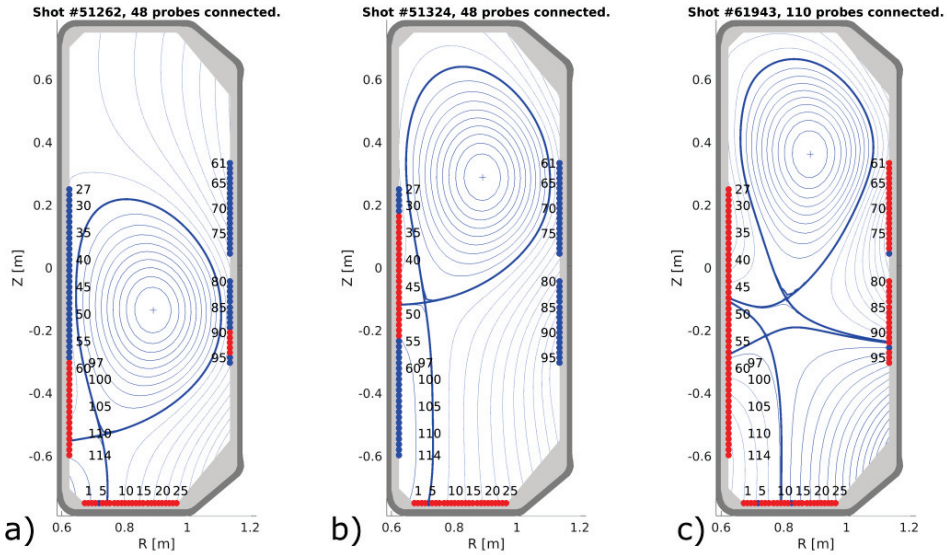

Figure 2.2: Poloidal cross-section of TCV with the location of the 114 Langmuir probe tips prior to the 2019 upgrade. Red dots indicate LPs connected to an amplifier, blue dots are LPs that are not acquired. Before the 2018 electronics upgrade, the amplifiers needed to be re-wired manually to accommodate the different plasma shapes and positions as shown in **a)** for the shot #51262 and in **b)** for the shot #51324. After the 2018 electronics upgrade, e.g. in **c)**, shot #61943, full coverage is attained.

see FIG. 2.2 **a)** and **b)**. In 2019, the number of Langmuir probes has been increased from 114 to 194 [68] in the frame of the TCV divertor upgrade [48]. The electronics upgrade allows the simultaneous operation of all the 194 wall-embedded single LPs currently installed on TCV as shown in FIG 2.3, and thus substantially improves the operational flexibility.

2.3 Design of the Langmuir probes and characteristics of the transmission line

Langmuir probes have been present in TCV since 1992 [76]. They have evolved over time and only the most recent design is presented here. The first details of the spatial location of installed probes have been given in 2003 [77]. The different probe tip geometries used in TCV are shown in FIG. 2.4. Domed probes represent the majority of the installed tips. They are preferred over flush probes due to several practical reasons: reduced sheath expansion, less relative error on the height of the probe tips and better signal to noise ratio for grazing magnetic field line angles $\alpha \approx 0°$. The greater erosion rate of domed probes is, however, a disadvantage and replacement of eroded probes is sometimes required after an experimental campaign.

The probe assembly is housed in the TCV polycrystalline graphite tiles which armor the main

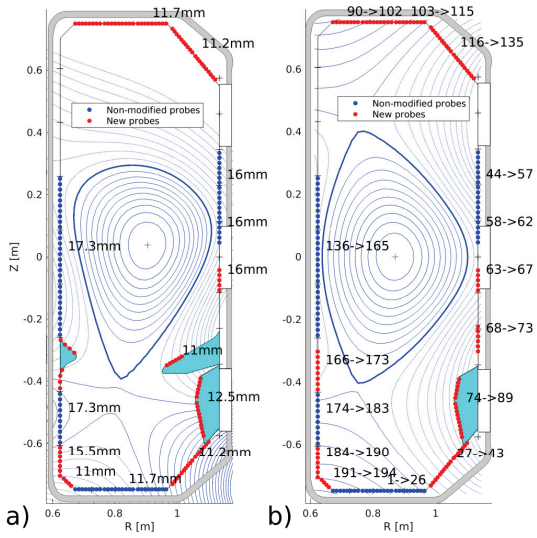

Figure 2.3: 2019 Langmuir probe coverage upgrade [68]. The average distance in between probe tips is displayed for the upgrade with the first version of the baffles installed in 2019 in **a)** and the probe numbering is shown for the upgrade without baffles for the 2020 campaign in **b)**.

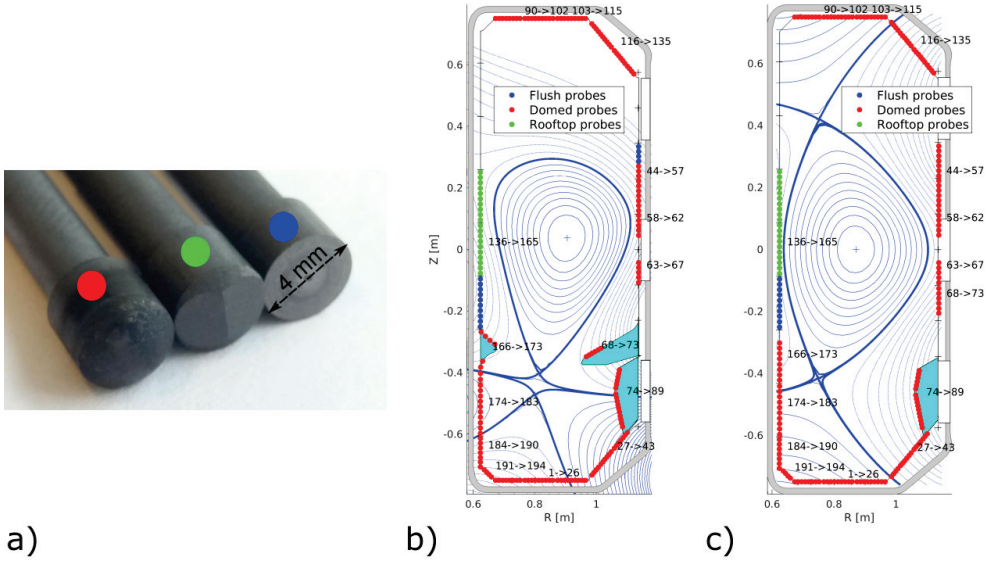

Figure 2.4: **a)** Picture of the different probe heads installed in TCV: dome-shaped head (red), rooftop (green) and flush (blue), **b)** probe types installed for the first version of the baffles installed in 2019 and **c)** for the upgrade without baffles during the 2020 campaign.

wall and the divertor, as shown in FIG. 2.5. Electrical contact is provided by nickel based alloy springs ($R \approx 1\ \Omega$) positioned between the inner conductor of the mineral insulated coaxial

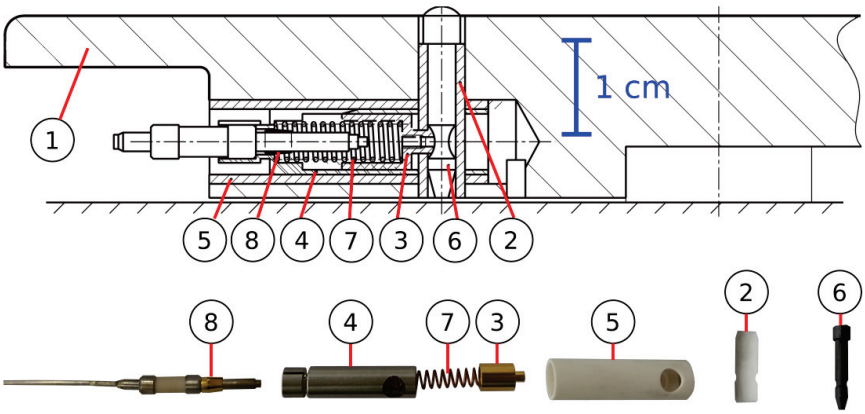

Figure 2.5: Cross-sectional view of the probe assembly and photos of the individual components labelled [68]: ① Graphite tile housing ② Vertical aluminum nitride electrical insulation tube ③ Gold coated copper beryllium finger electrical contact ④ Stainless steel housing for the cable inner conductor (end of the Thermocoax® cable) ⑤ Horizontal aluminum nitride electrical insulation tube ⑥ Graphite probe tip ⑦ Nickel based alloy spring and ⑧ Gold coated copper beryllium contactor (tiny ring mounted onto the cable inner conductor).

cable 1 $Zs\ Ac$ 10 from the company Thermocoax® and the probe tips are manufactured in polycrystalline graphite SGL® Sigrafine $R6650$. The springs used to be made out of copper beryllium alloy with high electrical conductivity ($R \approx 0.1\ \Omega$) and were later discarded: some springs lost their shape because of the annealing process happening at high temperatures. The measured electrical resistance of the assembly ($R \approx 0.5\ \Omega$) is often lower than the resistance of the nickel based alloy springs because the current can find a direct path from the stainless steel housing ④ in FIG. 2.5 to the copper beryllium finger electrical contact ③ in FIG. 2.5. If the current goes through the nickel based alloy spring, the electrical resistance of the assembly is $\approx 1.4\ \Omega$. Adding copper springs in parallel with the nickel based alloy springs and electrodeposition of copper on top of the nickel based alloy springs are possible solutions considered for future installations in order to reduce the electrical resistance of this component. The mechanical link between the probe tips and the assembly is assured by the same spring.

Probe tip maintenance requires the tiles to be unfastened and taken out of the machine, as illustrated in FIG. 2.6 **a)**. The ease of replacement, thanks to the spring assembly, is important to minimize the downtime during manned entries in TCV. Langmuir probe tips need to be replaced when the erosion is large enough to reduce their projected area along the magnetic field. Furthermore, it was observed during the 2019 opening that a resistive layer has been deposited on most probe tip surfaces. The contact resistance measured with round-shaped electrodes is high ($R_{contact} \approx 100\ \Omega$) when the voltage applied is within $\pm 1.7\ V$ and then suddenly drops ($R_{contact} \approx 0.6\ \Omega$) once the applied voltage is larger than $\pm 1.7\ V$, showing variable resistance behavior. It is difficult to evaluate the effective resistance as seen by the plasma, probably an order of magnitude lower than the measured contact resistance because

of the larger contact area wetted by the plasma. Such resistive layers can affect the evaluation of the electron temperature [51], particularly in the case of low electron temperature and high density, where the most important part of the IV curve is found in a limited voltage range. It is believed that both carbon redeposition and boronisation play a role in their formation. The resistive layer is supposedly very thin since a gentle sanding with a scouring pad enabled to recover both proper electrical conductance and dull appearance. High heat flux from the plasma can have the same effect as sanding: eroded probes frequently found in the near scrape-off-layer have the characteristic dull appearance from pure graphite and show negligible contact resistance.

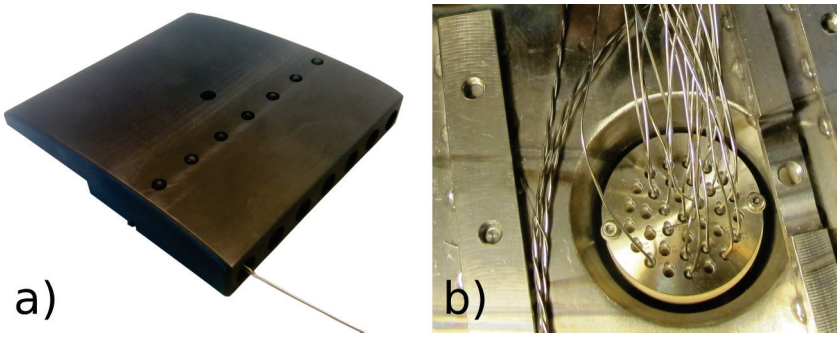

Figure 2.6: Langmuir probe tile **a)** ready for installation with a single Thermocoax® cable connected to the first probe for illustration and vacuum feed-through **b)** seen from inside the tokamak vessel after the protective tiles have been removed.

Specific care is required when making the Thermocoax® cable termination in order to ensure ultra-high vacuum (UHV) compatibility and proper electrical connection. The magnesium oxide ceramic powder electrical insulation in the Thermocoax® cable acts as a moisture reservoir and therefore the cables must be oven dried before the connectors are brazed to seal the cable terminations. Moisture is problematic because the magnesium oxide powder becomes slightly electrically conductive when exposed to the ambient humidity level. The electrical insulation must be tested with +250 V DC voltage to verify if the resistance across the inner conductor and the shield of the cable is sufficiently high, i.e. at least 100 $M\Omega$.

The length of the Thermocoax® cables between probe tips and vacuum feedthroughs, see FIG. 2.6 **b)**, is typically $\approx 2m$. The vacuum feedthroughs are special units from the Kurt J. Lesker Company® . They are mounted on $DN63\ CF$ vacuum flanges. Each unit carries a maximum of 35 conductors. Electrical contact is provided by male pins embedded into the ceramic body of the feedthroughs and by specific female copper contactors that are brazed onto the inner conductor of the Thermocoax® cables.

The in-vessel transmission line is then followed with $\approx 20\ m$ of 19 twisted pairs Mueller® cables, connecting the vacuum feedthroughs with the Langmuir probe electronics cubicle. Each probe conductor from the vacuum feedthrough is connected to both conductors of each twisted pair in the Mueller® cable in order to minimize the line resistance. The advantage of

twisted pairs is lost by using both conductors to carry the same signal but the high frequency properties are maintained thanks to the individual grounded screens wrapped around each pair. Each of the 19 pairs Mueller® cable carries a maximum of 19 signals.

The overall capacitances of the transmission lines have been measured directly at 10 kHz and 100 kHz and the values are found between $C_{line} = 3.5\ nF$ and $C_{line} = 6\ nF$ depending on the line. These measurements are consistent with measurements on spare Thermocoax® cables $C_{Thermocoax} = 0.61\ nFm^{-1}$ and on twisted pairs from spare Mueller® cables $C_{Mueller} = 0.19\ nFm^{-1}$.

The overall resistances and inductances of the entire lines have not been measured directly. Estimates are given here based on measurements done on spare cables:

- The overall resistance is estimated to be $R_{line} \approx 1.3\ \Omega$, given the measured DC resistance $\approx 0.5\ \Omega$ of the probe assembly shown in FIG. 2.5 connected to a 2 m long Thermocoax® cable and given the measured resistance per unit length of a twisted pair from the Mueller® cable $R_{Mueller} \approx 0.04\ \Omega m^{-1}$. The resistance of the Thermocoax® is included in the $\approx 0.5\ \Omega$ value. In the scenario where nickel based alloy springs are taken into account as explained earlier, the overall resistance is estimated to be $R_{line} \approx 2.2\ \Omega$.
- The overall inductance of the line is estimated to be $L_{line} \approx 15.4\ \mu H$, given the measured inductance per unit length of the Thermocoax® cable $L_{Thermocoax} = 0.7\ \mu Hm^{-1}$ and the measured inductance per unit length of a twisted pair from the Mueller® cable $L_{Mueller} \approx 0.7\ \mu Hm^{-1}$ (measurements performed at 100 kHz).

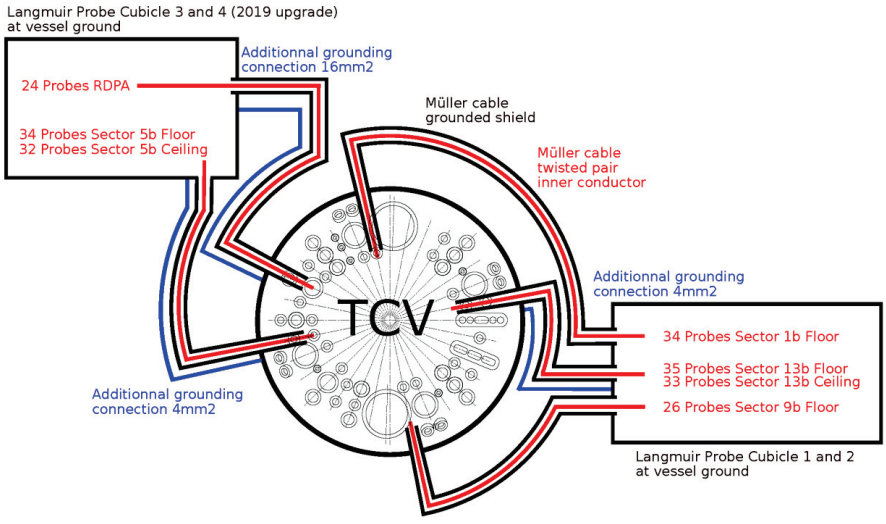

Figure 2.7: Electrical connections in between the tokamak and the electronics cubicles for the divertor upgrade with biased conductors in red and grounded conductors in black. The RDPA diagnostic has been included in the image because it relies on the same electronics as the LPs.

Langmuir probe electronics are necessarily referenced to the vacuum vessel ground, as opposed to most diagnostics at TCV which are referenced to the TCV building ground. The electronics cubicles are therefore separated from the building ground using an isolation transformer.

The 19 pairs Mueller® cable shield connects the electronics cubicles to the vacuum vessel ground, as sketched in FIG. 2.7. The cables do not encircle the vacuum vessel to avoid receiving the loop voltage induced by the central solenoid.

During a discharge, the time derivative of the vertical magnetic field can be as high as $\approx 0.05\ T/s$ in the region between the vacuum vessel and the cubicles ($r \approx 2\ m$, $z \approx -1.5\ m$) mainly due to the contribution of poloidal field coils. The inductive current going through the shield can be estimated from the resistance $R_{shield} \approx 0.1\ \Omega$. The stray current can be approximated with the laws of Ohm and Faraday:

$$I = \frac{U}{R_{shield}} = \frac{S\frac{dB}{dt}}{R_{shield}} \approx \frac{10\ m^2 \cdot 0.05\ T/s}{0.1\ \Omega} \approx 5\ A \tag{2.12}$$

This relatively modest stray current is not expected to perturb the measurements or the TCV magnetic field.

2.4 Design of the amplifier circuitry

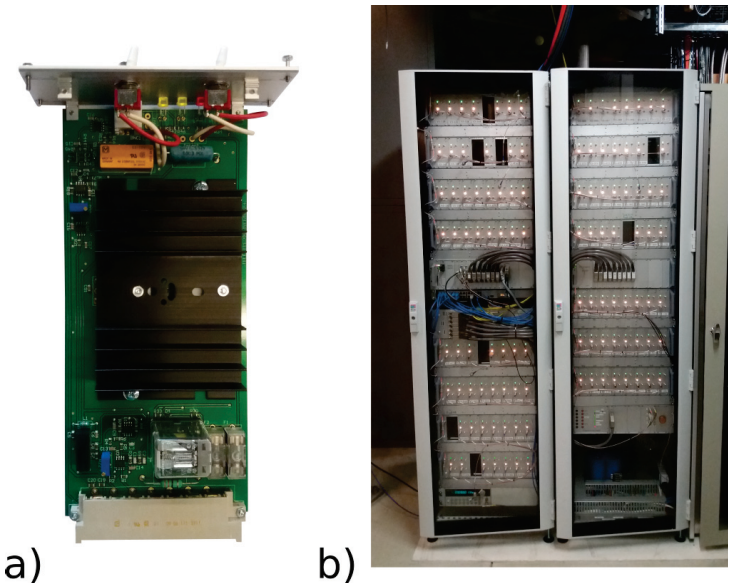

Figure 2.8: Single amplifier **a)** and complete cubicle **b)**. A few amplifiers have been removed where the in-vessel transmission line has been damaged.

There have been three different generations of Langmuir probe amplifiers developed at SPC. Only the third generation is described in detail here. The first generation did not have any

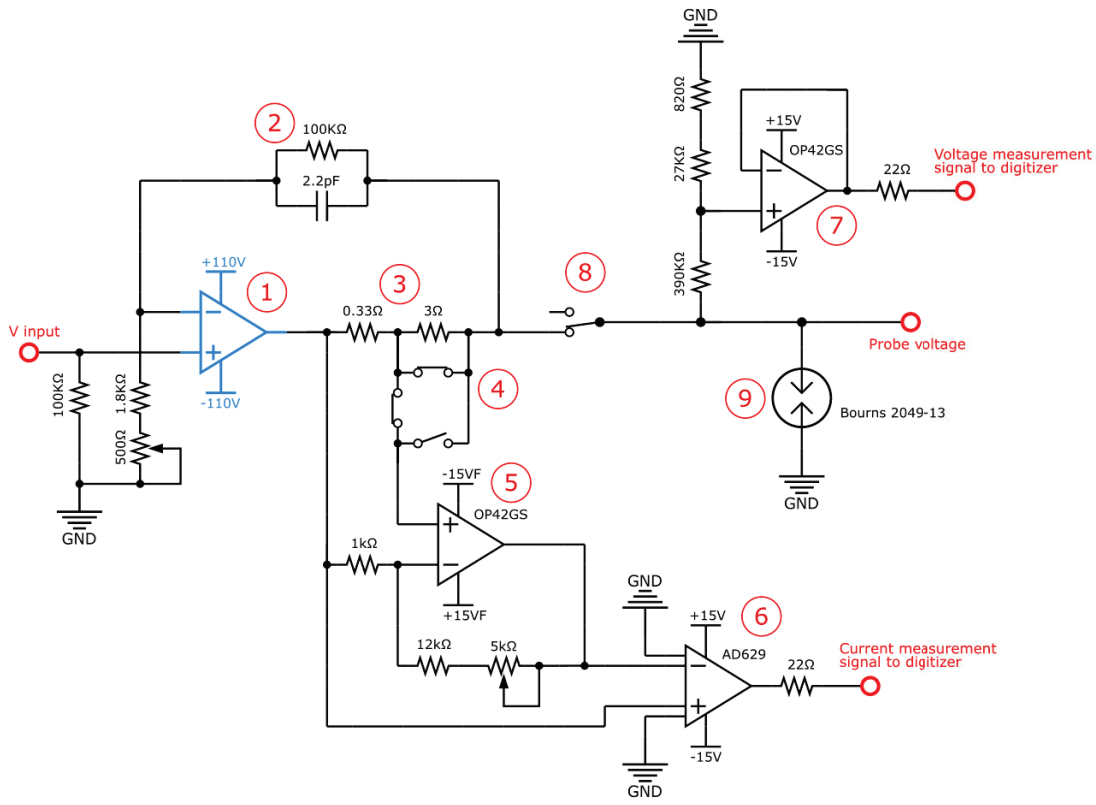

Figure 2.9: Custom Langmuir probe electronics [68]: ① Custom amplifier in blue (see FIG. 2.11), ② Overall negative feedback loop, ③ Shunt resistors, ④ Shunt relays (here the 3 Ω resistor is bypassed to select the large current measurements $\pm 2A$), ⑤ OP-Amp used to amplify the current measurement signal (the potential drop across the shunt resistors), ⑥ High common mode unity gain OP-Amp referencing to ground the current measurement signal, ⑦ OP-Amp used as a voltage divider for the potential measurement, ⑧ Switch to select either the biased probe potential mode V_{pr} or the floating potential mode V_{fl} and ⑨ Surge protection.

custom amplification module and was based on $PB58A$ APEX® amplifiers. In the second generation, the APEX® amplifier was replaced by a patch developed at SPC. The patch will not be described here because it can be considered as obsolete when compared to the latest generation. Indeed, the third generation features an improved current measurement and an improved current limitation system over the second generation.

This section is organized in five subsections. SEC. 2.4.1 presents the general constraints given from plasma parameters while SEC. 2.4.2, SEC. 2.4.3, SEC. 2.4.4 and SEC. 2.4.5 cover, respectively, the choice of power supplies, the amplification system, the potential and current measurement system and the current limitation system.

A single amplifier module is shown in FIG 2.8, as well as the cubicle installed in the TCV basement level. The organization of the electronics of a single amplifier within the complete

diagnostic environment is illustrated schematically in FIG 2.10 and a complete drawing of the circuitry is given in FIG 2.9.

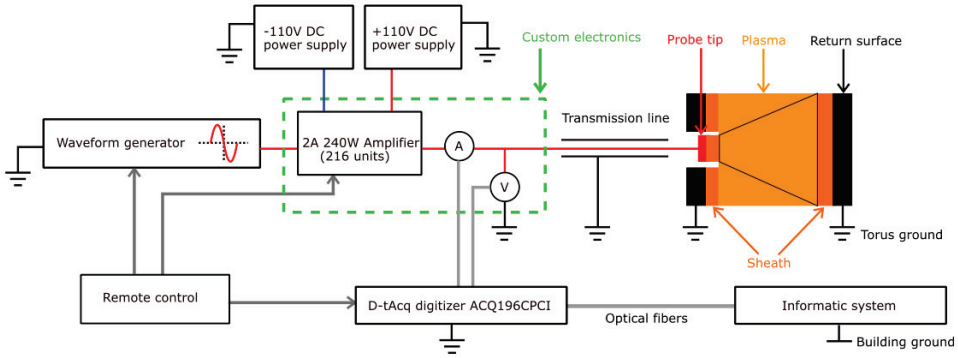

Figure 2.10: Diagram including the main components of the electronic system and the equivalent circuit for the Langmuir probe with the current flowing between the probe tip and a larger return surface.

Amplifiers, waveforms, acquisitions and power supplies are all referenced to the torus ground. Electrical insulation from the building ground is provided with optical fibers once the signal has been digitized, see FIG 2.10.

2.4.1 Requirements

In order to measure the current-voltage characteristics described in EQ. (2.9), V_{pr} must be swept from a strongly negative voltage $V_- \approx V_{fl} - 3T_e$ to obtain sufficient saturation for the ion flow, up to the plasma potential $V_p \approx V_{fl} + 3T_e$ [38]. The floating potential is usually found in between $V_{fl} = -30\ V$ and $V_{fl} = +15\ V$ in TCV plasmas. Target electron temperatures typically do not exceed $T_e \approx 30\ eV$. Therefore the biased probe voltage should range at least from $V_{min} \approx -30\ V - 3 \cdot 30\ V = -120\ V$ up to $V_{max} = 15\ V + 3 \cdot 30\ V = 105\ V$. Two separated DC power supplies have been selected to provide the sufficient extrema voltages $V_{pr} = \pm 110\ V$. It should be noted, however, that for some discharges, the floating potential is extremely low and T_e above 30 eV, e.g $V_{fl} = -45\ V$ and $T_e = 45\ eV$ for shot #58182 (low density, high plasma current, high confinement mode discharge). In this particular case, the amplifiers are unable to apply a voltage low enough to fully approach ion saturation.

Target electron densities at the sheath edge typically do not exceed $n_{e,se} \approx 1.5 \cdot 10^{19}\ m^{-3}$. It is possible to obtain an estimate of the corresponding ion saturation current:

$$I_{sat} = n_{e,se} e S \sqrt{\frac{e(T_e + \gamma T_i)}{m_i}} \approx 0.36\ A, \tag{2.13}$$

with $n_{e,se} = 1.5 \cdot 10^{19}\ m^{-3}$, $S = 2.8\ mm^2$ the projected area of the domed probes used in TCV with incident field lines at grazing angle $\alpha = 0°$, $T_e = T_i = 30\ eV$, $m_i = 3.32 \cdot 10^{-27}\ kg$ in a

deuterium plasma and $\gamma = 1$. Therefore, the $-110\ V$ power supply has been chosen to deliver $9\ A$ DC, sufficient to provide the maximum current calculated in equation 2.13 to at least $9/0.36 \approx 25$ probes.

The electron saturation current with the same plasma parameters can be estimated as follows [38] [51]:

$$I_{sat,e} = -|I_{sat}| \cdot \sqrt{\frac{2m_i}{\pi m_e}\left(\frac{T_e}{T_e + \gamma T_i}\right)} \approx -12.3\ A. \tag{2.14}$$

The theoretical ratio $|I_{sat,e}/I_{sat}| \approx 34$ is usually much higher than the experimental ratio of $I_{sat,e}/I_{sat} \approx 6$ [78], mainly because the electron depleted region in magnetized plasmas becomes longer than the mean free path of electron ion collisions [78] and the collisionless assumption required in sheath theory is no longer valid. Nevertheless, the estimated maximum electron saturation current $I_{sat,e} \approx 6 I_{sat} \approx 2.16\ A$ is found beyond the acquisition range limit of $\pm 2\ A$ in experiments with high target temperature and density.

The positive $+110\ V$ DC power supply has been sized to deliver $18\ A$, enough to attain the $2\ A$ acquisition limit in electron saturation simultaneously on 9 different probe tips.

2.4.2 Power supplies

The positive $+110\ V$ power supply consists of 2 Camtech® $HPV10001\ 9.1A$ units and the negative $-110\ V$ power supply consists of a single one. These units include galvanic insulation and can therefore be directly connected between the standard $220V$ AC network and the torus ground. Both positive and negative terminals are connected to large capacitances $C_{out} = 2800\ \mu F$. These large capacitances add up to the Camtech® power supplies internal capacitances in order to provide a current transiently exceeding $19A$ in the case of electron saturation with swept bias voltage.

The positive $+15V$ power supply consists of a $26A$ Camtech® $HSE04801$ and the negative $-15V$ supply consists of a $5A$ Camtech® $HSW00751$. The current requirement is larger for the positive voltage since it supplies current for the $\pm 15VF$ DC-DC power supply, item ④ in FIG. 2.11. The highest current drawn per amplifier is $\approx 55\ mA$ for the DC-DC power supply, as explained in SEC. 2.4.5. Therefore the $26A$ unit is sufficient to power hundreds of amplifiers at the same time.

A delay switch ensures that the $\pm 15V$ power supply is always activated once the ± 110 power supply turns on.

2.4.3 Amplification

The probe voltage is remotely controlled by changing the waveform generator settings. The waveform generator voltage is amplified 50 times with the overall negative feedback loop on the custom amplifier circuitry, see item ② in FIG. 2.9 and item ② in FIG. 2.11. The gain is

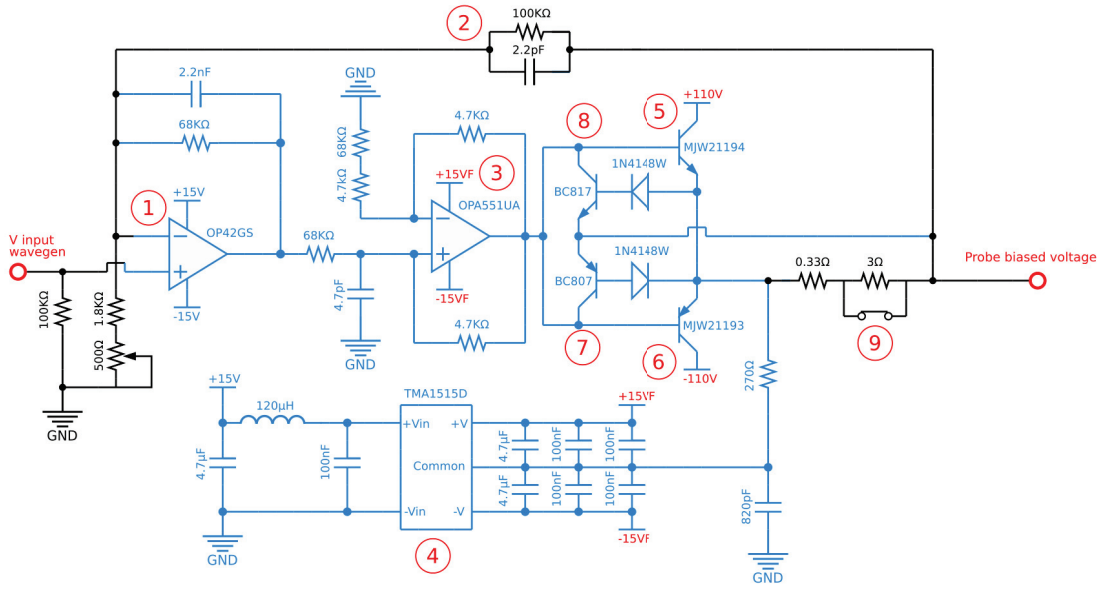

Figure 2.11: Detailed circuit of the custom amplifier (item ① in FIG. 2.9): ① First OP-Amp ② Overall negative feedback loop from probe voltage, ③ Second OP-Amp used to step up the voltage ④ DC-DC power supply for the second OP-Amp with the "common" reference being close to the probe potential, ⑤ Silicon power transistor delivering the negative current, ⑥ Silicon power transistor delivering the positive current, ⑦ Transistor used to limit the negative current, ⑧ Transistor used to limit the positive current and ⑨ Shunt relays (here the 3Ω resistor is bypassed to select the large current measurements $\pm 2A$).

precisely tuned on each amplifier by changing the resistance of the 500 Ω potentiometer.

A 2.2 nF capacitance has been set on the negative feedback loop of the first OP-Amp, see item ① in FIG. 2.11. This capacitance primarily determines the measured cutoff frequency of the overall amplifier $f_{cutoff} \approx 25\ kHz$ for stability purposes. The cutoff frequency is much higher than the typical sweeping frequency necessary for time-averaged measurements $f_{sweep} \approx 300\ Hz$. However, it does not allow the ultra fast sweeping required to resolve fluctuations from plasma micro-turbulence [52].

The second OP-Amp, see item ③ in FIG. 2.11, is a so-called *suspended OP-Amp*: the potential reference VF of the positive and negative power supplies $VF \pm 15\ V$ is very close to the probe voltage, therefore suppressing the need for any large potential differences at the OP-Amp terminals.

2.4.4 Potential and current measurement system

The voltage measurement consists in dividing the probe voltage by a factor of 15 before the analog-to-digital conversion with a resistive divider. The OP-Amp *OP42GS*, item ⑦ in FIG. 2.9 is connected as a voltage follower and the resistances are selected in order to obtain $\pm 10\ V$

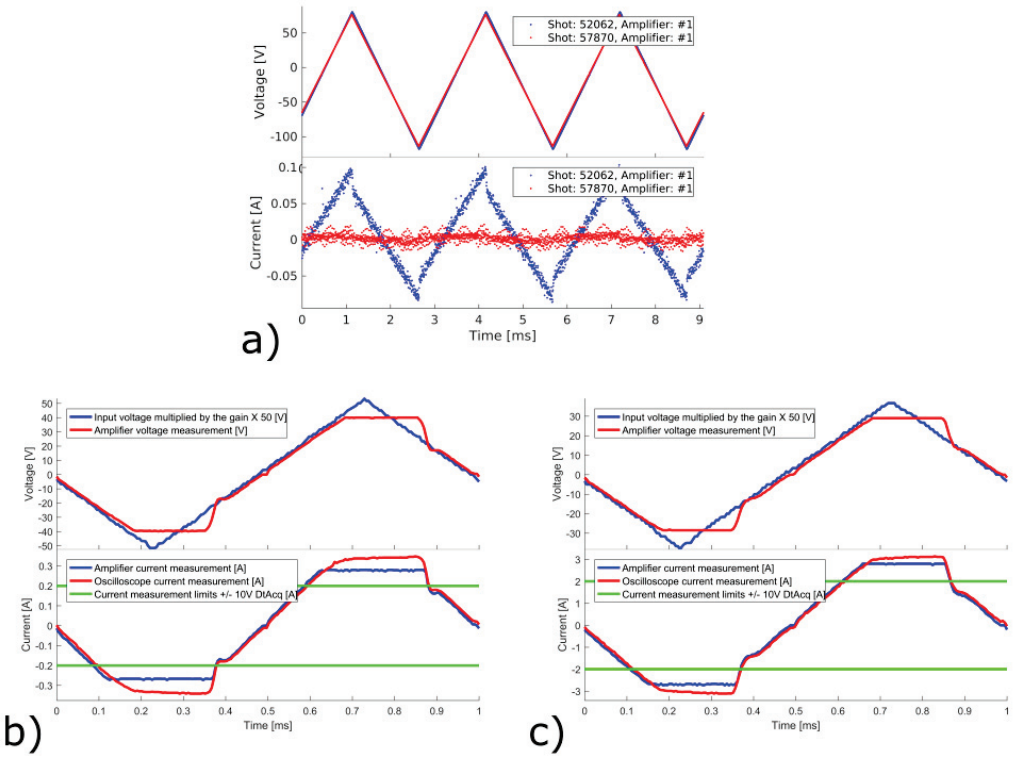

Figure 2.12: **a)** Virtual current measurement recorded after the end of the plasma discharge (no load) for a triangular voltage sweep from the first generation of amplifier in shot #52062 and from the third generation amplifier in shot #57870, **b)** current limitation test with a 1 kHz triangular voltage sweep, 100 Ω load and the shunt selection for small current measurements ±0.2 A and **c)** same measurement with a 10 Ω load and the shunt selection for large current measurements ±2 A.

at the digitizer when the probe voltage is ±150 V. The acquisition is provided by D-TACQ Solutions Ltd® ACQ196CPCI 16 bits digitizers sampling at 200kS/s. The voltage measurement range is sufficient to cover the power supply range ±110 V. Probe voltages beyond ±150 V are obtained only in the non-stationary case of plasma disruptions with the probes in V_{fl} mode.

The current measurement system is more complex than the voltage measurement one. In the first generation of amplifiers, the voltage drop across the shunt resistors was directly sent to the differential inputs of a high common mode unity gain OP-Amp. The voltage drop range is ±0.66 V and it was then amplified to match the digitizer input voltage range ±10 V. Virtual currents originating from the imperfect common mode rejection were acquired, as shown in FIG. 2.12 **a)**. These residual currents have to be subtracted from the data by averaging the traces before or after the plasma discharge. OP-Amps $AD629$ have also been used in other Langmuir probe systems in a similar fashion in order to address the issue of common mode rejection [79].

In the third generation of amplifiers, the potential drop through the shunt resistors is first amplified with an OP-Amp, see item ⑤ in FIG. 2.9. The signal is then referenced to ground potential through the high common mode unity gain OP-Amp $AD629$ in order to be acquired, see item ⑥ in FIG. 2.9. Virtual currents have been highly reduced thanks to the higher signal to common-mode ratio, as seen in FIG. 2.12 **a)**. The subtraction of virtual currents is still maintained in the routines for the Langmuir probe analysis [51] because capacitive currents are still present with the new electronics.

The current measurement is calibrated in order to obtain $\pm 10\ V$ at the digitizer when the current is $\pm 0.2\ A$ in low current mode and $\pm 2\ A$ in high current mode. Dense and hot plasma at the probe can regularly attain the $2\ A$ acquisition limit in electron saturation. The saturation of the acquisition does not represent any significant information loss since data points in the electron saturation region are not taken into account by the minimum temperature method chosen for the 4 parameters fit of the IV curve [51] given in equation 2.9.

In the case of negative bias and when the shunt selection for large current $\pm 2\ A$ is chosen, the current limitation is always above the probe current, which is typically $I_{sat} < 0.36\ A$, see equation (2.13).

The measured resonance frequency point of the current measurement system is $f_{res} \approx 250\ kHz$. Therefore any current fluctuation faster than the upper cut-off frequency $f_{cm} \approx f_{res}$ can not be seen in the acquired data.

2.4.5 Current limitation system

Current limitation is necessary to avoid over-currents in the silicon power transistors, to limit heat-flux onto the probe tips (in the electron saturation region) and to avoid the current starvation of the high voltage power supplies $\pm 110\ V$ which can happen when many probes draw high currents at the same time.

The current limits are determined by the sum of the diode threshold voltages from the transistors $BC817$ and $BC807$, see items ⑦ and ⑧ in FIG. 2.11, and from the 2 diodes $1N4148W$. Once the voltage drop across the shunt resistors overcomes the sum of the diode threshold voltages $V_{threshold} \approx 0.6\ V + 0.6\ V \approx 3.33\ \Omega \cdot 0.35\ A$ or $0.33\ \Omega \cdot 3.5\ A$, the OP-Amp $OPA551UA$ delivers current directly to the Langmuir probe and the silicon power transistor is bypassed. The large current requested by the overall feedback loop can rapidly damage the OP-Amp $OPA551UA$. This is why a $270\ \Omega$ resistor has been installed to starve the floating power supply of the OP-Amp $OPA551UA$ once the return current becomes larger than $I_{max} \approx \frac{15\ V}{270\ \Omega} \approx 55\ mA$. Therefore, even though the voltage required by the overall feedback, item ② in FIG. 2.11, is still very high, the effective voltage at the OP-Amp $OPA551UA$ output and the probe voltage are lower, just enough to supply the current limit $\pm 0.35\ A / \pm 3.5\ A$.

Tests of the current limitation system are presented in FIG. 2.12 **b)** for the $\pm 0.2\ A$ shunt mode and in FIG. 2.12 **c)** for the $2\ A$ shunt mode. A specific setup with a voltage isolator device

connected to an oscilloscope referenced to ground is required to measure the actual current limit. Indeed, the maximum current measurable by the amplifier circuitry is lower than its actual current limitation $\approx \pm 0.35\ A / \pm 3.5\ A$, due to the finite voltage $VF \pm 15\ V$ supplying the OP-amp $AD629$, item ⑥ in FIG. 2.9. The test frequency $f = 1000\ Hz$ is chosen to be similar to the typical sweeping frequency used at TCV. The test peak voltages and the test resistors 10 Ω and 100 Ω have been chosen in order to attain the current limit.

The probe current is limited to $I_{pr} \approx \pm 0.35\ A$ as shown in FIG. 2.12 **b)** when both shunt resistors are connected. It is limited to $I_{pr} \approx \pm 3.5\ A$ when the 3 Ω shunt resistor is bypassed as shown in FIG. 2.12 **c)**. The $\pm 0.27\ A$ and $\pm 2.7\ A$ plateaus observed with an oscilloscope for the amplifier current measurement, plotted in blue in the bottom panels of FIG. 2.12 **b)** and FIG. 2.12 **c)**, correspond to the saturation of the high common mode OP-Amp due to the finite voltage supply $\pm 15\ V$. The measurement would have been limited to $\pm 10\ V$ if the measurement had been done with the digitizers instead of an oscilloscope, as explained in SEC. 2.4.4.

2.5 Protection against amplifier damage

The silicon power transistors, items ⑤ and ⑥ in FIG. 2.11, are the most frequent components responsible for amplification failure. Usually both components are damaged at the same time. This may lead to a short circuit between the power supply terminals $\pm 110 V$ which is rapidly stopped by $2A$ fuses installed in series with the power supply terminals of each amplifier. The transistors for the current limitation, items ⑦ and ⑧ in FIG. 2.11, are also damaged in ≈ 20% of the cases. The typical rate of failure is one amplifier per week of probe operation at TCV with the loss of 29 amplifiers between July 2017 and April 2018 (with 48 amplifiers installed at that time).

These failures can be caused by current surges faster than the time response of the current limitation system described in SEC. 2.4.5. It can be also caused by absorption of energy when the plasma itself transiently acts as a power supply instead of a load. The power transistors are indeed vulnerable to non-standard operation such as base-emitter junction breakdown in this case.

These processes mostly occur during transient plasma events such as: tokamak plasma current disruptions, Edge Localized Mode (ELM) transients and electron cyclotron microwave power not absorbed by the plasma. The corresponding timescales of these processes are $\approx 0.5\ ms$ and $\approx 1\ ms$ (typical durations of the plasma thermal quench and the plasma current quench), $\approx 0.5\ ms$ (ELMs) and $\approx 1\ s$ (microwave power).

2.5.1 Attempt to prevent amplifier damage with fuses

Cartridge fuses FSF5X20250V2A (reference 0034.1519) were used in series with the transmission line on the first generation of amplifiers. Due to the inefficiency of these fuses, it was

decided to eliminate them in the latest generation.

The lack of fuse effectiveness is believed to be linked to the fuse breaking time. Even if the current is large enough to provide the integrated energy $RI^2\Delta t$ necessary to melt the conductor, at least a few milliseconds are required for any fuse to completely stop the current [80] due to the formation of an electrical arc. Therefore, the fuse would not protect the transistors during the first $\Delta t = 1\ ms$ of any off-normal events, regardless of the current value.

2.5.2 Attempt to prevent amplifier damage with surge protectors

The main purpose of using surge protectors is to prevent the probe potential from exceeding the power supply range $\pm 110\ V$.

Surge protectors, as well as varistors [81] fulfill protection requirements because of their fast time response (ranging from $\approx 50\ ns$ to $10\ \mu s$ depending on the product). Surge protectors Bourns® 2049 – 13 with the specified DC spark-over $130\ V$ were connected directly in between the transmission line conductor and ground, see item ⑨ in FIG. 2.9. Once the voltage difference between the grounded electrode and the electrode at probe voltage is higher than the surge protector breakdown voltage, a Paschen discharge is initiated in the low pressure gas chamber to short-circuit the transmission line. The surge protector breakdown was tested in the laboratory, as described in the next two paragraphs and surge protectors were then installed in the machine to evaluate the protection effectiveness.

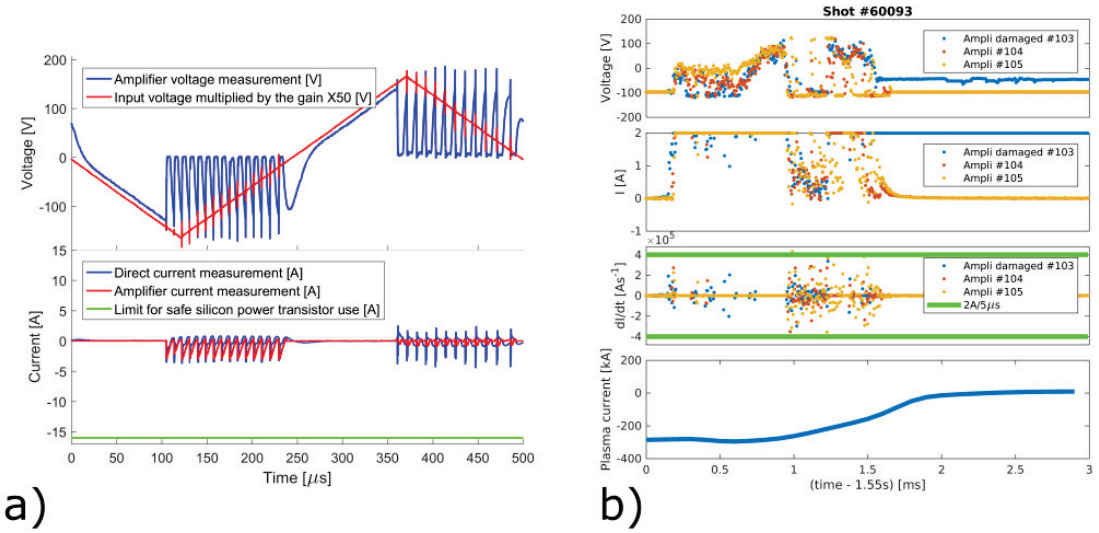

Figure 2.13: **a)** Time traces of the surge protection being switched on with a triangular waveform at 2 kHz. Each sawtooth oscillation consists of three different phases: the discharge time, a glow period and the voltage ramp-up time of the amplifier and **b)** time traces during a disruption where the amplifier connected to the probe #103 is damaged. For comparison, time traces of neighbouring amplifiers are also shown.

Testing surge protectors before installation at TCV

A test has been done without any resistive load at the amplifier output in order to see the bare surge protector current. Once the surge protector is triggered, current and voltage show a characteristic sawtooth behavior oscillating at $\approx 100\ kHz$ as shown in FIG. 2.13 **a)**. The maximum current rating $I_{collector} = 16\ A$ according to the manufacturer for the silicon power transistors has been plotted on the same figure. All of the current signals shown in FIG. 2.13 **a)** correspond to the current flowing through the surge protector. The $\approx 10\ \mu s$ period of this sawtooth oscillation is the sum of the measured breakdown time $t_{breakdown} \approx 1\ \mu s$, a glow period $t_{glow} \approx 4\ \mu s$ and the voltage ramp up time constant $t_{ramp} \approx 5\ \mu s$. Once triggered, surge protectors switch off again once the voltage applied is reversed. Therefore, it assures reliable data acquisition 0.75 ms after any event that could have triggered the surge protector (1/4 of the typical triangular waveform sweeping period applied).

Installation of surge protectors at TCV and unsuccessful protection

The installation of surge protectors on 30 amplifiers out of 114 did not decrease the failure rate. From March 2018 to July 2018, 3 out of the 13 damaged amplifiers were equipped with surge protectors. The surge protectors on the damaged amplifiers did not show any sign of fatigue. For one of these damaged amplifiers, the time traces of the event were recorded in the experiment #60093, as shown in FIG. 2.13 **b)**. On this figure, it can be seen that after the disruption, the amplifier #103 is no longer able to provide the $-100\ V$ voltage required for I_{sat} measurement, proving that the silicon power transistor lost its semiconductor properties. It is interesting to notice that the time derivatives of the current are very high, sometimes exceeding $2\ A/5\ \mu s$ (the positive acquisition limit divided by the acquisition period).

The lesson learned is that amplifier failure can happen within the voltage range from the power supplies $\pm 110\ V$ and therefore surge protectors do not offer an adequate protection.

2.5.3 Preventing amplifier damage by increasing the transmission line inductance

In order to limit the peak current flowing before the current limitation system has time to trigger, a simple solution is to increase the inductance of the transmission line. Any sudden current change would change the probe voltage in order to oppose the increase in current following the equation $U_L = -L dI/dt$. The second positive effect would be to stabilize the emitter and collector voltages of the transistor in order to avoid the emitter voltage to transiently surpass the base voltage.

This possible solution has not been implemented in TCV because of the possible perturbation to the measurement. Detailed calculations are given in [68].

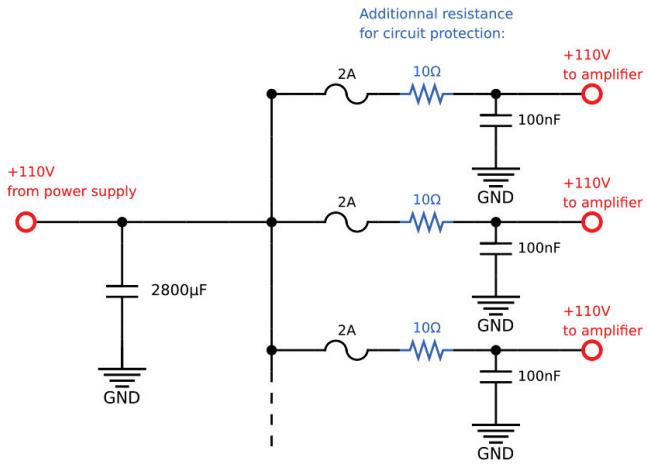

Figure 2.14: Equivalent circuit for the positive $+110V$ power supply. All of the 120 amplifiers in the cubicles 1 and 2 are connected to the same large capacitor. The same circuit applies for the negative $-110V$ power supply. The additional protective resistances R_{extra} are highlighted in blue.

2.5.4 Preventing amplifier damage by decreasing the effective power supply capacitance

The large capacitor mounted in parallel with the high voltage supply of each amplifier is a disadvantage during plasma transient events because it can provide large amounts of energy to the individual probe tips having the smallest sheath resistances. The issue can be partially solved by adding a resistor in series with the amplifier, see FIG. 2.14, in order to drop the line voltage in case of high current excursions.

For instance, in the presence of a $20A$ surge during a disruption when the bias voltage is $+100\ V$, the effective sheath resistance is $R_{sheath} = 100V/20A = 5\ \Omega$. In this case an additional resistance $R_{extra} = 10\ \Omega$ would lower the current down to $I = U/R = 100V/(5\Omega + 10\Omega) \approx 6.7A$. This reduction in current would likely be sufficient to prevent transistor damage.

During normal operation, the current can attain $2A$ in electron saturation. In this case the voltage of the power supply would be lowered down to $V = 110V - R_{extra}I = 110V - 2A \cdot 10\Omega = 90V$. The voltage drop would be acceptable from a physics point of view because most of the voltage range in the IV curve would remain accessible.

Circuit safety is always maintained when the voltage command is higher than the power supply voltage at the amplifier. Indeed, the floating power supply voltage $\pm 15VF$ of the second amplification OP-Amp, item ③ in FIG. 2.11, will drop through the 270Ω resistor and therefore limits its current.

The resistance protection solution is thought to be more effective than the inductance protection solution because it can address the problem of current surges regardless of the temporal

characteristics. The combination of surge protectors and 10 Ω resistors on all the 216 Langmuir probes amplifiers of TCV has led to a substantial decrease in the frequency of amplifier damage. The full protection was already installed in the months of August and September 2019, and the failure rate remained low throughout 2020, with 35 amplifier failures over the whole year of operation.

It is important to emphasize that the additional resistance must be used in conjunction with the surge protectors. Indeed, the probe voltage is allowed to make large excursions during off-normal events because of the additional resistance and therefore a voltage limit must be installed to protect the current measurement system.

The $\pm 15\ A$ power supply used for the current measurement system is not fused and some current measurement chips have been burned when electrical faults developed due to the absence of surge protectors. The fire partially extended to the rest of the board but did not reach other amplifiers. Installing fuses on the $\pm 15\ A$ power supply would increase safety in this regard, although the probability of such an incident is currently much lower thanks to the installation of the surge protectors.

2.6 Possible future improvement to the current measurement system

The current measurement system suffers from two issues: **1)** the time response is quite slow, $\approx 250\ kHz$, as discussed earlier in SEC. 2.4.4, primarily because of the slow time response of the $AD629$ OP-Amp and **2)** the component $AD629$ can sometimes fail because it is directly exposed to the voltage difference between the probe and the tokamak ground. While the presence of surge protectors should avoid any large voltage excursions, these components are prone to ageing and do not assure an absolute protection on the long term.

A possible solution for a future upgrade of the current measurement system on the long term is proposed in the FIG. 2.15. Instead of the low shunt resistance value used in the current design (0.33 Ω/3.33 Ω), a larger shunt resistance value would be used, e.g. 10 Ω, in order to enable the division of the measured voltage $\pm 150\ V$ down to the OP-Amp $\pm 15\ V$ working voltage range. Furthermore, the large resistance would give an additional protection to the amplifier against large current excursions.

Let us make the calculations for a typical example in ion saturation: the probe voltage is maintained at $-100\ V$ by the amplifier and the current passing through the probe is $2\ A$. A shunt resistor of 10 Ω would lead to a voltage drop of $20\ V$: $-100\ V$ on the probe voltage and $-120\ V$ at the amplifier output behind the shunt. The resistive voltage divider in both voltage measurements by a factor of 15 gives us $-6.66\ V$ on the probe voltage and $-8\ V$ at the amplifier output behind the shunt. The voltage drop is only $1.3333\ V$ and therefore needs to be amplified by a factor $15/2 = 7.5$ with a dedicated OP-Amp in order to match the acquisition range $\pm 10\ V$, see FIG. 2.15.

To conclude, this proposed measurement circuit is believed to have a faster time response and to be more resilient to voltage transients. The possibility to switch to a higher shunt value to measure low current could be implemented as for the existing circuit.

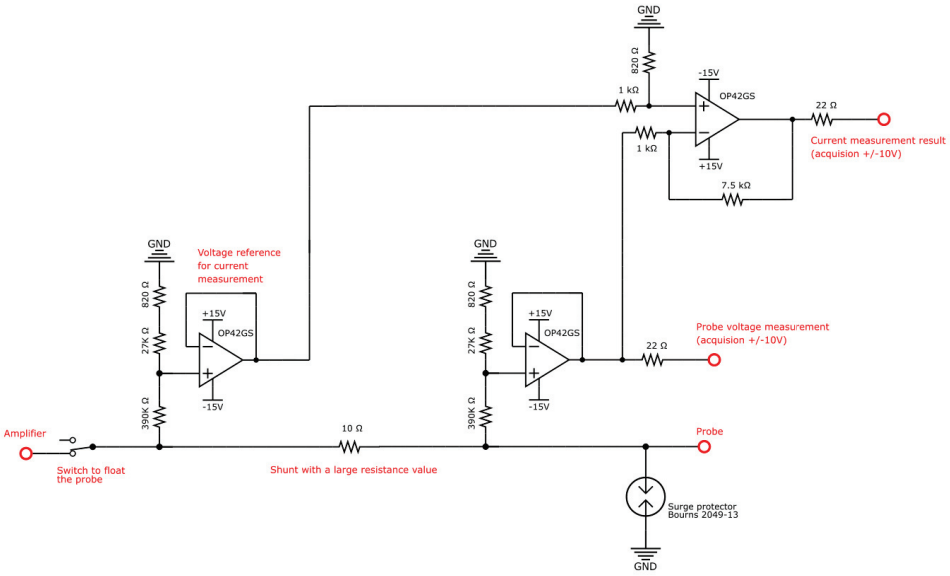

Figure 2.15: A possible solution for a future upgrade of the current measurement.

2.7 Analysis routines

Once the data is acquired, the analysis routine can be launched. The routines have been written in the Matlab® environment. The fitting functions have been written in Fortran in order to speed up computational time [51].

The different steps performed by the analysis for the voltage sweeping mode have been listed here: **1)** Virtual currents from the circuit imperfections are corrected based on the signal recorded before and/or after the plasma discharge. **2)** Current values are scaled accordingly to the shunt selection 0.33/Ω/3.33Ω. **3)** Current densities are calculated from the current values and from the effective probe collection areas that depends on the probe geometries and on the pitch angle of the magnetic field at the probe location. The pitch angle of the magnetic field is obtained from the magnetic equilibrium reconstruction system LIUQE [82]. **4)** A single voltage sweep is usually statistically not sufficient to obtain a reliable fit because turbulent events can sometimes distort the IV curve during the most critical part of the fit, i.e. during the exponential decay of the electron current. Therefore, the data points are split in overlapping bins of time duration $2 * period$ where $period$ is an arbitrary time duration chosen by the user. The overlap is $1 * period$. A period of 10 to 25 ms has been usually found to produce results of higher quality. An example of a time window for the shot 64766 is shown in FIG. 2.16 **a)** where the data from ≈ 20 fits has been merged into a single IV plot. **5)** The data points are

then binned as a function of voltage in order to create a smooth IV curve, see the red curve in FIG. 2.16 **b)**. The voltage bins are arbitrarily chosen to be $\approx 2\ V$ wide and therefore, there are approximatively $200V/2 = 100$ points defining the IV curve. **6)** A hyperbolic tangent fit is applied to the data set in order to obtain first estimates for the ion saturation current and electron temperature. These estimates are used as initial guesses for the subsequent fits. **7)** A series of four parameters fits are applied to the data points, see equation (2.9). A vector named $vm4par$ must be given by the user in order to determine how far the data should be fitted into the positive probe voltage range. $vm4par$ is defined in units of ion saturation currents, e.g. if $vm4par = [1,3]$, the fit is applied to the points of the IV curve above $-1 * I_{sat}$ and then to the points of the IV curve above $-3 * I_{sat}$. In a magnetized plasma, the IV curve deviates from an exponential variation well below the plasma potential. If the values from the IV curve at the floating potential and/or beyond are fitted, EQ. (2.9) may results in an overestimation of the electron temperature [78]. **8)** In order to determine the best fit from all the results obtained in **7)**, the result with the lowest electron temperature is chosen [51]. **9) (optional)** An asymmetric Langmuir probe fit can be optionality chosen [51]. This fit is mostly relevant in relatively low electron temperature conditions, as the electron saturation current must be recorded within the acquisition limits $\pm 2\ A$. It should be noted for the user that the asymmetric Langmuir probe fit requires a longer computational time than the four parameters fit. **10)** The average and standard deviation of the raw data for the lowest probe voltages (ion saturation current) is performed at the sweep frequency. The values obtained have a finer temporal resolution than the four parameters fit results and can be used as a sanity check for the fits. The ion saturation current obtained with this method is usually ≈ 15 % larger than the four parameters result in the case of domed probes because sheath expansion is not taken into account. **11) (optional)** The results are then optionality saved on the MDS tree and can be accessed by all users. Since the computational time required for a single TCV experiment is usually less than 10 minutes, overwriting another user's results is not a critical issue. **12) (optional)** The results of the fits can be accessed by calling a specific routine: *LP_TCV_4(shot_number,'show_fit')*. A window similar to FIG. 2.16 is then displayed. The user can then select the desired probe position, see FIG. 2.16 **c)**, and the desired time in order to display the corresponding fit.

2.8 Inter-ELM analysis routines for H-mode studies

ELM events are not long enough to allow resolving the IV curve with conventional Langmuir probe electronics. The ion saturation current measurement is also impossible to obtain during an ELM in TCV, because the limited voltage from the amplifier is not sufficiently negative to repel the entire electron population. Therefore, LP analysis is mostly performed during the inter-ELM time windows in H-modes. ELM heat fluxes are obtained more easily with other diagnostic types, such as IR.

ELM times are detected based on the strong $D-\alpha$ (Balmer line for the $3 \rightarrow 2$ transition) light burst emitted once the hot plasma from the ELM comes in contact with the neutral particles in the main chamber and in the divertor. $D-\alpha$ light is recorded with photodiodes equipped

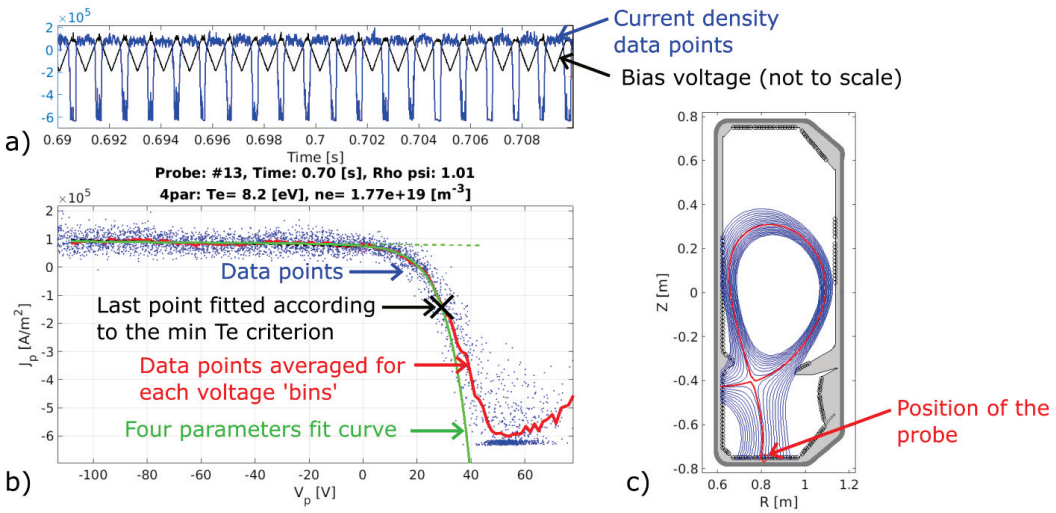

Figure 2.16: Shot 64766, REVB, $I_p \approx 320\ kA$. **a)** Time window with the considered data point for the fit, **b)** IV curves of the raw data, smoothed IV curve and four parameter fit obtained with the lowest electron temperature and **c)** position of the probe tip considered in the TCV poloidal plane.

with a specific filter. The photodiodes have a high temporal resolution and collect photons from a large solid angle covering almost an entire sector at a specific toroidal location. ELMs consist of toroidally elongated filamentary structures moving from the plasma edge to the SOL and therefore the toroidal location of the camera is not important.

The ELM-detection routine requires two different inputs from the user in order to properly function: **1)** A threshold value for the $D-\alpha$ light, any value above this threshold is potentially considered as an ELM. **2)** A threshold value for the time derivative of the $D-\alpha$ light, any value above this threshold can be considered as the onset of an ELM. Both conditions must be met to consider that the $D-\alpha$ light burst corresponds to an ELM. Once the routine is launched by the user, a prompt appears, asking for a visual confirmation of the ELM-detection process, see the top plot from FIG. 2.17.

Two other parameters specified by the user are also needed to determine how much of the data during the ELM time window should be discarded: **1)** The beginning of the inter-ELM time window, which must be set between 0 and 1, represents the starting point of the relevant inter ELM period. Data points before the beginning of the window are excluded from the fit. The typical value used is 0.3 in order to avoid recording data from the previous ELM. **2)** The end of the inter-ELM time window, which must be set between 0 and 1, represents the ending point of the relevant inter ELM period. Data points after the end of the window are excluded from the fit. The typical value used is 0.8 in order to avoid recording data from the incoming ELM.

The discarded data is highlighted in red in the bottom plot shown in the FIG. 2.17. The probe

voltage is shown on top of the $D-\alpha$ signal. Although the sweeping frequency shown in FIG. 2.17 is equal to 330 Hz, a sweeping frequency of ≈ 900 Hz is better suited to resolve inter ELM periods, whose frequency are in the $100-400$ Hz range in TCV [83].

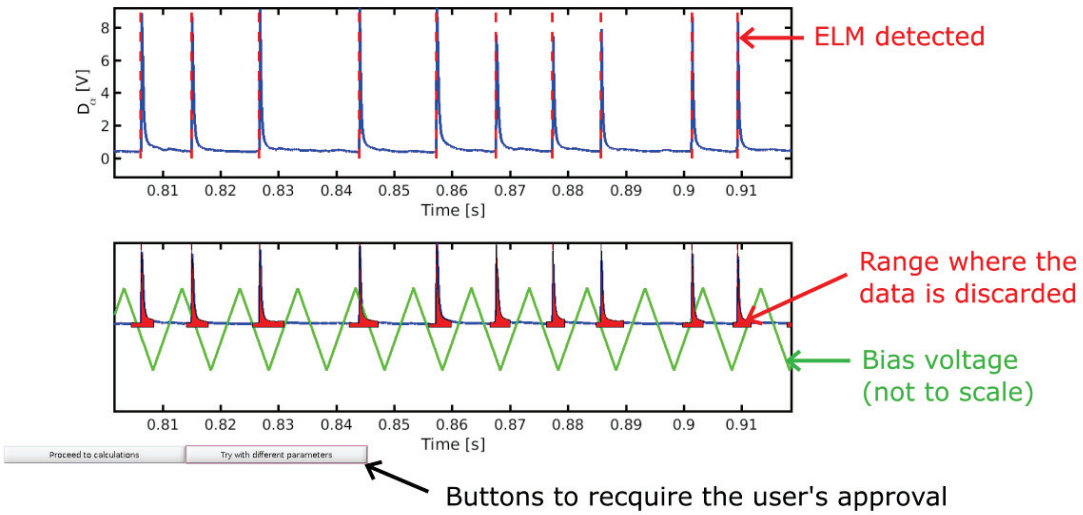

Figure 2.17: Prompt requiring user's approval for the validation of the ELM-removal routines.

The electron temperature, ion saturation current and sheath heat flux profiles from the floor probes are shown as an example result in FIG. 2.18. These results corresponds to the inter-ELM period from an ELM-ing H-mode forward field plasma with $I_p \approx 380$ kA and $P_{NBH} \approx 200$ kW and have been published in reference [84]. The parallel peak heat flux ≈ 10 MWm^{-2} from the Langmuir probe is of the same order as the IR result ≈ 13 MWm^{-2} for a chosen sheath heat flux transmission factor $\gamma = 7$. Interestingly, the ion saturation current presents a double peaked structure, probably because of complex SOL physics such as drifts which were not included in the simulation [84]. The description of the physical processes involved in this doubled peak profile is beyond the scope of this thesis chapter.

In H-mode experiments, special care should be taken regarding the magnetic coordinates. Indeed, fluctuations in the strike point location can induce large broadening of the profile if the magnetic motion timescale is shorter than the averaging period chosen to run the four parameters fits. In H-mode and more generally in high plasma current discharges, the SOL width λ_q obtained from the Eich fit [37] can be quite narrow, as low as ≈ 2 mm in TCV [85]. Such a narrow SOL width increases the requirement for a fine spatial and temporal resolution.

In order to improve the spatial resolution, an attempt to fit data as a function of magnetic coordinate instead of fitting the data as a function real position (probe position) has been performed. The results were quite similar to the standard analysis performed on a short period, and therefore, the magnetic coordinate method has not become a standard analysis.

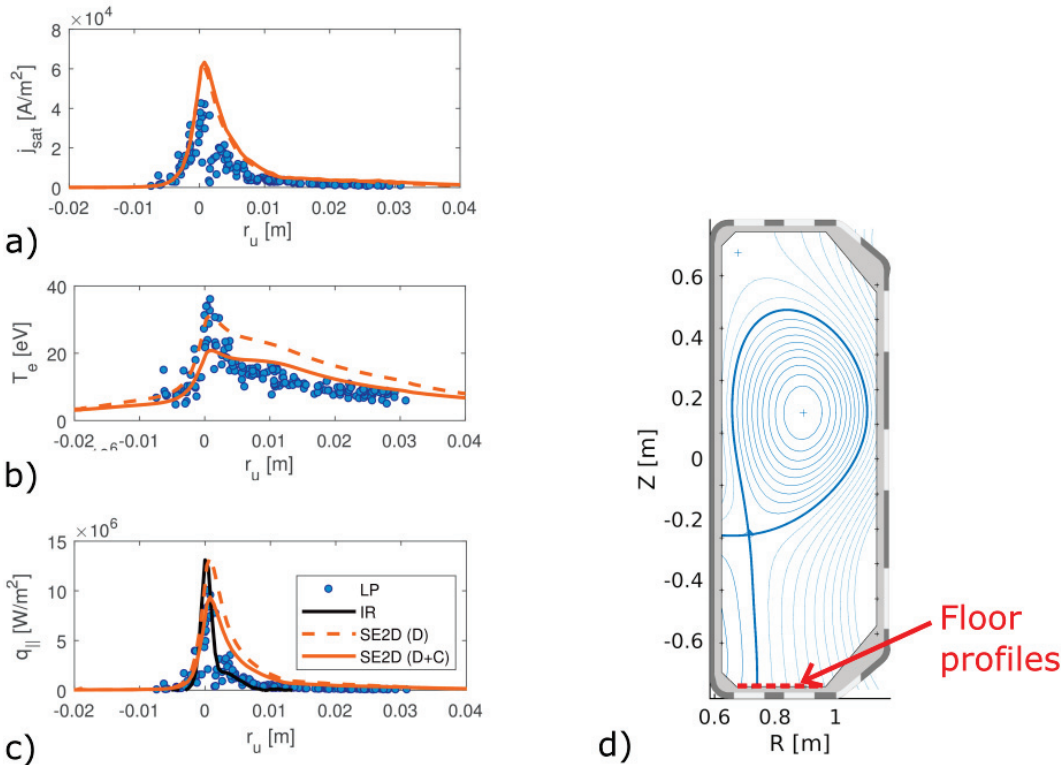

Figure 2.18: Examples of inter-ELM outer target profiles obtained from the LPs and comparisons to IR measurements and simulations with the SOLEDGE2D-EIRENE code for a 320kA Type-I ELMy H-mode (shot 58182) [84]: **a)** ion saturation current profile, **b)** electron temperature profile, **c)** parallel sheath heat flux profile. **d)** Magnetic equilibrium reconstruction at $t = 1.00\ s$ for the same experiment.

2.9 Conclusion

The TCV tokamak is equipped with a powerful system of wall-embedded Langmuir probes, providing a rich set of local measurement near the wall of time-averaged plasma parameters (J_{sat}, n_e, T_e, V_{fl}, V_{pl}, q, and ground current J_0) as well as turbulence resolved quantities (J_{sat}, V_{fl}, and J_0) [76] [51]. The present thesis work includes operation, maintenance and upgrades of this system [68]. In particular, the TCV wall probe coverage has been extended from 114 to 194 probes, including the coverage of the upper part of the vessel for Double-Null divertor studies, of the new divertor baffles, and in previously non-diagnosed regions in the lower divertor, notably the large major radius region. In order to operate all these probes simultaneously, rather than switching probe connections between different experiments, the array of Langmuir probe amplifiers has been extended from 48 to 216. Compared to the first generation amplifiers developed at the SPC-EPFL, the new set features a number of improvements [68]. The higher number of amplifiers operated simultaneously results in a larger failure rate, occurring mostly during off-normal events such as disruptions and ELMs.

Among the different solutions explored to date, the most efficient is the addition of extra resistors to avoid current surges in combination with surge protectors to avoid voltage spikes. Finally, the standard analysis for swept Langmuir probes on TCV [51] has been extended to obtain inter-ELM profiles in H-mode plasmas, achieved by an interactive tool to correctly filter out the ELM periods from the raw data.

3 Design, construction and commissioning of the Reciprocating Divertor Probe Array (RPDA)

In this chapter, the RDPA diagnostic is presented in detail, starting with a brief overview of similar existing systems in SEC. 3.1, followed by a quick introduction to the RDPA diagnostic in 3.2. The various design constraints are discussed in SEC. 3.3. The resulting engineering design fulfilling the aforementioned constraints is presented in SEC. 3.4. Relevant examples of experimental data are presented in SEC. 3.5. Future perspectives regarding possible hardware and theoretical improvements for the interpretation of the results are discussed in SEC. 3.6. Finally, a brief summary of the most relevant content from the chapter is given in SEC. 3.7.

In this chapter, the content of SEC. 3.3, SEC. 3.4 and SEC. 3.5 is largely based on a conference paper submitted to the journal Review of Scientific Instrument [86]. There are more details and figures given in this thesis chapter than in the paper because the strict 9 pages limit for the conference paper. Co-authors of the paper have agreed to share the content for the chapter of this thesis.

3.1 Overview of existing reciprocating divertor probes and probe arrays

As stated in SEC 1.7, RDPA is a new tool designed to provide $2D$ measurements of plasma quantities across a poloidal section of the divertor. In order to apprehend the similarities and the differences compared to previous systems, a non exhaustive overview of various divertor probes and LP arrays is given in this section.

The divertor and X-point regions of tokamaks have been diagnosed with fast reciprocating Langmuir probes, such as in DIII-D [87], Asdex Upgrade [88] [89] and JT-60U [90]. A rotating design in the toroidal plane was chosen for the former divertor probe in Asdex Upgrade [89]. However most of the recent designs rely on linear reciprocations [87] [88] [90].

The divertor probe from DIII-D [87] has been particularly influential for the design of RDPA. Both diagnostics share similar design features, such as the absence of an external vacuum system separated by a gate valve, contrary to what is usually the standard design choice for reciprocating probes at the outer mid-plane. The DIII-D probe also comes closest to providing $2D$ measurements in the tokamak divertor. The probe shaft consists of a cylindrical graphite structure with a diameter of $\approx 30\ mm$, undergoing a vertical reciprocation [87]. The radial range covered by the probe tips $\approx 20\ mm$ does not allow to scan the entire divertor leg within a single reciprocation. Therefore, sweeping of the magnetic equilibrium between repeat discharges combined with several reciprocations have been used to reconstruct 'reduced' $2D$ maps [91] [92].

Langmuir probe arrays have also been built in various machines. In the Caltech tokamak ($R = 45\ cm$, $a = 16\ cm$, $I_p = 20\ kA$), $1D$ and $2D$ arrays have been mounted on limiters at the outer-mid plane [93] and enabled one of the earliest studies performed to describe the plasma turbulence properties in the SOL. Another example of a similar system installed in the WEGA Stellarator is a $1D$ poloidal probe array undergoing a radial motion with 13 tips aligned to the flux surfaces [94]. In the divertor region of the large stellarator Wendelstein 7-X, several LP arrays have been mounted on a large reciprocating manipulator [95], aimed primarily to expose samples to reactor relevant target plasma conditions. The Wendelstein 7-X divertor manipulator can act as a limiter, intersect magnetic islands and/or the separatrix, depending on the depth setting. 2D Langmuir probe arrays are also used routines in basic plasma devices, such as TORPEX [96] and TJ-K [97].

3.2 Short presentation of RDPA

The Reciprocating Divertor Probe Array (RDPA), shown in FIG. 3.1, covers a $2D$ region in the poloidal plane of the TCV divertor by combining the fast vertical motion of a linear motor (up to 38 cm into the chamber) and a radial array of 12 rooftop Mach probes (1 cm radial resolution). The plunge duration is typically 0.35 s, the maximum speed can be as high as 2.5 m/s and the maximum acceleration reaches 80 m/s^2. The diagnostic structure, $\approx 4\ m$ high, is mounted on the TCV basement floor, as represented in the point **d)** in FIG. 3.1. The diagnostic has been built in the limited space ($\approx 5\ cm$ by $\approx 15\ cm$) available between the TCV toroidal coils.

FIG. 3.1 **a)** shows the probe head during assembly. The system installed in the TCV vacuum vessel is shown when fully deployed, see FIG. 3.1 **b)** and in rest position, see FIG. 3.1 **c)**. The dark grey parts of RDPA, with the same colour as the rest of the TCV walls in FIG. 3.1 **b)**, are graphite heat shields. The white parts shown in the same image are made from boron nitride, a refractory electrical insulation with low atomic number ($Z_B = 5$ and $Z_N = 7$). FIG. 3.1 **f)** shows a specially filtered snapshot ($D - \beta$ line from the MANTIS imaging system [64]) of the plasma at a time when RDPA is close to the maximum vertical position. Some plasma-probe interaction is clearly visible, as well as a characteristic shadow along the magnetic field, which

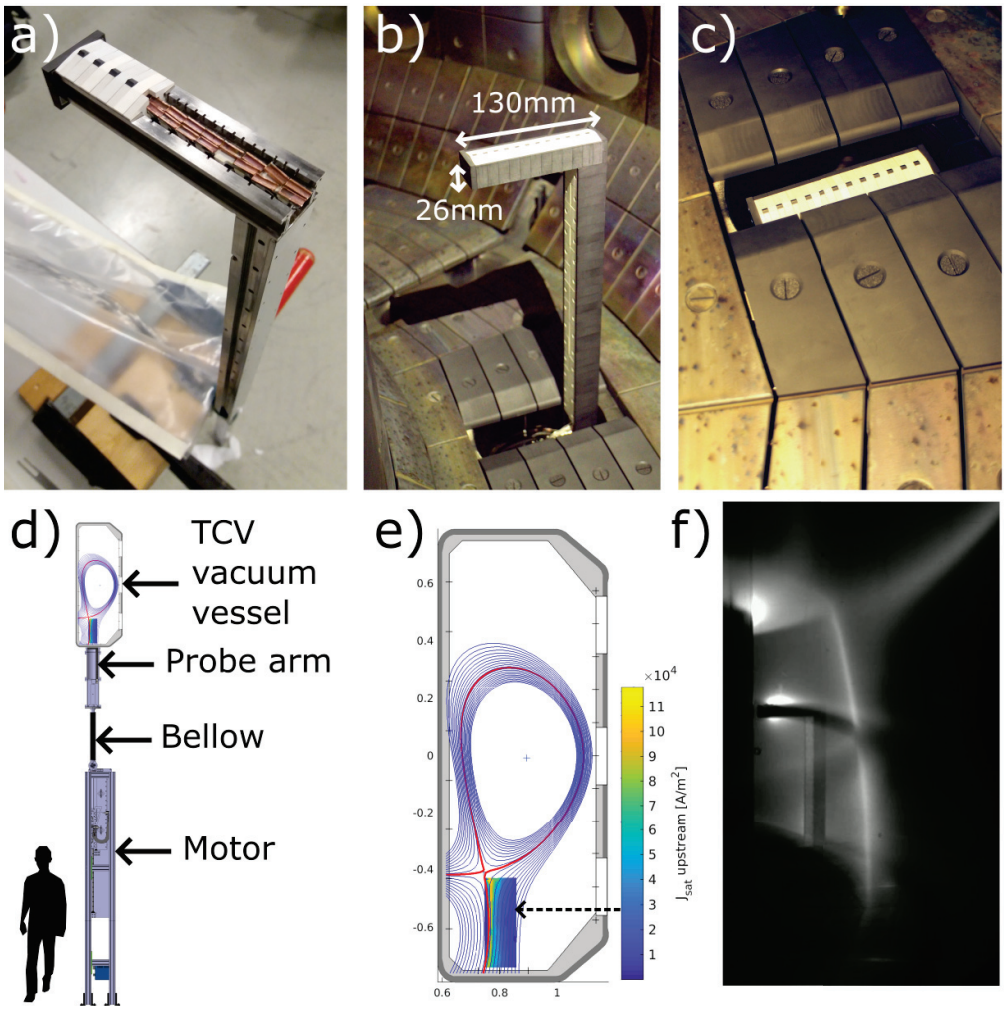

Figure 3.1: **a)** RDPA during assembly, **b)** RDPA inside the vacuum vessel at maximum height, **c)** RDPA inside the vacuum vessel in rest position, **d)** poloidal view of the entire diagnostic mounted in the TCV environment, **e)** example of a measured profile: ion saturation current density from the upstream RDPA probe tips, discharge #63023 and **f)** $D-\beta$ light snapshot recorded with the MANTIS camera system [64] of the RDPA plunge in a lower single null plasma, discharge #63023.

points mainly out of the image plane. FIG. 3.1 **e)** shows an example of the 2D measurements achieved with the RDPA, in this case time-averaged profiles of the ion saturation current density recorded by the upstream probe tips.

3.3 Main design constraints

In this section, after some considerations about probe tip geometry and bandwidth requirements, the main design constraints needed to minimize plasma perturbation by the probe,

to limit probe erosion and impurity release, and to assure probe integrity during off-normal events are presented.

3.3.1 Probe tip requirements for ion saturation and Mach number measurements

In a strongly magnetized plasma, the effective ion collection area of the probe is not computed as the total probe surface but rather as the projection of the probe surface in the direction of the magnetic field [70]. This approach is justified if the ion Larmor radius and the Debye length are smaller than the probe dimensions across the magnetic field.

The typical ion temperature in the TCV SOL is expected to be $T_i \approx 15\ eV$, the TCV magnetic field is $\approx 1.5\ T$ and we consider deuterium ions. The corresponding Larmor radius is:

$$\rho_{Larmor} = \frac{m_i \langle v_\perp \rangle}{eB} = \frac{\sqrt{\pi m_i T_i}}{\sqrt{2} eB} \approx 0.43\ mm,$$

where $\langle v_\perp \rangle$ is taken as the average norm of the velocity in a 2 dimensional Maxwellian distribution. It can be noted that the characteristic scale length of the Debye sheath (equal to a few times the Debye length [38]) is much smaller than the ion Larmor radius for typical TCV plasmas:

$$\lambda_{Sheath} \approx \lambda_{Debye} = \sqrt{\frac{\epsilon_0 e T_e}{n_e e^2}} \approx 0.01\ mm.$$

Probe tips heights of $1\ mm > 2\rho_{Larmor}$ have been chosen for RDPA. This $1\ mm$ dimension has also been historically used for dome shaped wall-embedded probes in TCV [51] [68] and enabled to obtain more consistent results than wall-embedded flush probes for various reasons (reduced sheath expansion, less relative error on the height of the probe tips and better signal to noise ratio for grazing magnetic field lines angles $\alpha \approx 0°$).

Probe tips must be split in two to allow for measurements of parallel Mach numbers [70], separating them in an upstream and a downstream part. The Gundestrup Mach probe design [98], [59], [99] would enable to obtain more information such as perpendicular flows but it has been discarded because it adds complexity to build an array of tightly packed probes.

3.3.2 Bandwidth requirements

Acquisition systems can be increasingly difficult to procure with increasing sampling frequency. Hence, determining the relevant sampling frequency is important during the diagnostic design phase. Most of the plasma fluctuations were found below $\approx 500\ kHz$ at TCV [100], in a study performed with a fast reciprocating probe with a fast acquisition sampling rate of $6\ MHz$. Therefore, an acquisition sampling frequency of $2\ MHz$ is believed to be sufficiently high in order resolve micro-turbulence fluctuation in the TCV SOL.

3.3.3 Spatial coverage requirements

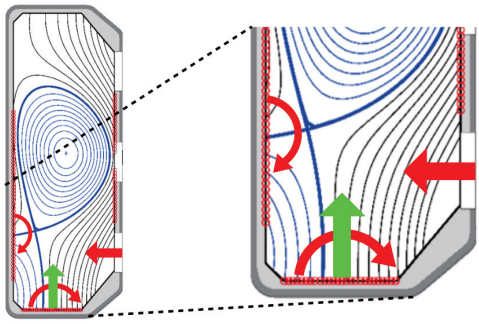

Figure 3.2: Different motions considered for RDPA.

Several probe motions are possible such as rotation [101], horizontal translation [88] and vertical translation [87]. See FIG. 3.2 for the different motions considered. A rotational system can hardly rest within the limited shadow of the TCV tiles, protruding only 20 mm above the vacuum vessel inner surface. Coverage of the inner divertor leg is therefore probably impossible to engineer. If the rotational system is installed in the largest port diameter available in the TCV divertor ($\approx$ 10 cm radius), it would be impossible to probe the X-point region. In the case of horizontal motions, the disadvantage is that the region near the target can not be covered because the lowest lateral ports axis at TCV are located 38 cm above the tiles on the machine floor.

Due to these limitations for the rotary and horizontal motions, a vertical motion for the divertor outer leg was considered optimal. The large vertical range combined with the TCV magnetic shaping capabilities provides highly flexible operation.

Multiple vertical probes at different radial positions (like a candelabra) would have been a possibility but self shadowing of the magnetic field lines behind the probe arm would have been an issue for a vertical divertor leg. Therefore, a radial array of probe tips mounted on a horizontal arm was found to be the best choice. This arm is held in place by a vertical shaft, as shown in FIG. 3.1 **a)**, and can be conveniently positioned in a place with little plasma interaction. The necessary radial dimension of this array is determined by experimental results on relevant TCV plasmas: the upstream e-folding lengths of the heat flux λ_q, the electron temperature λ_{T_e} and the density λ_n are usually found in the $2-20$ mm range [102]. This width increases in the divertor due to the geometry of the magnetic field (poloidal flux expansion by factors of $2-20$ [36]). Let us consider an intermediate case: $\lambda_u = 10$ mm and $f_x = 10$. If the outer divertor leg is vertical, the heat flux decay width at the target can be estimated as follows: $\lambda_{target} \approx \lambda_u * f_x = 100$ mm. Therefore the RDPA, radial coverage should be larger than ≈ 100 mm.

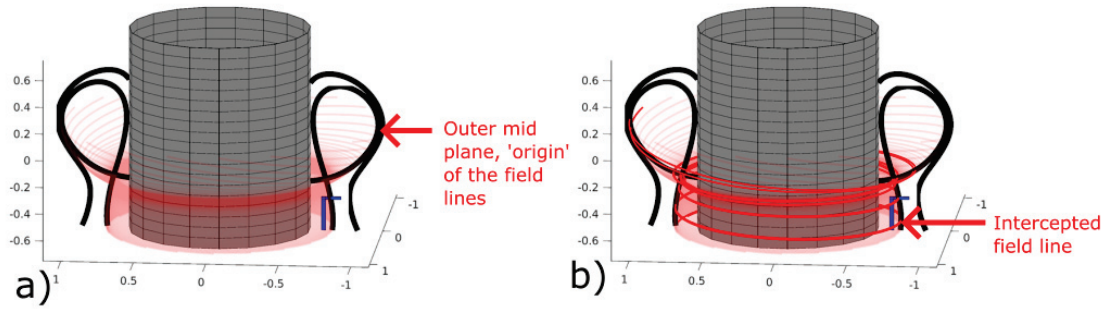

Figure 3.3: **a)** Magnetic field lines in the SOL from the mid plane to the outer target and **b)** highlighted magnetic field line intercepted by RDPA.

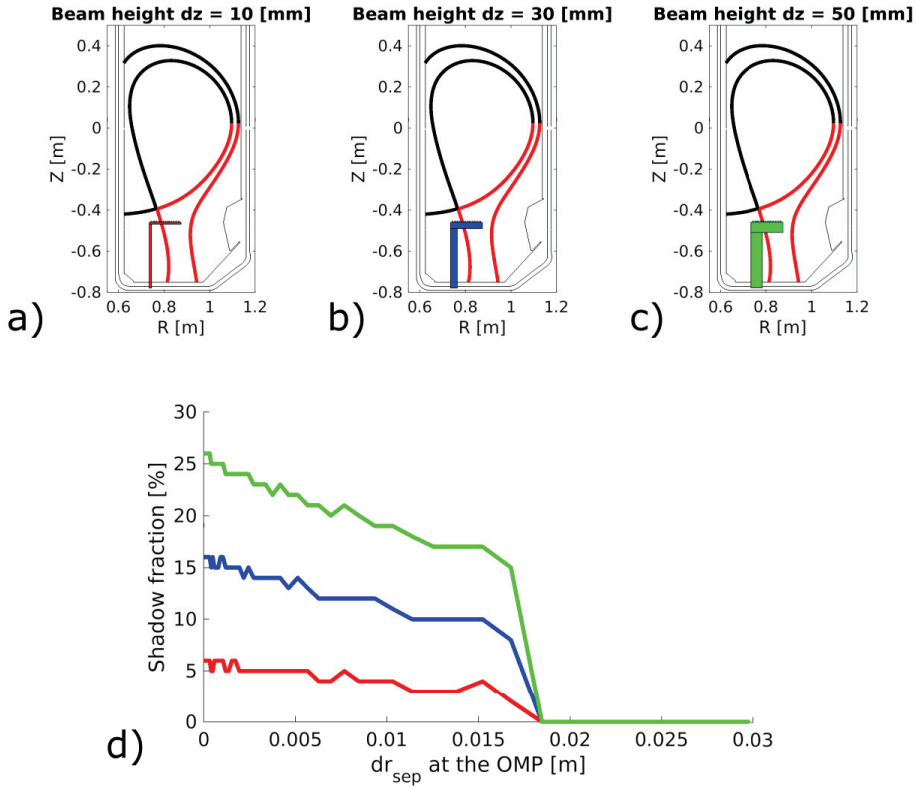

Figure 3.4: **a)**, **b)** and **c)**, illustration of different probe arm widths (10 mm, 30 mm and 50 mm) and the magnetic equilibrium chosen for the calculations and **d)** Calculated fractions of magnetic field lines being intercepted by the different probe arm.

3.3.4 Minimizing plasma perturbations: probe shadow and recycling

Heat and particles are expelled from the core plasma, predominantly at the outer mid plane and flow along the magnetic field to the wall, see FIG. 3.3 **a)**. This flow can be intercepted by

the probe, essentially generating a false floor, and thus perturbing the local plasma. In order to avoid unacceptable levels of perturbation, the fraction of intercepted field lines should be minimized, requiring a compact design.

In order to limit the fraction of intercepted field lines, an inverted L-shape has been chosen for the in-vessel structure of the probe, see FIG. 3.4: the vertical pole remains in the private plasma/far SOL (depending on the chosen orientation) and the horizontal beam hosts the radially distributed probe tip array. This geometry enables to strongly reduce the fraction of field lines intercepted by the probe body in the SOL. This fraction increases linearly with the vertical extent of the horizontal beam, see FIG. 3.4 **d)**. 15% shadowing, considered to be an acceptable fraction, requires a probe arm of not more than $\approx 3\ cm$ in width.

The shadowing fraction on a given flux surface becomes ≈ 100 % once the magnetic field lines are purely toroidal in the vicinity of the X-point. The perturbation caused by the RDPA measurement is therefore expected to be larger at the X-point than near the target.

3.3.5 Minimizing impurity release and material erosion

Plasma facing components must be built from refractory materials, such as graphite or tungsten, in order to avoid substantial impurity release causing dilution and radiation losses in the core plasma [103]. Solid materials must remain at a reasonable temperature, in order to avoid any melting or sublimation. In the present case, graphite is the preferred choice for plasma facing components because the entire TCV wall is currently covered with graphite tiles [104]. The grade chosen for the main heat shield of the RDPA is SGL® R6650, the same grade as the TCV wall [104]. This poly-crystalline graphite material has outstanding thermo-mechanical properties, thanks to its low porosity, around 10%, such as an excellent thermal conductivity, a relatively high tensile strength, and a low thermal expansion coefficient. It shows excellent thermal shock resistance and can be easily machined. The maximum service temperature is considered to be the onset of radiation enhanced thermal sublimation at $T_{surf} \approx 2200\ K$ [33]. The main drawback of graphite is the relatively high electrical conductivity that represents a risk in the presence of halo currents, as discussed later in Sec. 3.3. Therefore, some parts of RDPA must be made with refractory insulating materials. Most ceramics are unsuitable because manufacturing ceramic pieces with small radii is challenging due to the risk of cracking during machining, assembly and operation. Likewise, plastics are problematic because all organic based insulators have a limited service temperature, e.g. 700 K for the highest melting point of technical polymers such as polyimide. Muscovite mica sheets were found to resolve both the toughness and temperature concerns because this material can tolerate high service temperature $\approx 900\ K$ and can be easily cut to the appropriate shape with scissors.

In order to determine the adequate graphite heat shield thickness and the acceptable exposure times, $1D$ thermal analysis have been performed in this study. Precise material properties and heat flux values are required as inputs for the calculations. The thermal properties as a function of temperature for the SGL® R6650 graphite are shown in FIG. 3.5. In order to simplify

Graphite Grade SGL R6650

Properties considered constant as a function of temperature:

Density [kg/m3]	E modulus [Pa]	Poisson ratio []	Compressive strength [Pa]
1870	1.35E+10	0.25	1.50E+08

Nonlinear properties as a function of temperature:

Temperature [K]	Thermal expansion coefficient [1/K]	Tensile strength [Pa]	Flexural strength [Pa]	Heat capacity [J/(kg.K)]
2.000E+02	2.660E-06	3.660E+07	6.430E+07	1.780E+02
4.300E+02	3.200E-06	2.890E+07	6.610E+07	1.000E+03
6.000E+02	3.570E-06	2.600E+07	6.740E+07	1.394E+03
7.000E+02	3.750E-06	2.530E+07	6.830E+07	1.524E+03
8.000E+02	3.910E-06	2.520E+07	6.920E+07	1.633E+03
9.000E+02	4.050E-06	2.580E+07	7.020E+07	1.729E+03
1.050E+03	4.220E-06	2.760E+07	7.190E+07	1.830E+03
1.200E+03	4.360E-06	3.050E+07	7.380E+07	1.901E+03
1.350E+03	4.480E-06	3.420E+07	7.600E+07	1.953E+03
1.500E+03	4.590E-06	3.860E+07	7.850E+07	1.993E+03
1.700E+03	4.750E-06	4.520E+07	8.260E+07	2.035E+03
1.900E+03	4.900E-06	5.210E+07	8.750E+07	2.068E+03
2.150E+03	5.070E-06	6.070E+07	9.500E+07	2.100E+03
2.400E+03	5.200E-06	6.830E+07	1.040E+08	2.124E+03

Temperature [K]	Heat conductivity [W/(m.K)]	Emissivity []	Heat diffusivity [m2/s]	Thermal shock parameter [°C]
2.000E+02	9.350E+01	7.316E-01	2.810E-04	1.342E+03
4.300E+02	6.860E+01	7.316E-01	3.670E-05	1.147E+03
6.000E+02	5.790E+01	7.316E-01	2.220E-05	1.050E+03
7.000E+02	5.350E+01	7.316E-01	1.880E-05	1.011E+03
8.000E+02	5.020E+01	7.316E-01	1.640E-05	9.830E+02
9.000E+02	4.750E+01	7.316E-01	1.470E-05	9.630E+02
1.050E+03	4.440E+01	7.316E-01	1.300E-05	9.460E+02
1.200E+03	4.190E+01	7.316E-01	1.180E-05	9.400E+02
1.350E+03	3.970E+01	7.316E-01	1.090E-05	9.420E+02
1.500E+03	3.780E+01	7.408E-01	1.010E-05	9.500E+02
1.700E+03	3.560E+01	7.895E-01	9.360E-06	9.670E+02
1.900E+03	3.400E+01	8.079E-01	8.800E-06	9.930E+02
2.150E+03	3.280E+01	8.342E-01	8.360E-06	1.042E+03
2.400E+03	3.170E+01	8.590E-01	7.970E-06	1.113E+03

Figure 3.5: Temperature dependent properties of the Graphite Grade SGL® R6650. The data is reproduced from an internal report written at the Swiss Plasma Center [104] on the central column tiles of TCV.

calculations, and as proposed in a previous study [104], the graphite properties have been set to be constant as a function of temperature for the rest of this study by calculating the average quantities in the relevant temperature range $293\ K < T < 2000\ K$. The thermal conductivity is $\lambda_{average} = 47\ W/(m.K)$ and the heat capacity is $c_{average} = 1720\ J/(kg.K)$. In order to estimate the heat flux onto the probe body, the worst conditions were chosen: $T_e = T_i = 50\ eV$ and $n_e \approx 1.5 \cdot 10^{19} m^{-3}$ (measurements from Thomson scattering during an ELM-ing H-mode at the separatrix [105]). The transmitted power through the sheath, parallel to the magnetic field, is approximated with the following formula [38]:

$$q_{\parallel} = \gamma \cdot e \cdot T_e \cdot \Gamma \approx 25\ MW m^{-2}, \tag{3.1}$$

assuming $T_i = T_e$ and $\gamma = 6$ [72], and with Γ the particle flux density, defined as:

$$\Gamma = \frac{1}{2} n_e \cdot \sqrt{\frac{e \cdot (T_i + T_e)}{m_i}}. \tag{3.2}$$

The heat flux chosen for the calculations has been set above this result with some margin: $q_{\parallel} = 30\ MW m^{-2}$.

The results from a single simulation of the $1D$ model are shown in FIG.3.6 in the case of a $3\ mm$ thick shield, $0.3\ s$ plunge duration and perpendicular incidence of the magnetic field $q_{\parallel} = q_{\perp}$. In this example, the peak surface temperature of the graphite heat shield is $\approx 1730\ K$. The calculations have been performed for various shield thicknesses and various exposure times, see FIG. 3.7. As expected in case of inertial cooling, increasing the shield thickness is

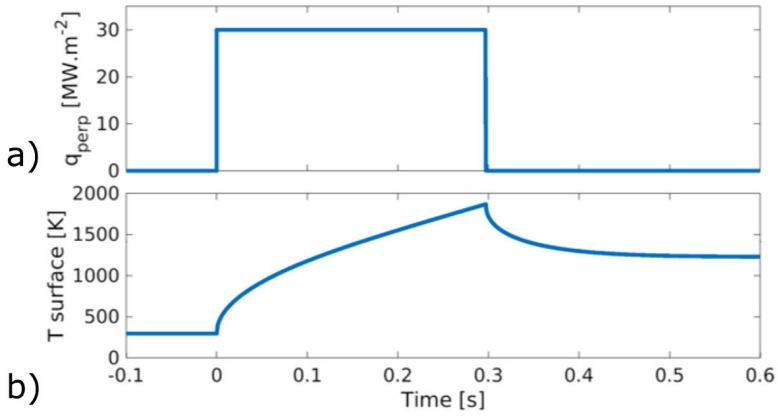

Figure 3.6: Output from the $1D$ model for the heat diffusion within the graphite thermal shield at a given shield thickness $d = 3\ mm$, plunge duration $t = 0.3\ s$, energy conservation of the simulation $E = 101.6$ %, heat flux $q_{\parallel} = 30\ MW.m^{-2}$, heat capacity $c_p = 1.72\ kJkg^{-1}K^{-1}$ and heat conductivity $\lambda = 47\ Wm^{-1}K^{-1}$. The applied heat flux as a function of time is shown in **a)** and the temperature at the graphite shield surface is shown in **b)**.

not sufficient to remain below the surface temperature limit. After a certain shield thickness, the reduction in surface temperature with increasing thickness is negligible, see the orange curve corresponding to the long plunge time $\delta t = 0.8\ s$ in FIG. 3.7. A relatively short exposure time and therefore a fast probe motion, less than $\delta t = 0.5\ s$, is therefore mandatory. The best compromise is found at $\delta t = 0.4\ s$ and shield thickness 2.5 mm.

In order to reciprocate within the 0.4 s allocated along the 0.38 m distance from the floor to the X-point, the necessary acceleration of the system is $a = 80\ m.s^{-2}$ and the necessary peak velocity is $v = 2.5\ m.s^{-1}$.

3.3.6 Ensuring probe integrity during off normal events

Off normal plasma events such as Edge Localized Modes (ELMs) and disruptions threaten the probe integrity. Although these events occur on the same timescale, disruptions are expected to be more hazardous due to the larger energy released per event. The first approach to avoid any damage from plasma disruptions is to operate far from stability limits. Nonetheless, disruptions are frequent and sometimes unpredictable in TCV experiments, so RDPA must be able to withstand a large number of disruptions. In typical tokamak disruptions, the sudden loss of energetic particle confinement, the thermal quench, is followed by a current quench due to the drop in plasma conductivity [106]. The current quench is the most hazardous to the probe integrity due to the large halo currents which dissipate some of the magnetic energy stored in the plasma. Halo currents are driven both by the time variation of the toroidal magnetic flux across the shrinking plasma poloidal cross-section and by the decay of the plasma current in the core [106]. The maximum halo current can amount to 50% of the pre-

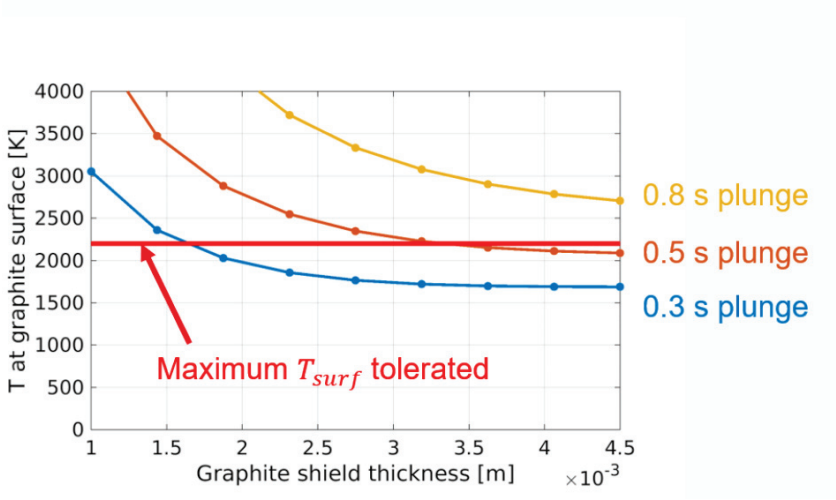

Figure 3.7: $1D$ model results for the heat diffusion within the graphite thermal shield for different graphite shield thicknesses and different plunge times. The y axis shows the maximum surface temperature, for an assumed heat flux of 30 $MW.m^{-2}$.

disruption plasma current [106], which can be as high as 500 kA in TCV. Once the plasma becomes more resistive than the vacuum vessel, the worry is that a substantial fraction of the current could be transferred from the plasma to the vessel through the probe arm.

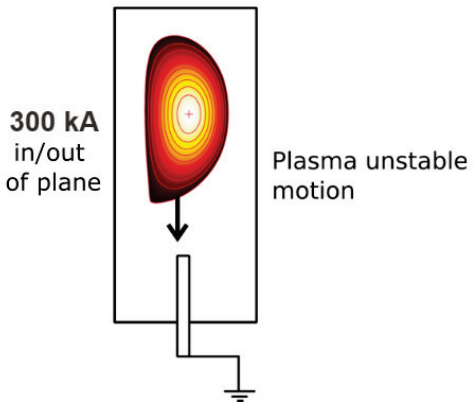

Figure 3.8: Grounded probe arm potentially in danger once the plasma undergoes an uncontrolled vertical motion during a disruption.

In the case where 5% of the overall plasma current in a typical experiment, with $I_p = 320\ kA$, would flow vertically in the RDPA structure, the corresponding Lorentz force would be:

$$\vec{F} = \vec{I} \times \vec{B}L = (15\ kA.1.5\ T.0.35\ m) \cdot \pm\vec{e_r} \approx 8400\ N \cdot \pm\vec{e_r}.$$

It becomes clear that such a large transversal force would damage the structure. Any electrical current path must therefore be interrupted between the plasma and the vacuum vessel. Thus, the graphite and metallic structure must be electrically insulated from each other. The electrical insulation must withstand the voltage difference without breaking down. The expected voltage is of the same order as the plasma loop voltage during the current quench:

$$U_{loop} = L\frac{dI}{dt} \approx 0.6\ \mu H \times 300\ kA/0.5\ ms \approx 360\ V,$$

where L is the inductance of a TCV plasma during the steady state phase of a typical inductive experiment (the actual inductance of the plasma is expected to change during the disruptive process).

3.3.7 Various external constraints

TCV baking

The baking temperature of the TCV vacuum vessel is $\approx 220\ ^{\circ}C$. Due to this high baking temperature, parts made of low melting point material such as tin, aluminum and polymers are forbidden due to the potential creep and out-gassing. Creep in polymers is particularly worrying in the case of electrical insulation washers, because the applied torque in the screw can be lost after the TCV baking. All electrical insulation washers must be made from creep free material such as ceramic materials (Muscovite mica sheet, aluminum nitride).

Magnetic field

The magnetic field in the toroidal coils is usually higher than $1\ T$, thus preventing the installation of any magnetic component such as an electrical motor very close to the plasma. Under the toroidal coils, the highest magnetic field is generated by the central solenoid and its direction is close to vertical. The vertical magnetic field is $\approx \pm 0.05\ T$ in the beginning of the discharge and is ramped up/down at $\approx \mp 0.05\ T/s$. This magnetic field is low enough to permit the use of magnetic components. However, the inductors present in electronic circuits are sometimes built with magnetic materials such as ferrite and can be affected by the ambient magnetic field. This issue can be solved for example with ferromagnetic plate shielding around the control electronics.

Space available below TCV

The space available is constrained by the port availability in TCV. Fortunately, there is less competition for the ports under the machine because access is more difficult and most diagnostics and heating systems are installed around the periphery of the machine. The ports available of the TCV vacuum vessel in the divertor region are represented in FIG. 3.9 **a)**. At the sector 4, shown in FIG. 3.9 **b)**, the vacuum port is centered at $R = 0.8\ m$ and has a diameter

$d = 150\ mm$, therefore sufficiently large to satisfy the radial coverage requirement presented in SEC. 3.3.3. Moreover, the vertical motion system must fit in the limited space between the toroidal coils, see FIG. 3.9 **b)**, located $\approx 0.7\ m$ below the vacuum vessel.

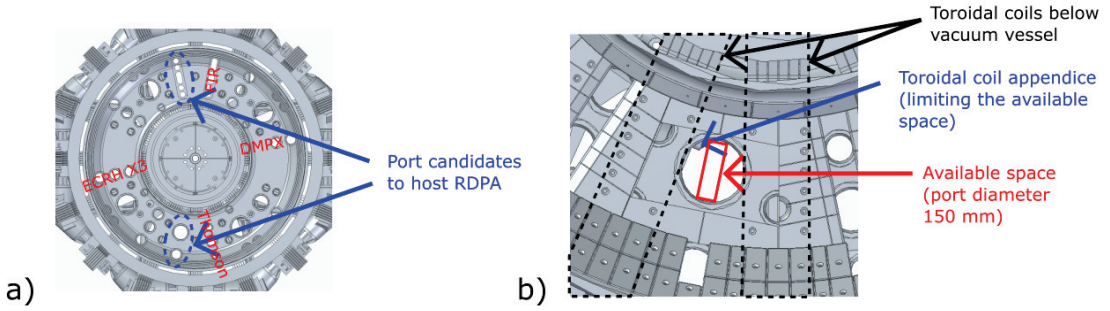

Figure 3.9: **a)** Top view of the TCV vacuum vessel floor with available ports and **b)** final choice for the RDPA position, the sector 4 port centered at $R = 0.8\ m$.

3.4 Probe design

The main conclusions drawn from the discussion in SEC. 3.3 are that the diagnostic motion must be fast, the probe arm must be as compact as possible while maintaining a critical thickness necessary for heat protection, and proper insulation is needed to avoid large currents to flow in the structure during disruption. The final engineering design that satisfies all these constraints is described in the following section.

3.4.1 Probe head design

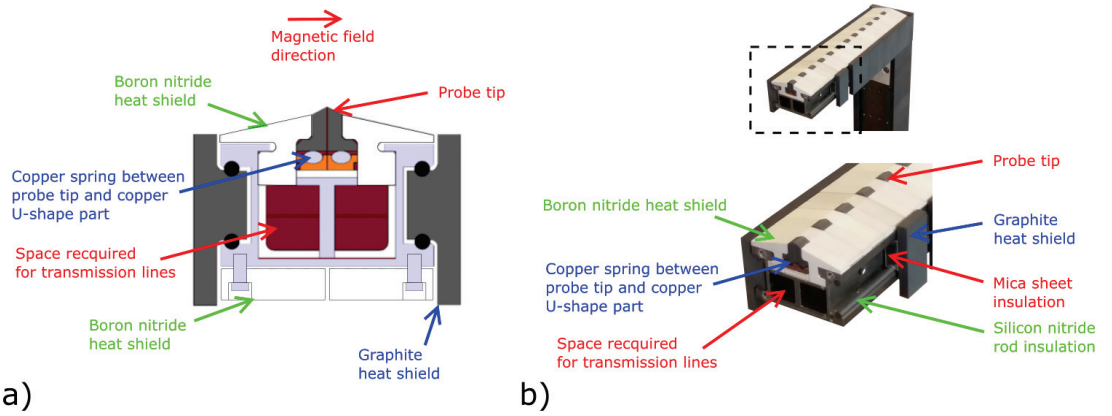

Figure 3.10: **a)** Drawing of the probe head cross section with labelled parts and **b)** picture of the probe head during the assembly.

The probe head is made of a titanium hollow structure in order to provide the highest stiffness to weight ratio possible. The hollow structure enables to host the 24 transmission lines, with

more details presented later in SEC. 3.4.4. If not in use, the probe head rests $\approx 2\ cm$ below the upper surface of the carbon floor tiles in order to avoid unnecessary damage from experiments unrelated to the diagnostic. Therefore the 38 cm plunge is actually only 36 cm in the plasma, just enough to reach the X-point for diverted plasma at $Z = 0\ m$. The horizontal beam height is 26 mm, as shown in FIG. 3.1 **c)**. Further reducing the beam height by a substantial amount is believed to be impossible while maintaining the same number of cables with the current design.

The only surfaces in contact with the plasma are the probe tips, the graphite and the boron nitride thermal shields. The thermal shields are slid radially in place during the probe assembly, as illustrated in FIG. 3.10 **b)**. The last shields at the extremities are screwed in place to secure the assembly. The tight tolerances and the friction in between parts is sufficient to avoid any jiggling motion. Probe tips are pushed upward by canted springs resting on copper parts, see FIG. 3.10 **a)**. The spring provides electrical contact to the transmission line conductors and ensures that the probe tip position relative to the boron nitride shield does not change.

Electrical insulation layers

In order to ensure proper protection from the halo currents discussed in SEC. 3.3.6, 5 different protections have been implemented: **1)** The grounded metallic structure of RDPA (connected to the tokamak ground voltage) is always maintained below the level of the floor in TCV, even for the maximum plunge height. **2)** The L-shaped titanium structure is disconnected from the rest of the diagnostic with electrically insulated screws, see FIG. 3.11 **a)**. **3)** The transmission lines are separated from the structure in a ceramic tubing inserted in both the vertical and horizontal parts of the L-shape structure. The horizontal section is shown FIG. 3.11 **b)**. This protection is required because the transmission lines outer jackets are connected to the tokamak ground in order to reduce capacitive and inductive effects for the measurements. **4)** The graphite thermal shield (electrically conductive) are insulated from the L-shaped titanium structure. The parts are mechanically linked through ceramic rods, as illustrated in FIG. 3.11 **b)**. The $\approx 1\ mm$ gap between the structure and the shield can fail to electrical insulate because an electrical arc can develop. However, the resistivity of the electrical arc is sufficiently high to limit the highest current excursions. **5)** All the graphite thermal shields (10 mm wide) are insulated from each other with mica sheet insulations. The shield voltages are therefore following the local floating potentials dictated by the plasma sheath condition.

Probe tips and anti arcing design

The probe tips are shown in FIG. 3.12. They protrude 1 mm above the boron nitride shields. A thin Muscovite mica sheet is inserted to insulate the upstream from the downstream Mach probe tips, see FIG. 3.12 **b)**. The probe tips have the so-called 'rooftop' shape with a reasonably low angle between the magnetic field and the surface in order to reduce the perpendicular heat flux. A significant heat sink volume is located below the surface: the probe tips are larger

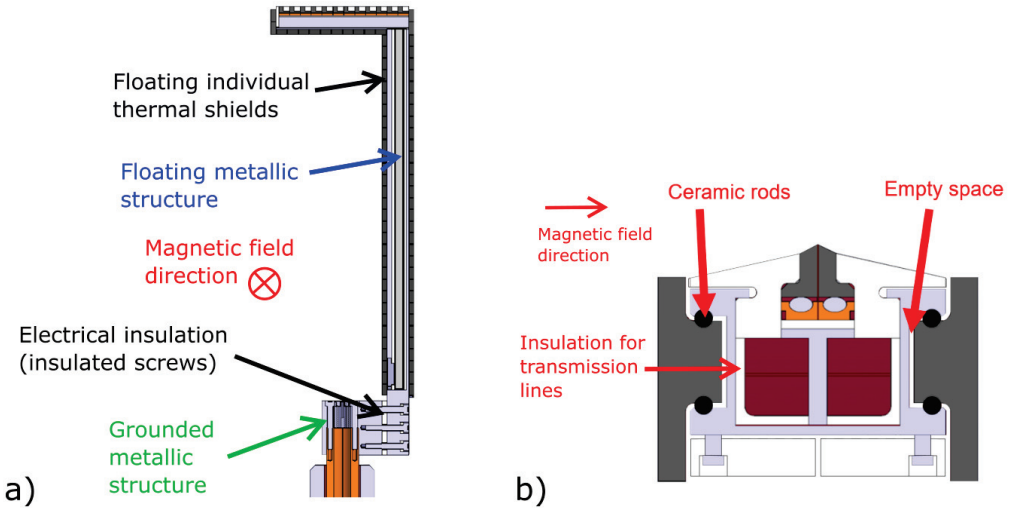

Figure 3.11: **a)** Cross sectional view of the L-shaped structure with the different parts labelled depending on their voltage reference and **b)** cross-sectional view of the RDPA beam with the insulation barrier between the structure and the thermal shields being highlighted.

below the surface than at the top, as shown in point **a)** in FIG. 3.10. The heat sink part of the probe tips is a parallelepiped volume, longer (10 mm) than the probe tips (4 mm) in the radial direction. This larger dimension enables to increase the number of electrical contact points with the canted copper spring located below the probe tip.

A significant issue that appeared during the first experiments is the phenomenon of probe tips "arcing": when a negative voltage is applied to the probe tips, a large transient current corresponding to electrons exiting the surface is collected instead of the standard incoming ion saturation current. Smoothing the probe tip edges with sandpaper, see 3.12 **c)**, has solved the problem. Since electron emission is possible only at high temperature and/or high electrical field [107], it is believed that the smoothing process helped by reducing the electrical field and the temperature at the tip of the conductor.

Graphite thermal shields

The lateral graphite heat shields are 2.5 mm thick, in accordance with the result from SEC. 3.3. The smallest machined radius is larger than ≈ 2 mm to avoid any stress concentration point. The shields at the horizontal probe arm extremities are split in two parts to facilitate thermal expansion and are screwed to the titanium structure. The screws were successfully electrically insulated with several washers made of Muscovite mica. The complex lateral and extremities shield shapes and the addition of holes for the screws could lead to thermal shock cracking. Thus, several design iterations have been performed to find the necessary distance ≈ 5 mm in between the critical region (screw holes and rod slots) and the surface exposed to the heat flux.

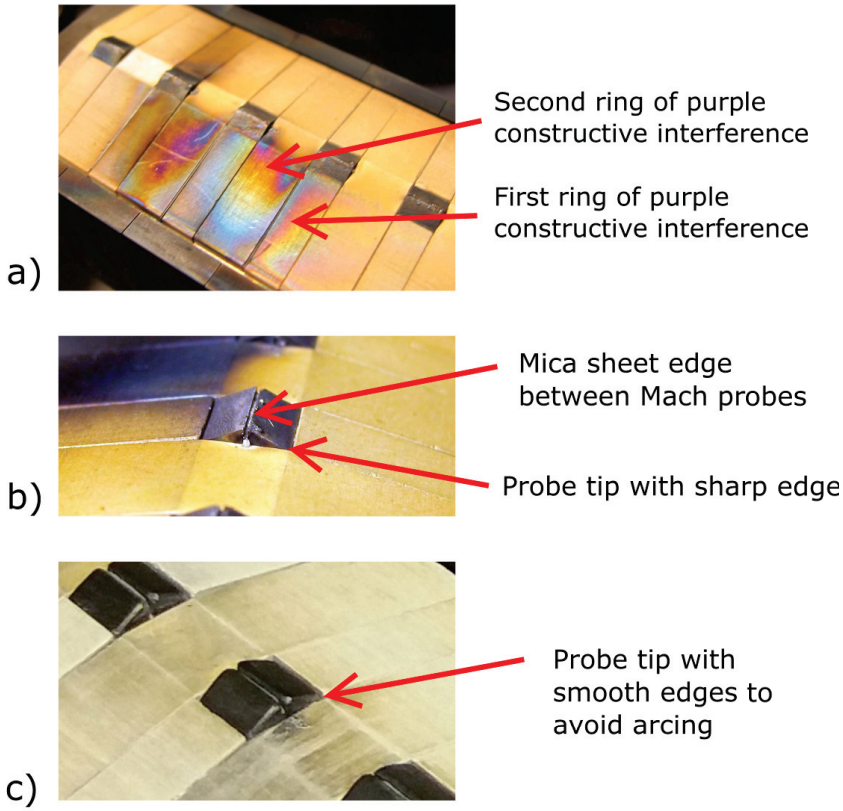

Figure 3.12: **a)** Picture of the RDPA probe tips after exposure to the plasma near the separatrix with the diffraction pattern caused by the carbon co-deposit, **b)** magnified picture of the Mach tips and the mica sheets and **c)** probe tips modified (edges have been rounded up to avoid arcing) ready for the next experimental campaign.

A thermo-mechanical analysis for the final design of both lateral and extremities shields with the software ANSYS® is shown in FIG. 3.13. The same exposure time $\Delta t = 0.3\ s$ and the same perpendicular heat flux input $q_{\parallel} = q_{\perp} = 30\ MW.m^{-2}$ were chosen as previously assumed in SEC. 3.3. The resulting surface temperature $T_{max} \approx 1440\ K$ was below the 2200 K limit (FIG. 3.13), the maximum tensile stress, $\sigma_{tension} \approx 15\ MPa$, below the 30 MPa limit (FIG. 3.14 **a)**) and the maximum compressive stress, $\sigma_{compression} \approx 84\ MPa$, below the 150 MPa limit (FIG. 3.14 **b)**). Stress limits for the graphite have been documented in the appendix, FIG. 3.5.

Boron nitride thermal shields

The boron nitride thermal shield surfaces have been designed to intercept field lines at a shallow angle, see FIG. 3.15 **a)**, in order to reduce the peak perpendicular heat flux to the surface from $q_{para} \approx 30\ MW.m^{-2}$ down to:

$$q_{perp} \approx q_{para} \cdot \sin\theta_{tot} \approx 12.2\ MW.m^{-2},$$

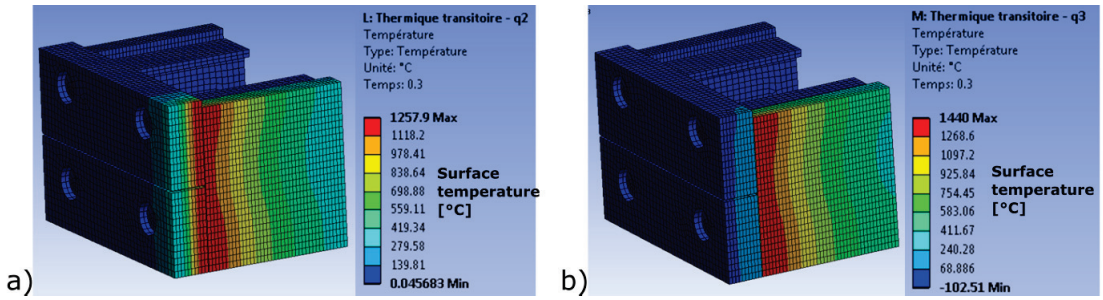

Figure 3.13: Thermal simulation performed with ANSYS® to determine the peak surface temperature on the graphite thermal shield. **a)** and **b)** represent two different positions of the heat flux corresponding to a different position of the outer divertor leg.

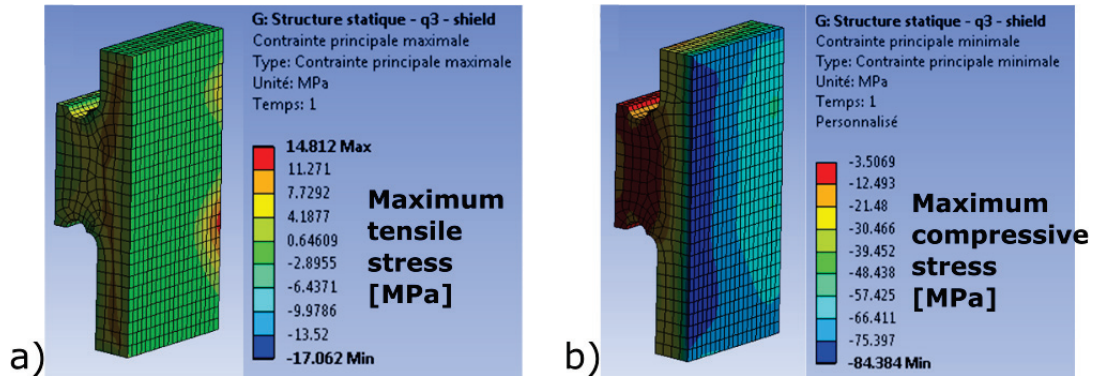

Figure 3.14: Thermo-mechanical simulation performed with ANSYS® to determine **a)** the peak tensile stress and **b)** the peak compressive stresses in the graphite thermal shield.

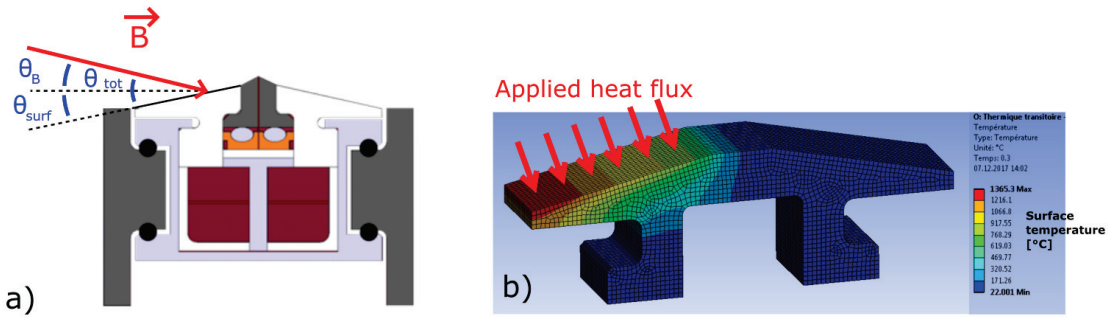

Figure 3.15: **a)** Cross-sectional view of the RDPA horizontal beam with the angle θ_{tot} between the magnetic field and the boron nitride shield surface and **b)** the thermal simulation result performed with ANSYS® to determine the peak surface temperature of the boron nitride thermal shield.

where $\theta_{tot} = \theta_B + \theta_{surf} \approx 24°$ is the highest angle possible between the inclined surface and the divertor magnetic field line.

An ANSYS® simulation has been performed to check if the peak temperature would stay below the maximum service temperature under such conditions. For this simulation, the material properties have been taken from the Combat® grade *A* hexagonal boron nitride data-sheet from Saint-Gobain®. The thermal conductivity is $k = 30\ W.m^{-1}.K^{-1}$ and the specific heat capacity is $C_p = 860\ J.kg^{-1}.K^{-1}$ in the simulation. However, it was decided in a later stage that the higher purity hexagonal boron nitride grade HeBoSint® PL 100 from Henze® (< 1%[*w*/*w*] oxygen content) would be the definitive material candidate. The actual high purity boron nitride used has similar thermal properties: the thermal conductivity is $k = 20\ W.m^{-1}.K^{-1}$ and the specific heat capacity is $C_p = 500\ J.kg^{-1}.K^{-1}$. The maximum service temperature for the HeBoSint® PL 100 boron nitride is $T_{max} \approx 2600\ K$. The maximum calculated temperature after the plunge, $T \approx 1365\ ^\circ C$, is lower than the maximum service temperature according to the simulation, see FIG. 3.15 **b)**. As expected, the highest temperature is located at the tip of the shield, where the shield is the thinnest.

It was initially believed that the deuterium ion flux from the plasma could lead to premature erosion of the boron nitride parts and lead to plasma contamination. However it was found experimentally that erosion of the boron nitride was absent and instead a deposited layer of carbon was found on the boron nitride surface, as shown in FIG. 3.12 **a)** and **b)**. Concentric rings of the entire visible spectrum are reflected, and the thickest deposit corresponds to the second purple ring of reflected light, as shown in FIG. 3.12 **a)**. Using Snell's law, the expected deposited thickness can be computed for the constructive interference of the purple reflected light:

$$d = \frac{m\lambda}{2n\cos(\theta)} \approx 400\ nm,$$

where the carbon deposit index of refraction is assumed to be equal to the refraction index of amorphous graphite $n \approx 1.5$ [108] (the actual refraction index is expected to depend on the porosity fraction and on the hydrogen content of the carbon deposit), the incident angle of the light is chosen to be intermediate, $\theta = 45\ ^\circ$, the wavelength of the purple color is $\lambda = 430\ nm$ and the integer number $m = 2$ corresponds to the second diffraction pattern ring. The reflected light at the air/carbon deposit interface and at the carbon deposit/boron nitride surface are both assumed to undergo 180° phase shifts because of the increasing refractive index values [108] [109]: $n_{air} = 1 < n_{carbon} \approx 1.5 < n_{BN} \approx 2.1$. The layer of carbon rich residue in this figure has been deposited over the course of ≈ 15 experiments corresponding to ≈ 6 *s* of plasma exposure and ≈ 3 *s* in ion saturation mode. The thickness deposited, ≈ 400 *nm*, is consistent with a deuterium ion flux density $\Gamma_{D_2} = 6.25e23\ m^{-2}.s^{-1}$ and a carbon ion flux density of $\Gamma_C = 2.5e22\ m^{-2}.s^{-1}$ with a 100% chance of deposition for the carbon atom upon contact with the surface and assuming that the deposited carbon is porous with ≈ 30 % of empty space.

The absence of boron nitride erosion could be explained by the high stability of boron nitride against chemical erosion by deuterium ions due to the strong chemical bond between boron and nitrogen atoms [110].

3.4.2 Out-of-vessel mechanical structure and vacuum assembly

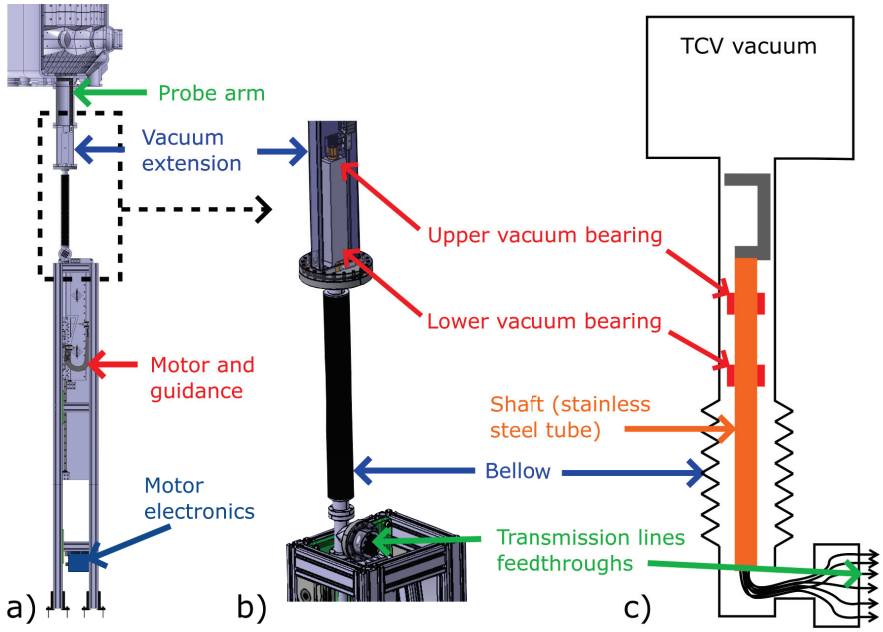

Figure 3.16: **a)** RDPA complete structure, **b)** close up of the parts near the bellow and **c)** simplified sketch of the vacuum assembly cross-sectional view.

The outer structure of the RDPA is made of vertical aluminum profiles and is bolted to the TCV concrete ground floor, almost 4.5 m below the vacuum vessel, see FIG. 3.16 **a)**. The outer structure is covered with transparent plastic panels to avoid any accident. An additional safety system is a 12 V line that triggers an emergency stop (disconnect the motor electrical power supply) if a single plastic panel is removed from the structure.

The structure supports a thick aluminum plate on which the motor and guidance systems are mounted. 2 THK® linear bearings $HSR\,20\,R$ ensure the guidance of the vertical motion. An electrical brake Zimmer® $LCE2001AS1-01$ clamps the rail of the linear bearings when the motor controller is turned off in order to avoid any motion. The force on the brake is usually less than 40 N because the weight of the moving assembly is almost entirely offset by the atmospheric pressure subjected to the bellow (force proportional to the bellow cross-sectional area).

Guidance of the motion inside the vacuum is assured by $PEEK$ bearings $\approx 30\ cm$ apart from each other, see FIG. 3.16 **b)** and **c)**. The $PEEK$ bearings are located in a region of the vacuum vessel which remains at room temperature during the baking process. Radial misalignment of up to $\approx 3\ mm$ are tolerated between the vacuum vessel and the RDPA structure thanks to the flexibility of the RDPA shaft. Beyond 3 mm, the friction on the $PEEK$ bearings inside the vacuum becomes unacceptable for a smooth motion. The vacuum vessel expands during the TCV bake and therefore, fast motions are not recommended when the vessel is still warm due to the radial misalignment.

It was not possible to install a vacuum gate valve in between the TCV vacuum and the probe vacuum due to the space limitation from the toroidal coils. Instead, the diagnostic vacuum relies on the tokamak turbo pumps (same situation for glow antennas for example), see FIG. 3.16 **c)**. Relying on the TCV vacuum constitutes a certain risk because any error or malfunction of the system could lead to failure of the tokamak vacuum. The feedthroughs for the 24 transmission lines are ceramic insulated SMA connectors and were assembled and welded to a custom designed vacuum flange. After several weeks of testing, frequent vacuum electrical discharge (between the conductors of the transmission lines and the tokamak ground inside the SMA connectors) were observed. The problem was later solved with additional electrical insulation jackets around the SMA conductor.

3.4.3 Motion system

Part	Mass [g]
Aerotech® linear motor moving part BLMX-502-B-AC-H-S-750	4100
Stop plate (end of travel)	397
Connection part between linear motor and linear bearings	1840
THK® Linear bearings HSR 20 R (X2)	500
Zimmer® electrical brake LCE2001AS1-01	1117
Renishaw® scale for optical encoder A-9661-0480	92
Coupling between linear motor and vacuum assembly	1143
Vacom® CF flange coupling	462
Vacom® CF tee flange TE38RS-316LNS	910
Vacom® CF reducer flange ZL6340-316KNS	1140
Vertical feedthroughs support	89
Feedthroughs support extension for 24 Vacom® VB-SMA2	129
Vacom® Flange 63 [mm] (welded to feedthroughs support extension)	312
24 Thermocoax® cables 1 Zs Ac 10	500
Vacom® CF flange connection bellow and shaft	649
RDPA shaft	4224
Vacom® edge welded bellow	500
Connection between RDPA shaft and RDPA probe arm	290
RDPA probe arm (including all plasma facing components)	1027
Total	19421

Figure 3.17: Masses of all the moving components of the RDPA diagnostic.

The choice of a linear electrical motor with permanent magnets was motivated by the recent success of a similar system on the Alcator C-Mod tokamak [55]. Linear motors have several advantages over pneumatic systems: better position control, more flexibility in the choice of the trajectory, better reproducibility in between identical plunge motion and less auxiliary systems required. Position is monitored in real time by the motor controller using inputs from a Renishaw® optical encoder with sub-mm accuracy. Aerotech® BLMX 502 motor was chosen for RDPA because of the large trust $4400N$ developed in the relevant speed range considered, $2-3\ ms^{-1}$. The sum of all the masses of the moving parts of the RDPA diagnostic is $\approx 20\ kg$, as shown in FIG. 3.17. The maximum theoretical acceleration $a = \frac{F}{m} \approx \frac{4400\ N}{19.4\ kg} = 227\ m.s^{-2}$ is therefore sufficient for the reference motion ($L = 0.38\ m$, $a = 80\ ms^{-2}$ and $v = 2.5\ ms^{-2}$) determined in SEC. 3.3.5.

At the time of writing, the maximum acceleration is not limited by the motor specifications but rather by the electrical connection to the power supply. The motor controller Soloist® HPe 100 (100 means 100 A peak DC current) can be fed either with the three phase US grid voltage $AC110\ V$ or to a single phase European grid voltage $AC220\ V$. In order to avoid the installation of a large transformer in the TCV zone (necessary to convert the 3 phase European voltage $AC220\ V$ down to the US standard), it was decided that the motor controller should be supplied with a single phase 35 A European voltage $AC220\ V$. The AC voltage is rectified in the motor controller where some energy is stored in a capacitor bank. This capacitor bank does not store enough energy for several reciprocations: it was experimentally seen that the system could no longer apply the desired voltage after the 4^{th} plunge with the reference motion.

3.4.4 Transmission lines

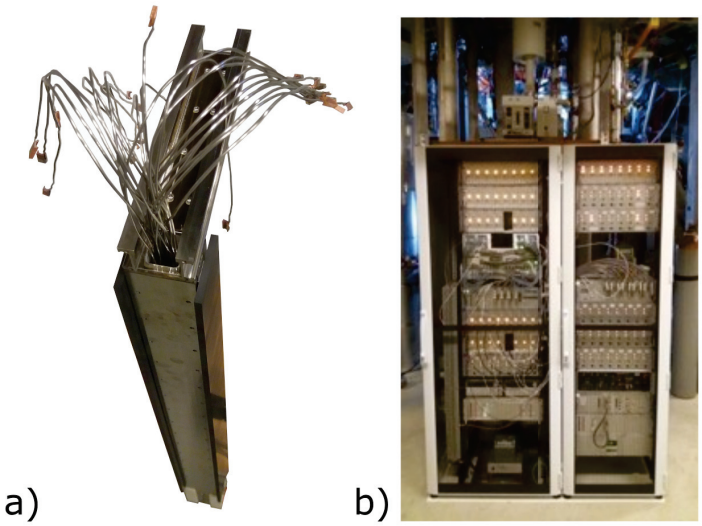

Figure 3.18: **a)** Assembly phase of the Thermocoax® lines in the RDPA probe arm and **b)** electronics cubicles with acquisition and Langmuir probes amplifiers at the TCV basement.

The transmission lines consist of $\approx 8\ m$ of standard coaxial cables outside the machine (at atmospheric pressure) and $\approx 2\ m$ of Thermocoax® cables inside the machine (in the TCV vacuum). The assembly phase of the Thermocoax® is shown in FIG. 3.18 **a)**. The assembly process is tedious and the transmission line would benefit from a redesign for a future version of the diagnostic.

The line outside the machine has a 50 Ω impedance, a DC resistance $R_1 \approx 1.48\ \Omega$, an inductance $L_1 \approx 9.4\ \mu H$ and a capacitance $C_1 \approx 0.67\ nF$. The line inside the vacuum has a $\approx 20\Omega$ impedance, a DC resistance $R_2 = 1\ \Omega$, an inductance $L_2 \approx 2\ m * 0.78\ \mu H/m = 1.56\ \mu H$ and a capacitance $C_2 \approx 2\ m * 0.61\ nF/m = 1.22\ nF$. The mismatch in line impedance is not expected to affect the time dependent measurement [68] (impedance matching only becomes relevant at higher frequencies, e.g. $> 5\ MHz$). The electrical contact between the graphite probe

tips and the Thermocoax® conductor contributes to the overall resistance by adding a DC resistance $R3 \approx 1\Omega$. This DC resistance value comes from a copper spring placed around the nickel alloy spring in between the graphite probe tips and the copper inner conductor of the Thermocoax® cable. The copper spring is prone to creep at temperatures above $\approx 700\ K$ and therefore can lose its original shape when the neighbouring probe tips are subjected to intense plasma heat flux. Therefore, the nickel alloy spring is required to hold the shape of the copper spring. This solution of adding a second copper spring around the nickel alloy spring is not ideal because it can lead to dissimilarities of the DC resistance between different lines. The overall DC resistance, inductance and capacitance are $R \approx 3.58\ \Omega$, $L \approx 10.96\ \mu H$ and $C \approx 1.89\ nF$. The large DC resistance $R \approx 3.58\ \Omega$ (compared to $\approx 1.4\ \Omega$ for wall embedded probes [68]) is problematic in the case of low electron temperature measurements [51]. The most straightforward improvements would be to use thicker coaxial inner conductors for the line outside of the machine and to coat the nickel alloy spring with a sufficiently thick copper conducting layer in order to bring the overall DC resistance of the line down to $R \approx R_2 = 1\ \Omega$.

The transmission lines end at the electronics cubicles, see point **b)** in FIG. 3.18 where the $2\ Mhz$ acquisitions and the custom built amplifiers are located [68].

3.5 Example results

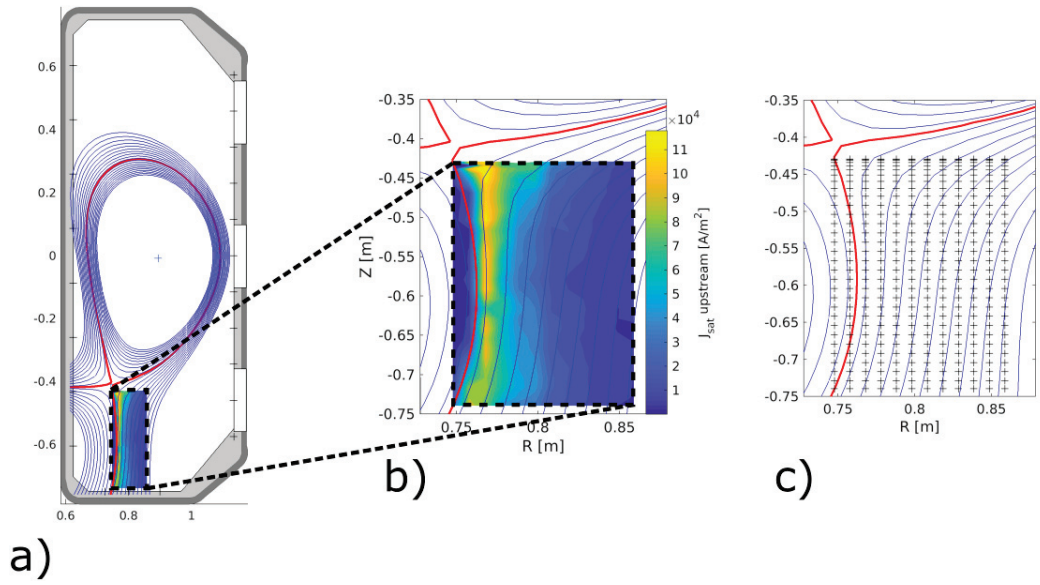

Figure 3.19: **a)** Poloidal plane view of the TCV wall, vacuum vessel and the plasma magnetic equilibrium. **b)** Focus on the RDPA coverage. A contour color plot is given here as an example for the ion saturation current density. **c)** A grid has been plotted to explicitly display the positions of the data points from **b)**.

$2D$ plots of the plasma quantities in the poloidal plane have been reconstructed, using a colour map for the scale. In the following, some example results are presented.

One of the most straightforward plasma quantity that can be derived from Langmuir probe analysis is the ion saturation current density, shown for the upstream probe tips in FIG. 3.19 **a)** and **b)**. The aspect ratio between the Z and the R coordinates is conserved in FIG. 3.19 **a)**. However, in the upcoming result examples, the aspect ratio is not conserved, see FIG. 3.19 **b)**, in order to highlight the gradients along the vertical direction (in the flux surface plane) relative to the gradients in the radial direction (normal to the flux surface plane).

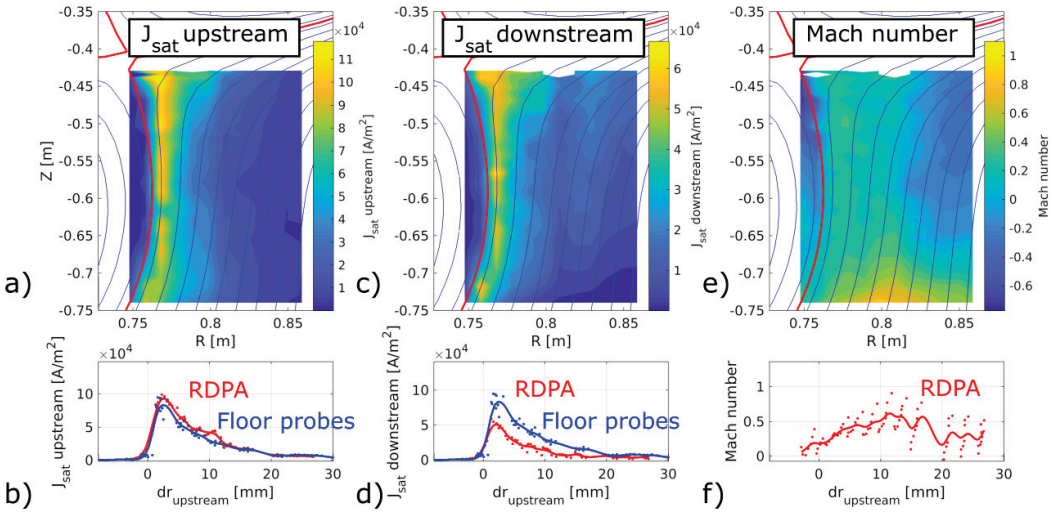

Figure 3.20: **a)** ion saturation current density for the upstream RDPA probe tips in the shot #63029 (L-mode, $I_p = 320\ kA$, unfavourable field direction for H-mode access) and **b)** comparison near the target with the wall-embedded probe measurements. **c)** and **d)** ion saturation current density for the downstream RDPA probe tips. **e)** Mach number computed from the ratio between upstream and downstream ion saturation currents and **f)** Mach number values near the target.

The upstream ion saturation current density is usually in agreement with the wall-embedded probe profile, see FIG. 3.20 **a)**. The downstream signal is usually lower than the upstream signal, see 3.20 **b)**, indicating a net ion flow towards the target. The ratio between the upstream and downstream signals enables to calculate the Mach number, see FIG. 3.20 **c)**, with the following expression [70]:

$$M = \ln\left(\frac{J_{sat,upstream}}{J_{sat,downstream}}\right)/2.2$$

In general, subsonic Mach numbers are measured $M < 0.8$. Negative Mach numbers have also been measured locally $-0.4 < M < 0$, corresponding to a parallel ion flux going away from the target, caused by either $E \times B$ drifts or when the measurement is performed near the X-point, above the ionisation front.

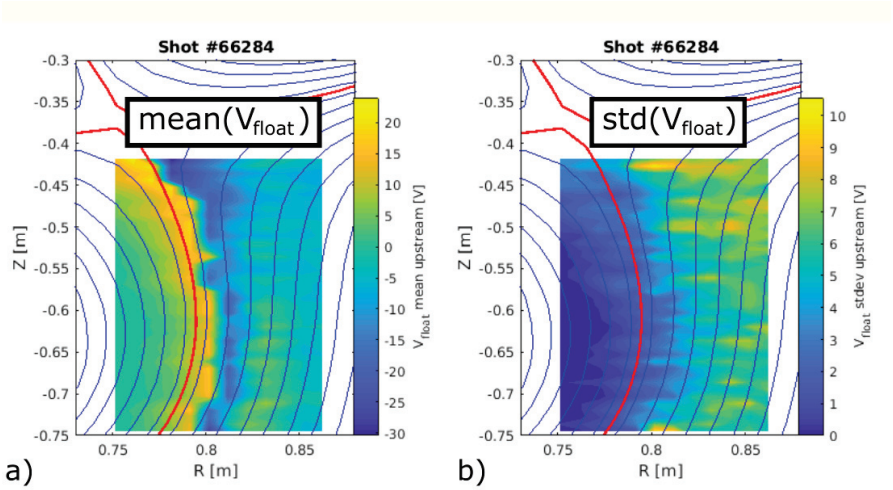

Figure 3.21: **a)** Time averaged floating potential measured by the upstream tips of RDPA for the shot #66284 (L-mode, $I_p = 160\ kA$, $\langle n_e \rangle / n_{gr} = 0.27$, favourable field direction for H-mode access) and **b)** standard deviation of the floating potential for the same case.

The floating potential, FIG. 3.21 **a)**, can be measured at the acquisition sampling frequency of 2 MHz. The standard deviation of the signal, see FIG. 3.21 **b)**, can be used as a proxy for the fluctuation level at the micro-turbulence timescale.

Sweeping of the probe voltage enables to determine time averaged quantities such as the electron temperature. The results have been obtained with a 4 parameters fit of the IV curve [51] (see also EQ. (2.9)). In the example shown in FIG. 3.22, the upstream and downstream electron temperature profiles agree with both the Thomson scattering measurement near the X-point and with the wall-embedded LPs at the target. The difference between the upstream and downstream temperature is relatively small, which is a necessary criterion for the validity of the Mach probe model [70] used to interpret plasma flows (this model has been derived based on the assumption of an isothermal plasma).

Another quantity that can be obtained with the diagnostic is the plasma potential. The plasma potential is an important quantity, e.g. to estimate the velocity of the $E \times B$ drift, which can be a key player in the particle and heat balance [92] [111]. The plasma potential measurement has been obtained from sheath theory [38]:

$$V_{pl} = (V_{fl,downstream} + V_{fl,upstream})/2 + 3T_{e,upstream},$$

where $T_{e,upstream} \approx T_{e,downstream}$ is expressed in $[eV]$. The theoretical constant ≈ 3 corresponds to a deuterium plasma with $T_e \approx T_i$ and with negligible coefficient of secondary electron emission [38]. The average between the upstream and downstream probes floating potential values is taken for the floating potential value in order to obtain a quantitative agreement with the V_{pl} target profiles, as shown in FIG. 3.23 **a)**. The derivation of a theoretical model would be required to interpret the asymmetries often seen between the downstream

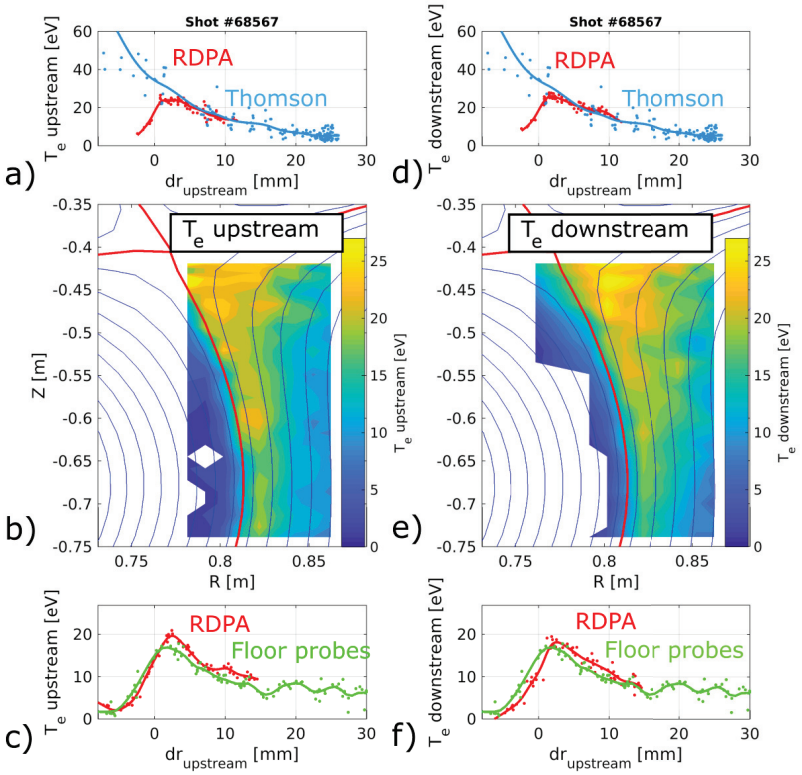

Figure 3.22: **a)** , **b)** and **c)** Electron measurement from the upstream RDPA probe tips compared with Thomson scattering measurements **a)** near the X-point and with wall-embedded probes **c)** near the target for the shot #68567 (L-mode, $I_p = 160\ kA$, $\langle n_e \rangle / n_{gr} = 0.26$, unfavourable field direction for H-mode access). **d)** , **e)** and **f)** same profiles for the downstream RDPA probe tips.

and upstream floating potentials, suspected to be caused by electrical currents in the divertor plasma, see SEC. 3.6.

3.6 Future hardware improvements and theoretical models requirements

3.6.1 Asymmetric floating potential and asymmetric electrical current drawn with grounded probes: an opportunity for an interpretative model ?

A large difference between the upstream and the downstream ground current is often seen in experiments, see FIG. 3.24 **a)** and **b)**. The same observation holds for the floating potential, see FIG. 3.24 **c)** and **d)**. This asymmetry potentially holds relevant information about the plasma properties that could be used in an interpretative model. The mismatch between upstream

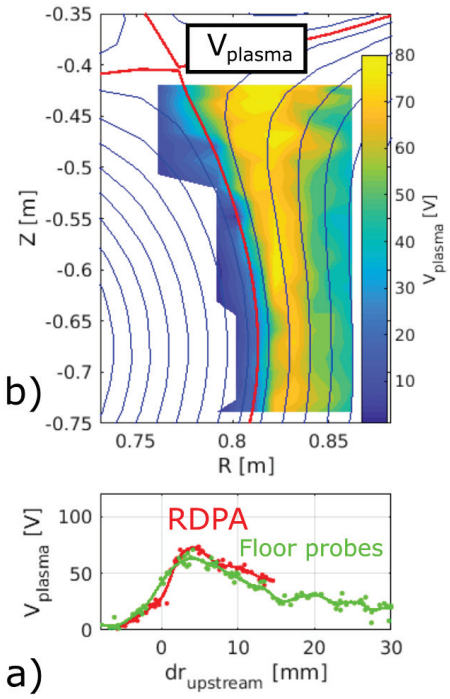

Figure 3.23: **a)** Time averaged plasma potential from RDPA (average between the upstream and the downstream plasma potentials) for the shot #68567 (L-mode, $I_p = 160\ kA$, $\langle n_e \rangle / n_{gr} = 0.26$, unfavourable field direction for H-mode access) and **b)** comparison between RDPA data near the target and the plasma potential from the wall-embedded probes.

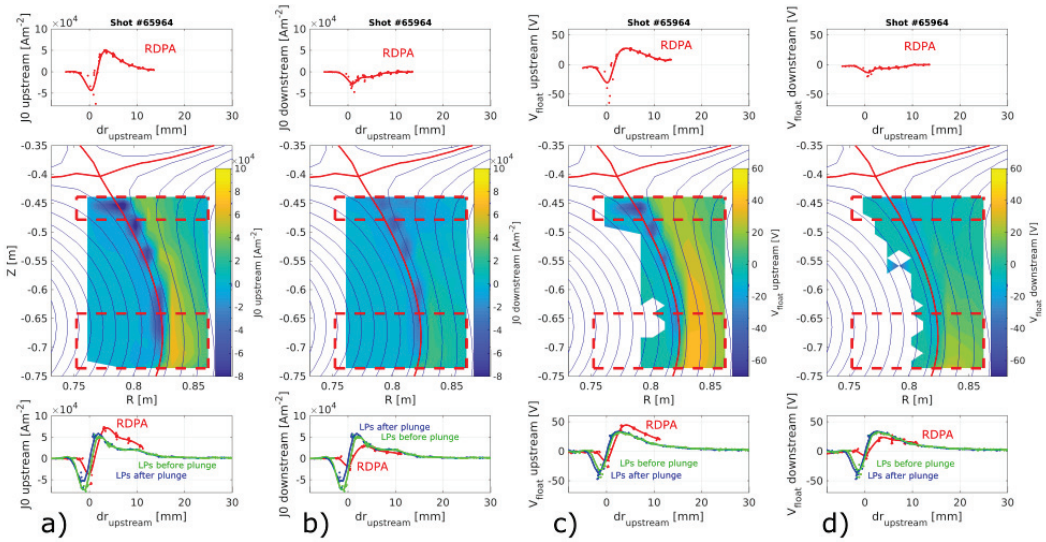

Figure 3.24: **a)** Upstream J_0, **b)** downstream J_0, **c)** upstream V_{fl} and **d)** downstream V_{fl} profiles for the discharge 65964 ($\langle n \rangle \approx 5.0e19[m^{-3}]$).

and downstream J_0 and V_{fl} is relatively less important for discharges with high core density (not shown here), possibly because the low electron temperature region near the target, which is highly electrically resistive, restricts the electrical current values. Discharges in forward field (favorable H-mode access) have also shown some asymmetries between upstream and downstream floating potentials (not shown here).

Unfortunately, to our knowledge, no model exists which could relate these J_0 and V_{fl} asymmetries to local plasma parameters, such as potentially the parallel current densities in the absence of the probe.

3.6.2 Challenging interpretation of the electron pressure profile differences between RDPA and Thomson and a possible hardware improvement to isolate the effect of recycling on the probe body.

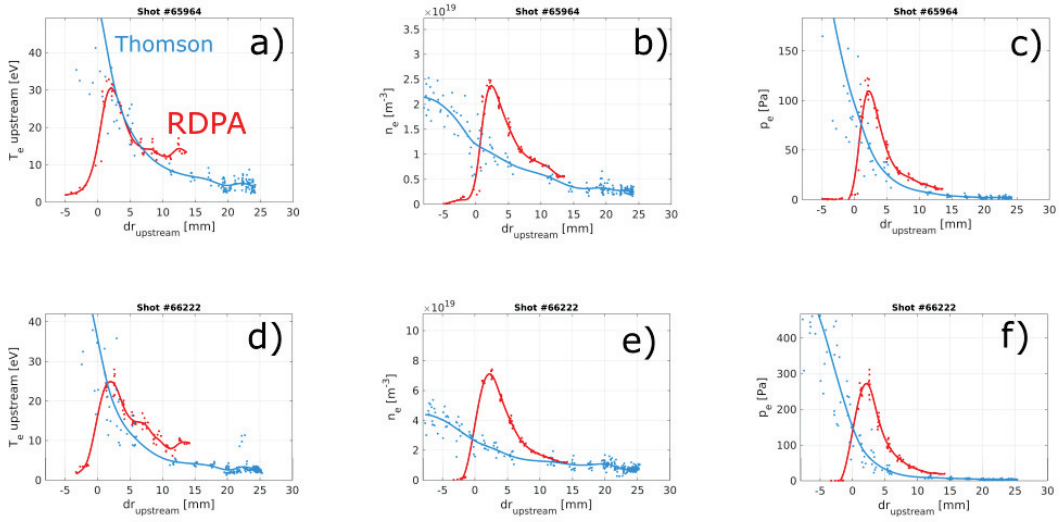

Figure 3.25: **a)** Electron temperature, **b)** density and **c)** electron pressure in the low density discharge 65964 ($I_p \approx 320\ kA$, unfavourable field direction for H-mode access, $\langle n \rangle \approx 5.0e19[m^{-3}]$). **d)** Electron temperature, **e)** density and **f)** electron pressure in the high density discharge 66222 ($I_p \approx 320\ kA$, unfavourable field direction for H-mode access, $\langle n \rangle \approx 11.0e19[m^{-3}]$).

Electron pressure profiles from RDPA agree with the upstream Thomson scattering data in most cases. However, the electron pressure measured by RDPA is higher than that measured by the Thomson scattering system at high plasma density and high plasma temperature (near the X-point region), see FIG. 3.25 **f)**. Different hypothesis are proposed to explain the mismatch:

1) If the ion temperature is larger the electron temperature near the separatrix, some of the ion pressure could be transferred to the electron pressure as the ion-electron collisionnality increases towards the divertor.

2) A shift in the magnetic equilibrium reconstruction could be partially responsible for the disagreement.

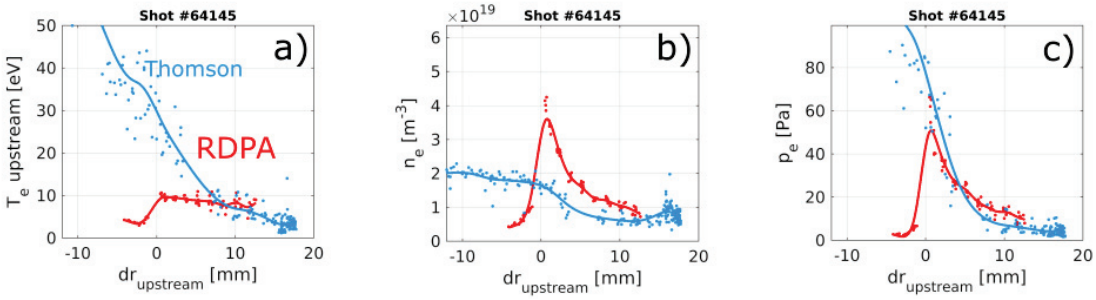

Figure 3.26: **a)** Electron temperature, **b)** density and **c)** electron pressure in the discharge 64145 ($I_p \approx -192\ kA$, favourable field direction for H-mode access, $\langle n \rangle \approx 5.0e19[m^{-3}]$).

3) A radial shift of the profile could be caused by the radial $E \times B$ drift acting within the X-point (parallel transport is inefficient in the vicinity of the X-point and therefore radial transport plays a relatively important role). Indeed, reversed field configurations (unfavourable H-mode access) show a shift of the entire pressure profile towards the LFS throughout the divertor leg. The opposite is true for the forward field discharges (favourable field direction for H-mode access), where the pressure profiles usually agree. A forward field example, with similar magnetic geometry as for the discharges in FIG. 3.25 (although at much lower plasma current) is shown in FIG. 3.26 to illustrate the better agreement.

4) A possible overestimation of the density due to the Mach probe theory from [70]. The formula used is presented in detail in SEC. 4.3.1.

5) A collected ion flux virtually enhanced by the local recycling process on the RDPA body could explain the high density measurement from RDPA. This hypothesis is motivated by the observation of a strong hydrogenic light emitted on the probe body and by the increasing mismatch between the Thomson and the RDPA profiles with increasing core density, see 3.25 **c)** and **f)**.

A careful analysis of the relative importance of these different possible processes should be carried out. Regarding the last hypothesis, which, if verified, would confirm the importance of keeping the probe body dimension as small as possible, which was one of the most challenging engineering design constraints of the diagnostic. Moreover, the inclined surface of the boron nitride shields is believed to redirect the recycled neutrals into the measured flux tube, see FIG. 3.27 **a)**. The position of the probe tips relative to the probe body could be modified in a future design of the diagnostic (e.g. moved to the front of the probe body) in order to evaluate the magnitude of this effect on the result, see FIG. 3.27 **b)**.

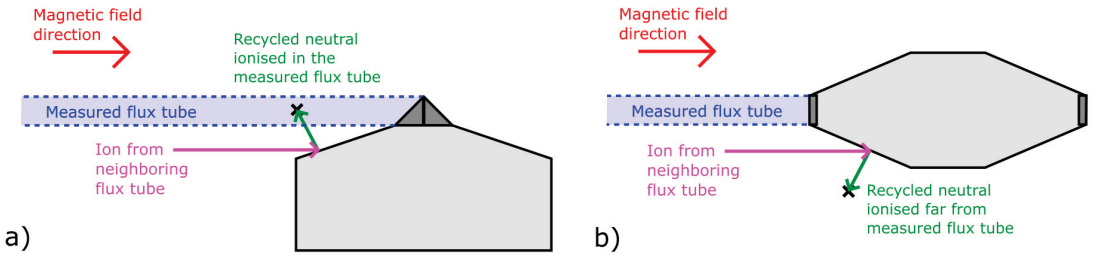

Figure 3.27: **a)** Current RDPA configuration with recycled neutrals originating from neighbouring flux tubes entering the probe collection volume and **b)** alternative design with the probe tips on the middle of the probe body in order to deflect the recycled neutrals away from the measured flux tube.

3.7 Conclusion

A novel fast probe array, dubbed RDPA, has been built at TCV [86], providing unprecedented $2D$ Langmuir probe measurements across the divertor of quantities temporally resolved at the turbulence time scales (J_{sat}, M, $\Gamma_{\parallel}$ and V_{float}) and time averaged quantities that necessitate a sweeping of the bias voltage (T_e, n_e, V_{plasma}, $v_{\parallel}$, $v_{E\times B}$). The RDPA features innovative design characteristics. In contrast to reciprocating probes accessing the divertor region of other major tokamaks, the RDPA provides $2D$ measurements in a single reciprocation, enabled by a radial array of probe tips moved vertically across an extended region of the divertor volume.

The engineering design answered the main constraints and challenges posed by the harsh tokamak environment. No sign of damage could be seen on the probe after more than 200 experiments performed, including more than ≈ 20 disruptions happening while the diagnostic was in motion. The physics results are consistent with other reference diagnostics (electron Thomson scattering and wall embedded Langmuir probes) for most plasma conditions, showing that the design is sufficiently compact to provide measurements representative of the unperturbed plasma parameters.

Further RDPA development and interpretation tasks have been identified such as improving the transmission lines, lowering the amount of recycled neutrals in the measured flux tube (to improve the interpretation of the density measurement) and developing a model for the interpretation of the asymmetries between upstream and downstream floating potentials.

4 Particle balance in the TCV divertor

The first detailed physics study with RDPA focuses on the particle balance in the divertor. The relative importance of parallel flows, ExB drifts, and upstream and divertor particle sources are explored in attached and detached conditions and with/without the recently installed TCV divertor baffles. The chapter is organised as follows. An introduction to the typical dynamics of the SOL and divertor relevant for particle balance studies in TCV is given in SEC. 4.1. A description of the experimental setup is presented in SEC. 4.2, followed by a detailed presentation of the analysis performed to deduce the most relevant quantities from the RDPA diagnostic in SEC. 4.3. The main experimental results are presented in SEC. 4.4. Finally, a summary of this chapter is presented in SEC. 4.5.

4.1 SOL and divertor dynamics expected in TCV

As presented in SEC. 1.4.2, heat is continuously expelled from the core plasma into the SOL, through cross-field transport. Most of the cross-field transport from the core into the tokamak SOL has been shown to be caused by turbulence near the outer mid plane in the region of 'unfavourable' magnetic field curvature [112] [113]. Indeed, the outer mid-plane is a destabilizing region for curvature driven instabilities. Also, in this region, non-linear turbulent structures can easily be shown to cause a self-induced electric field with an outward directed ExB drift [114].

Particle balance in a tokamak can differ substantially from that of heat: if the core is perfectly screened from incoming neutral particles, the ionisation process mostly occurs in the SOL and there is no cross field particle flux passing through the separatrix in steady state conditions. In this particular case, radial profiles of plasma density tend to be flat [38]. However, in realistic cases, some ionisation occurs in the core, for various reasons such as a long ionisation mean free path (seen in TCV), pellet injection (planned in ITER) and neutral beam heating. Besides fluctuation induced cross-field fluxes, parallel fluxes, $E \times B$ drift fluxes, and $\vec{B} \times \nabla B$ drift fluxes are the dominant particle transport channels [115]. The direction of these fluxes are shown for a reversed field discharge (upward ion $\vec{B} \times \nabla B$ drift from the X-point to the core), see FIG. 4.1

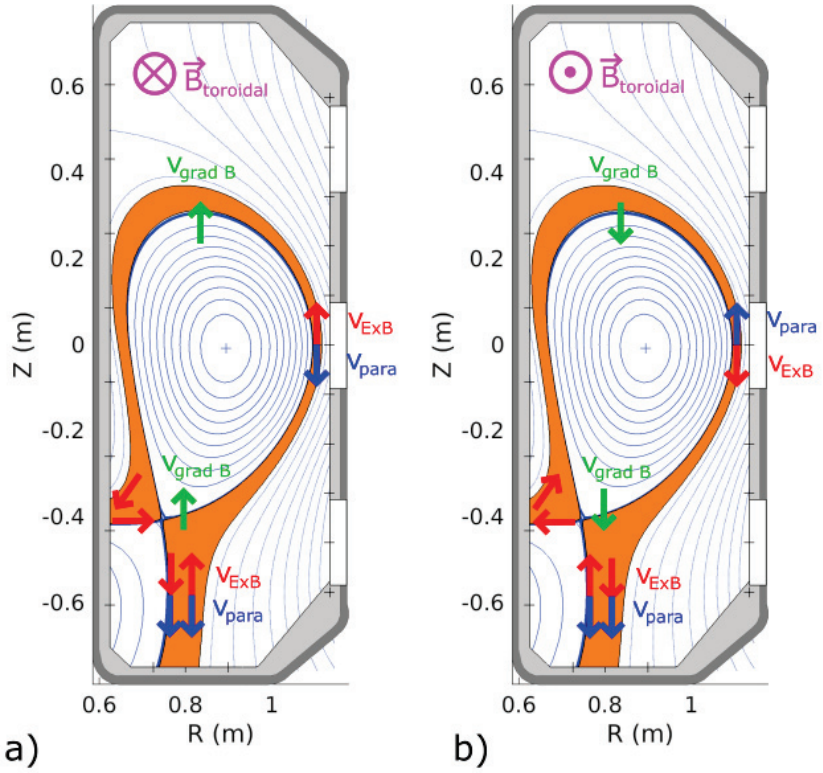

Figure 4.1: The most important parallel and poloidal flows illustrated for a **a)** reversed field discharges and **b)** forward field discharge in TCV.

a), and for a forward field discharge (downward ion $\vec{B} \times \nabla B$ drift from the core to the X-point), see FIG. 4.1 **b)**.

The vertical $\vec{B} \times \nabla B$ drifts are responsible for cross field transport mostly at the top and at the bottom of the plasma. As they are directed in opposite directions for ions and electrons, they are responsible for parallel return electrical currents in the upstream SOL. These return currents are called Pfirsch-Schluter currents in the literature [116]. Ions being much more massive than electrons, experimentalists usually consider that the plasma velocity is equivalent to the ion current velocity and, therefore, $\vec{B} \times \nabla B$ drifts are also responsible for Pfirsch-Schluter parallel 'flows'. $E \times B$ are not responsible for any electrical current because they do not generate any charge separation. However, they can be responsible for strong parallel return flows [116]. $\vec{B} \times \nabla B$ drifts are much weaker than $E \times B$ drifts, but their contribution is integrated over the entire separatrix because they are partially directed across flux surfaces, unlike the steady-state $E \times B$ drifts, which, near the LCFS, are mostly directed tangential to the flux surfaces (poloidal flow) and create 'local' parallel return flows within a given flux surface. It can be experimentally difficult to figure out the different contributions to the overall parallel current in the SOL [116]. At the outer mid plane, the ion $\vec{B} \times \nabla B$ drift is aligned with the flux surface and its magnitude is negligible in comparison with the $E \times B$ velocity for the typical TCV OMP

conditions ($T_e = T_i = 30\ eV$, $B = 1.4\ T$, $R_0 = 0.9\ m$, $\lambda_{T_e} \approx 0.03\ m$, $E \approx 3T_e/\lambda_{T_e} = 3000\ V\,m^{-1}$):

$$v_{\nabla B,ion} = \frac{\frac{1}{2} m_i \langle v_\perp \rangle^2}{qB} \frac{|\vec{B} \times \nabla B|}{B^2} \approx 18\ ms^{-1} \ll v_{E\times B} = \frac{|\vec{E} \times \vec{B}|}{B^2} \approx 2150\ ms^{-1}. \tag{4.1}$$

Therefore, the $\vec{B} \times \nabla B$ drift is not a key player in the nearly vertical outer divertor leg, later studied in this chapter. This simplified considerations are supported by the results of SOL/divertor transport code studies including drift terms, which highlighted the dominant role of $E \times B$ drifts in the divertor [115] [117].

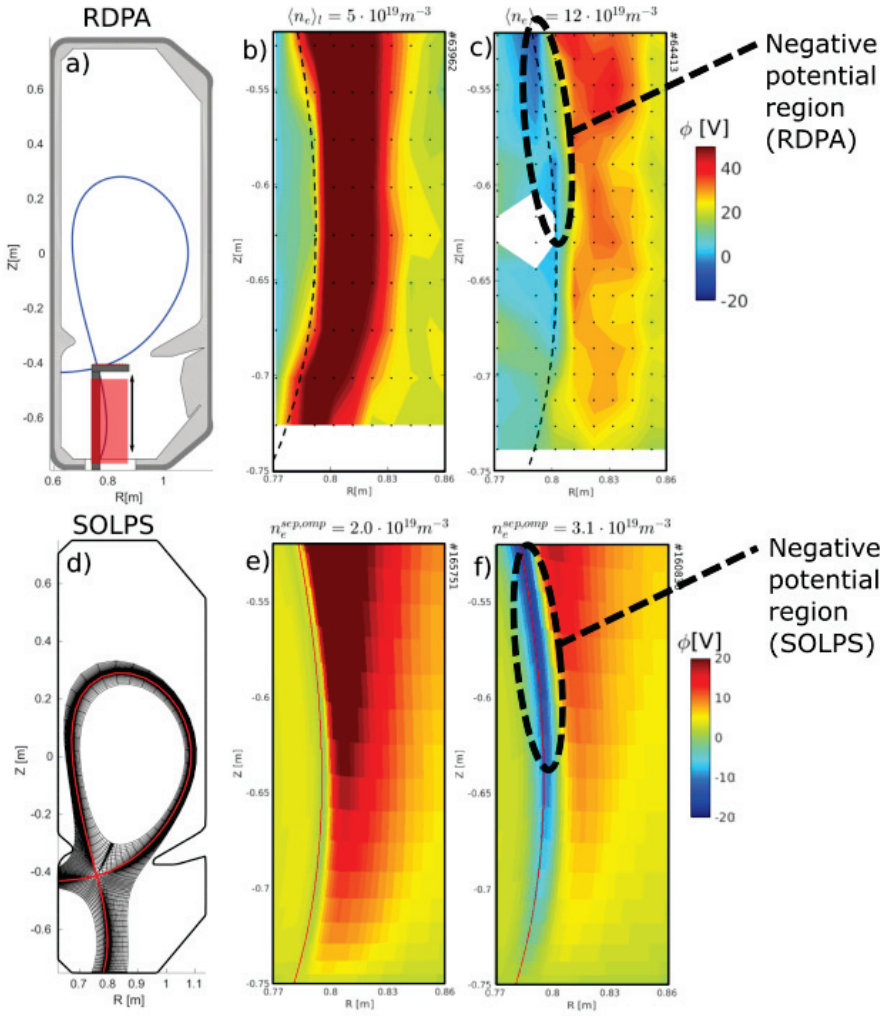

Figure 4.2: **a)** Plasma shape and RDPA diagnostic with **d)** corresponding SOLPS grid. Plasma potential inferred from RDPA downstream probes in **b)** low and **c)** high density TCV discharges. Black dots indicate the measurement locations. Corresponding **e)** low and **f)** high density SOLPS-ITER simulations [118].

We note here, however, that in some conditions, the $\vec{B} \times \nabla B$ can be indirectly responsible for enhanced divertor $E \times B$ fluxes. In reversed field discharges and at high collisionnality, SOLPS simulation have shown that a negative plasma potential can develop near the X-point [119]

which was later experimentally confirmed with RDPA measurements [118], see FIG. 4.2. A careful study enabled to understand the role of the asymmetry between the ion and electron ∇B drifts in the X-point region which leads to a parallel electrical return current to the target in the private flux region. At very low electron temperatures, a parallel electrical field builds up in order to overcome the electrical resistivity of the plasma. The negative potential then strengthens the radial electrical field and, therefore, increases the poloidal $E \times B$ flux. It should be noted that this specific feature is only present at high plasma collisionnality, where $E \times B$ fluxes are generally weaker than for attached discharges, because of the lower plasma potential values and wider SOL characteristic widths.

The role of divertor cross field transport channels, such as turbulence and $E \times B$ due to poloidal E field, are beyond the scope of this chapter, although RDPA measurements could be used to improve understanding on the subject. The content of the following sections is rather focused on the description of parallel and poloidal $E \times B$ particles fluxes.

4.2 Experimental setup

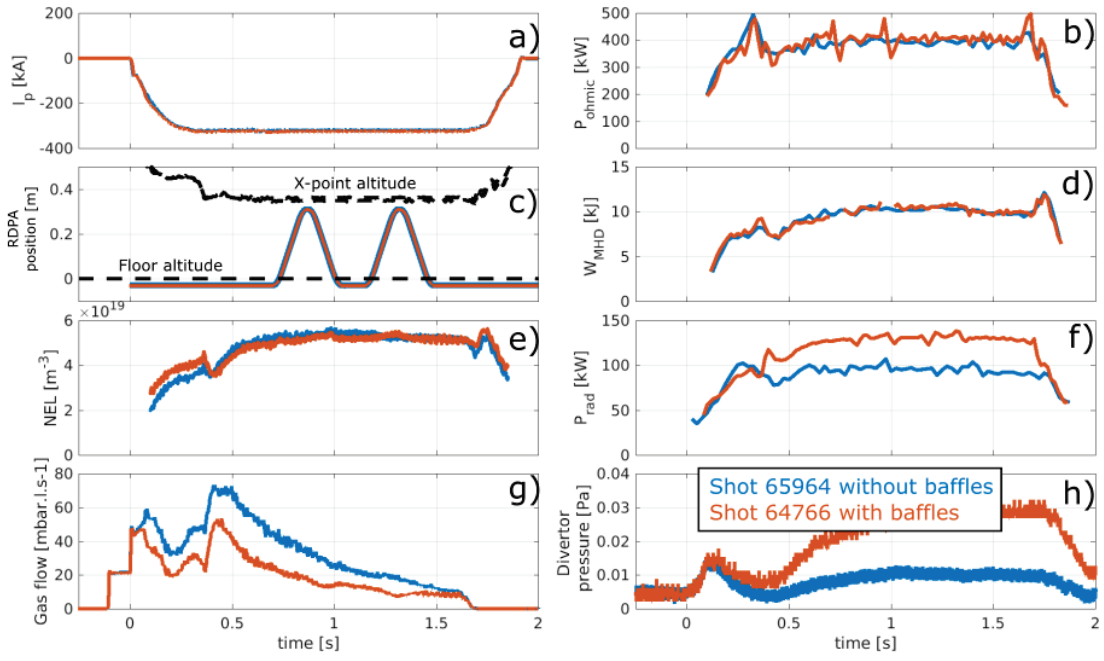

Figure 4.3: Time traces of relevant plasma properties from the low density reference #65964 without baffles and the low density reference #64766 with baffles: **a)** plasma current, **b)** ohmic power (no external heating source has been used in this study), **c)** vertical position of the RDPA probe, **d)** stored energy computed from magnetic measurements, **e)** line averaged density from interferometry measurements, **f)** total radiated power from bolometry measurements, **g)** deuterium gas flow and **h)** divertor neutral pressure from baratron measurements.

The experiments to explore the TCV divertor particle balance have been performed in Lower Single Null (LSN) Ohmic L-mode plasmas with constant magnetic field $B_t \approx 1.4\ T$ and constant

plasma current $I_p \approx 320\ kA$. The toroidal field is said to be 'reversed' which correspond to an upward ion $\vec{B} \times \vec{\nabla} B$ drift and unfavourable access to H-mode. The reversed field direction has been chosen to avoid H-mode transitions while operating at maximum toroidal magnetic field, which translates into a more stable plasma (operation with less magneto-hydrodynamics instabilities). $I_p = 320\ kA$ is a compromise between respecting the experimental disruptive limit in TCV $q_{95} < 2.15$ and having magnetic field lines sufficiently pitched to limit the total fraction of field lines being intercepted by the RDPA probe body (< 15%) in the divertor outer leg. High plasma current also enables to attain a higher line averaged density by delaying the density disruptive limit. The line averaged core density has been varied from $5 \cdot 10^{19}\ m^{-3}$ up to $11 \cdot 10^{19}\ m^{-3}$ in order to access both attached and detached divertor conditions. Edge physics experiment are often performed with density ramps in TCV [36] in order to study the plasma evolution from attached to detached within a single experiment. Since RDPA plunges last typically $\approx 0.35\ s$ (time limited by the motor force), performing the measurements during a density ramp would lead to inaccurate profiles. Instead, multiple shots have been performed with constant core densities. RDPA was found to have a negligible effect on the relevant main plasma properties such as radiated power, stored energy, line averaged density, Ohmic power, gas fuelling and divertor pressure. Indeed, these quantities are constant during the reciprocation time, as shown in FIG. 4.3. RDPA produces a characteristics shadow in the downstream region where the plasma density is lower than in the surrounding plasma and, therefore, data from the floor LPs within the shadow needs to be discarded.

The integrated ion flux density at the outer target, the $CIII$ emission front position along the outer leg [36] and the divertor neutral pressure, given as a function of the line averaged density, are found to be very similar for the density ramp experiments and the constant density experiments, as shown in FIG. 4.4. This indicates that the divertor conditions, including neutral dynamics and impurity levels, can be considered to be close to an equilibrium at any given time for the density ramp experiments in TCV.

The heat and particle exhaust characteristics of the TCV tokamak have been modified with a recent divertor upgrade [48] where an in-vessel structure of solid graphite baffles forms a divertor chamber of increased closure, in order to decouple divertor and main chamber regions. Experiments have been performed with an open divertor, see FIG. 4.4 **a)**, **b)**, **c)** and **d)**, as well as in the presence of the baffles, see FIG. 4.4 **e)**, **f)**, **g)** and **h)**. The integrated ion flux does not roll over in the absence of the baffles in these shots, see FIG. 4.4 **b)**, unlike the integrated ion flux in the baffled shots, which rolls over once $\langle n_e \rangle > 10 \cdot 10^{19} [m^{-3}]$, see FIG. 4.4 **f)**. Likewise, the effect of the baffles can be clearly seen with an earlier movement of the $CIII$ front towards the X-point and a substantially higher neutral divertor pressure (up to a factor 5 higher) for the same core conditions. These effects of the baffles are similar but even stronger than other L-mode results obtained at $I_p = 250\ kA$ [41] [120].

The gas flow required for fuelling, shown in the point **g)** in FIG. 4.3, was lower with the baffles installed for the low core density references $\langle n \rangle \approx 5.5e19 [m^{-3}]$. This counter-intuitive observation is, however, not always observed: in other experiments, the gas flow required was larger

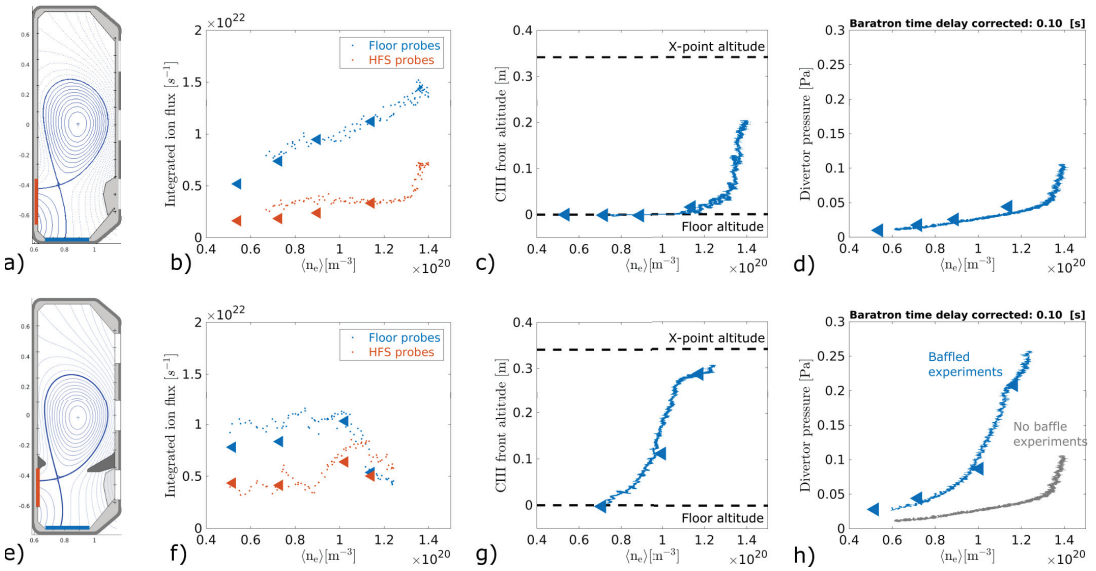

Figure 4.4: **a)** and **e)** Magnetic equilibrium reconstruction and relevant Langmuir probe coverage highlighted on the walls, **b)** and **f)** Integrated inner and outer target ion fluxes deduced from J_{sat} radial profiles as a function of $\langle n_e \rangle$ obtained from FIR measurements, **c)** and **g)** CIII front altitude obtained from the multi spectral imaging MANTIS system and **d)** and **h)** neutral divertor pressure obtained from the baratron gauge. Shots without baffle are shown in **a)**, **b)**, **c)** and **d)**: constant density experiments #65964, #66210, #66220 and #66222 represented with triangles and the density ramp #66208 represented with scattered points. Shots with baffles are shown in **e)**, **f)**, **g)** and **h)**: constant density experiments #64766, #63963, #64965 and #64962 represented with triangles and the density ramp #64900 with scattered points. CIII data for the shot #64766 could not be acquired.

with the baffles installed. It can be explained by the fact that the dominant plasma fuelling source comes from recycled neutrals, such that small changes in the recycling coefficient, a property of the wall surface condition, can indeed substantially influence the required gas puffing rate.

4.3 Parallel and ExB flow calculations with RDPA

This section discusses how the parallel ion Mach number, the electron density, the ion flux along the magnetic field and the $E \times B$ fluxes are deduced from the time averaged quantities obtained with RPDA. To illustrate these steps, example results from RDPA in an attached L-mode plasma without baffles, at a line-averaged density of $\langle n \rangle \approx 6.75 \cdot 10^{19} m^{-3}$, and with the same geometry and experimental parameters as for the discharges in Fig. 4.4 (unfavourable ion $\vec{B} \times \vec{\nabla} B$ drift, $I_p \approx 320\ kA$) are presented in FIGs. 4.6 to 4.9. These figures are divided into three regions listed here by their order of appearance from top to bottom: **1)** 1D profile near the top of the plunge (region within the dashed red rectangle near the X-point), **2)** 2D contour plot from RDPA in the middle plot and **2)** 1D profile near the bottom of the plunge (region

within the dashed red rectangle region near the target at $Z = -0.75\ m$).

4.3.1 Parallel flow and ion flux measurements

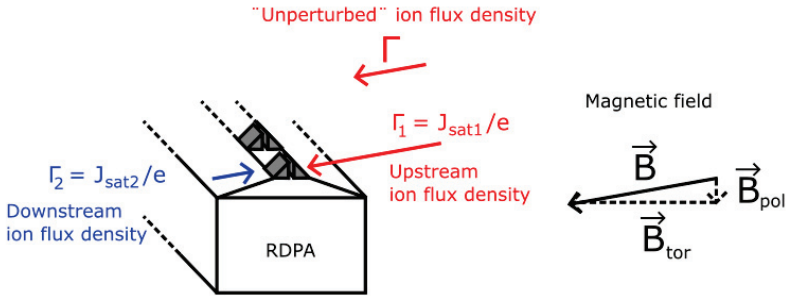

Figure 4.5: Mach probes of the diagnostic RDPA and their position relative to the magnetic field: upstream or downstream.

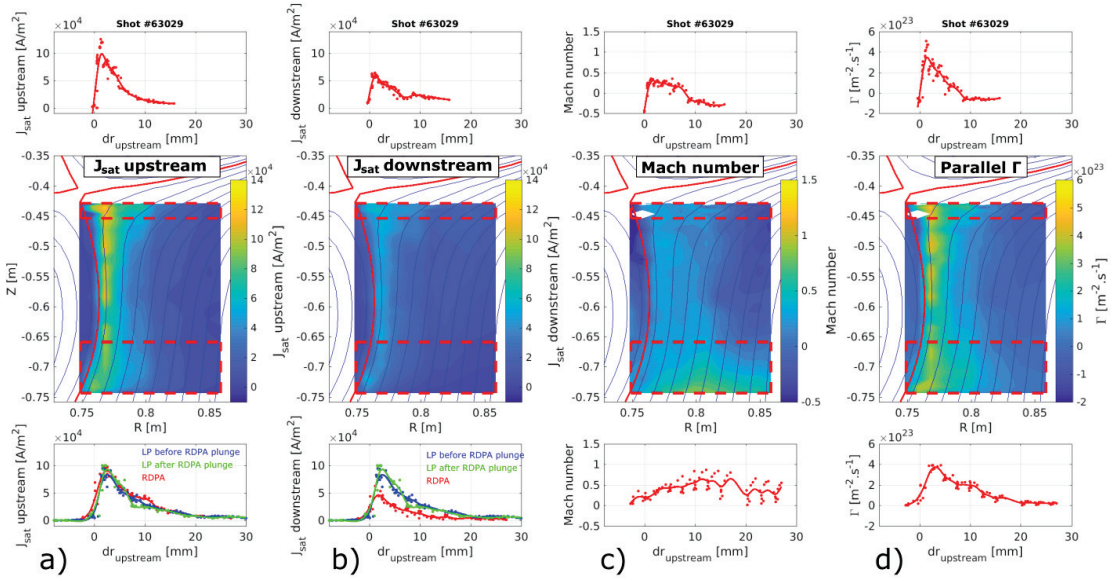

Figure 4.6: **a)** Upstream ion saturation current density, **b)** Downstream ion saturation current density, **c)** Mach number and **d)** Parallel particle flux density for a non-baffled, LSN L-mode plasma, $I_p \approx 320\ kA$, $\langle n \rangle \approx 6.75 \cdot 10^{19} m^{-3}$.

The parallel Mach number is deduced from the ratio of downstream and upstream J_{sat} [70]:

$$M = \ln\left(\frac{J_{sat1}}{J_{sat2}}\right)/2.2. \tag{4.2}$$

Here, J_{sat1} and J_{sat2} can be obtained from swept probes or with a higher time resolution, when the probes are operated in ion-saturation current mode.

The electron density n_e, in the presence of possible flows, is calculated with a viscous plasma

model based on diffusive perpendicular transport [70]:

$$n_e = \frac{J_{sat1}/e}{c_s \exp(-1+1.1M)}, \tag{4.3}$$

where c_s is the plasma sound speed, usually calculated as $\sqrt{(T_e+T_i)/m_i}$ [51]. Unlike the sign convention given in [70], M is here defined as positive for a particle flux directed into the upstream surface and out of the downstream surface. A positive Mach number therefore corresponds to a plasma flow directed towards the target. EQ. (4.3) shows reasonable agreement with expressions used for density measurements with LPs in the bulk plasma and for $M = 0$, as well as for measurements near a wall with $M = 1$. Indeed, for $M = 0$, EQ. (4.3) becomes:

$$n_e = \frac{J_{sat1}/e}{c_s exp(-1)} \approx \frac{2.7 J_{sat1}/e}{c_s}, \tag{4.4}$$

which agrees within 35% with the usual expression[38]:

$$n_e = \frac{2J_{sat1}/e}{c_s}. \tag{4.5}$$

In the case where $M = 1$, the density from EQ. (4.3) becomes:

$$n_e = \frac{J_{sat1}/e}{c_s \exp(0.1)} \approx 0.9 \frac{J_{sat1}/e}{c_s}, \tag{4.6}$$

which is close to the commonly accepted formula for the sheath edge density:

$$n_{se} = \frac{J_{sat1}/e}{c_s}. \tag{4.7}$$

n_e is meant here to represent the plasma density in the unperturbed plasma (in the absence of the probe) and in particular differs from the sheath edge densities n_{se1} and n_{se2} on the upstream and downstream probe tips. A different model, derived in the case of a drift based perpendicular transport, gives a similar formula for the density [121] and could have been chosen as another suitable option. The contributions from perpendicular drifts (represented by the Mach number $M_\perp$ perpendicular to the magnetic field) to the calculated plasma density have been explicitly calculated for this drift based model [121]:

$$n_e = \frac{J_{sat1}/e}{c_s \exp(-1-(M-M_\perp cot(\theta)))}, \tag{4.8}$$

where θ is the angle (in the plane of field and drift velocity) of the object surface to the magnetic field and M is here defined with the sign convention given in [70]. As stated in [121]: *"If a facet lies in a concave region of the object [...], then it does not possess its own plasma region. Instead, the solution(s) of the earlier region(s) applies right up to the respective fractions of that facet."* and, therefore, the relevant angle θ for the RDPA probe tip is not the angle of the probe tip surface because of the concavity of the RDPA cross-sectional geometry in the case of a downward $E \times B$ velocity. Instead, the angle between the boron nitride thermal shield surface

and the magnetic field direction, $\theta \approx 15°$, is relevant for EQ. (4.8). The term $M_\perp cot(\theta)$ brings a noticeable contribution to the density calculation in the case of large $E \times B$ velocities, such as for the experimental results shown in FIG. 4.7 and 4.8 ($T_e \approx 27\ eV$, $v_{E\times B} \approx 3000\ ms^{-1}$):

$$M_\perp cot(\theta) = \frac{v_{E\times B}}{c_s} cot(\theta) \leq 3.7 \cdot 3000\ ms^{-1}/51000\ ms^{-1} \approx 0.22. \tag{4.9}$$

This density correction due to the perpendicular velocity has not been calculated in the present work and therefore could possibly lead to an error of up to 20% on the density calculation in the worst case (region of strong downward $E \times B$ velocity).

Finally, the parallel particle flux density is calculated from the relation between the sound speed and the Mach number:

$$\Gamma = v_\parallel \cdot n_e = M \cdot c_s \cdot n_e = \frac{M J_{sat1}/e}{\exp(-1 + 1.1M)}. \tag{4.10}$$

It is interesting to notice that the flow measurement is independent of the temperature measurement. This is an advantage in the case of detached plasmas, where the electron temperature can be overestimated for Langmuir probes measurements [51]. As shown in FIG. 4.6 **a)**, the upstream ion saturation current collected by RDPA is usually similar to the ion saturation current collected by wall probes. On the other hand, the downstream current is usually a factor 2 lower, see FIG. 4.6 **b)**, resulting in a moderate Mach number, $M \approx ln(2)2)/2.2 \approx 0.3$ shown in FIG. 4.6 **c)**.

4.3.2 Measurement of ExB particle fluxes

$E \times B$ particle fluxes are calculated as the product between the local plasma density and the $E \times B$ drift velocity:

$$\vec{\Gamma}_{E\times B} = n_e \cdot \vec{v_{E\times B}} = \frac{J_{sat1}/e}{c_s \exp(-1 + 1.1M)} \frac{\vec{E} \times \vec{B}}{B^2} \tag{4.11}$$

The drift velocity is calculated from the plasma potential measurement obtained from sheath theory:

$$V_{pl} = (V_{fl,downstream} + V_{fl,upstream})/2 + 3T_{e,upstream}, \tag{4.12}$$

where $T_{e,upstream}$ is expressed in $[eV]$ and the constant 3 corresponds to a deuterium plasma where $T_e \approx T_i$ and where the coefficient of secondary electron emission is zero [38]. Example measurements of these quantities are presented in FIG. 4.7 and 4.8. In the absence of any valid theory explaining occasionally observed discrepancies between upstream and downstream floating potential measurements, apparent in FIG. 4.7 **c)** and **d)**, the average between the upstream and downstream values is taken. This default choice is motivated by a quantitative agreement with the V_{pl} target profiles, see FIG. 4.8 **a)**, although it does not address the discrepancies seen near the top of the plunge where comparison with wall LPs is not meaningful.

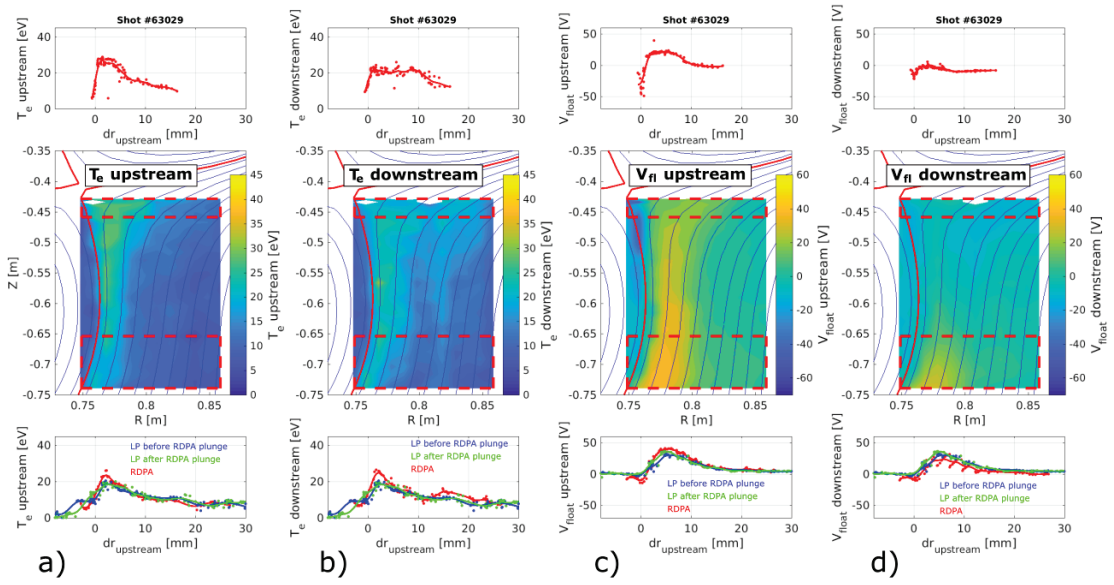

Figure 4.7: **a)** Upstream electron temperature, **b)** Downstream electron temperature, **c)** Upstream floating potential and **d)** Downstream floating potential. Data from the same discharge as in FIG. 4.6.

In the case of electron temperatures, the difference between upstream and downstream values is usually less pronounced than for the V_{fl} profiles, see points **a)** and **b)** of FIG. 4.7. The upstream electron temperature value has been chosen for the calculations but the downstream value would be suitable as well.

The electric field in the toroidal direction can be neglected because the loop voltage in steady state conditions is negligible. For the case of a predominantly toroidal field (B_z, $B_r \ll B_\phi$), the $E \times B$ drift velocity can then be written as:

$$\vec{v}_{E\times B} \approx \frac{-E_z B_\phi}{B^2}\vec{e}_r + \frac{E_r B_\phi}{B^2}\vec{e}_z. \tag{4.13}$$

Here, the second term dominates in the present case with a near-vertical divertor leg. In FIG. 4.9 **b)**, an example of the 2D measurements of the projection of the $E \times B$ drift along the vertical direction is given. In FIG. 4.8 **c)**, the vertical $E \times B$ velocity has been defined to be positive when directed towards the target and is therefore projected along the vector $-\vec{e}_z$. This graphical choice has been made in order to have the same sign convention as the parallel ion flux in FIG. 4.6 **d)** (positive towards the target).

A clear result arising from these measurements is that $E \times B$ flows, although being much weaker than parallel flows in the divertor, bring a substantial contribution to the total poloidal ion flux due to the shallow pitch angle of the field lines (field lines being almost purely oriented in the toroidal direction). This poloidal contribution can be larger than the parallel flows in the case of attached discharges as seen in FIG. 4.9, where the high electron temperatures lead to steep plasma potential profiles. A similar observation of strong $E \times B$ flows has been already

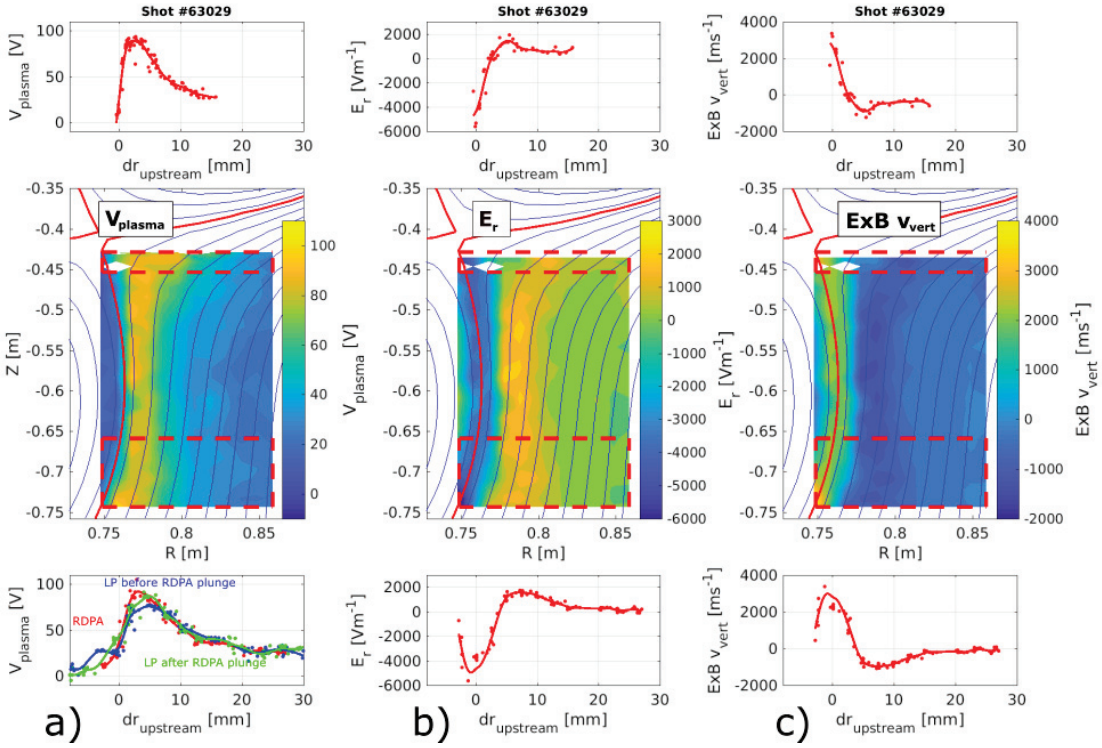

Figure 4.8: **a)** Plasma potential, **b)** Radial electrical field and **c)** Vertical ExB velocity. Data from the same discharge as in FIG. 4.6 to 4.7.

observed experimentally in $DIII-D$ [91][92][122][111].

Wall embedded LPs measure the $E \times B$ flux which is, together with the parallel flux, included in the J_{sat} measurement according to the Bohm-Chodura criterion, which in the marginal form is (for $B_{tor} \approx B$) [38] [123]:

$$v_{\parallel} + \frac{v_{E\times B}}{sin\theta} = c_s, \tag{4.14}$$

where θ is the grazing angle between the magnetic field and the surface. A fairly good agreement between the J_{sat} measurement from LPs and the total flux from RDPA is observed. However, in low density cases, such as the example shown in FIG. 4.9, the $E \times B$ flux measurement from RDPA seems to be overestimated when compared to the J_{sat} measurement from the domed probes on the floor (not shown). A possible hypothesis could explain the mismatch: once the ion temperature is sufficiently high, the ion Larmor radius becomes comparable in size with the probe tips. In this case, the angle θ sharply increases at the transition between the floor and the domed probe surface, and the parallel velocity must rapidly change to satisfy EQ. 4.14. Collisions between ions in the pre-sheath could be working against this sharp transition of the parallel velocity and therefore explain the 'missing' flux on floor LPs.

Another experimental finding which illustrates the dominant role of $E \times B$ flows is the observation of upward parallel flux in the downward $E \times B$ region, see FIG. 4.10. In this experiment, the electron temperature is higher than in the example previously discussed due to a lower

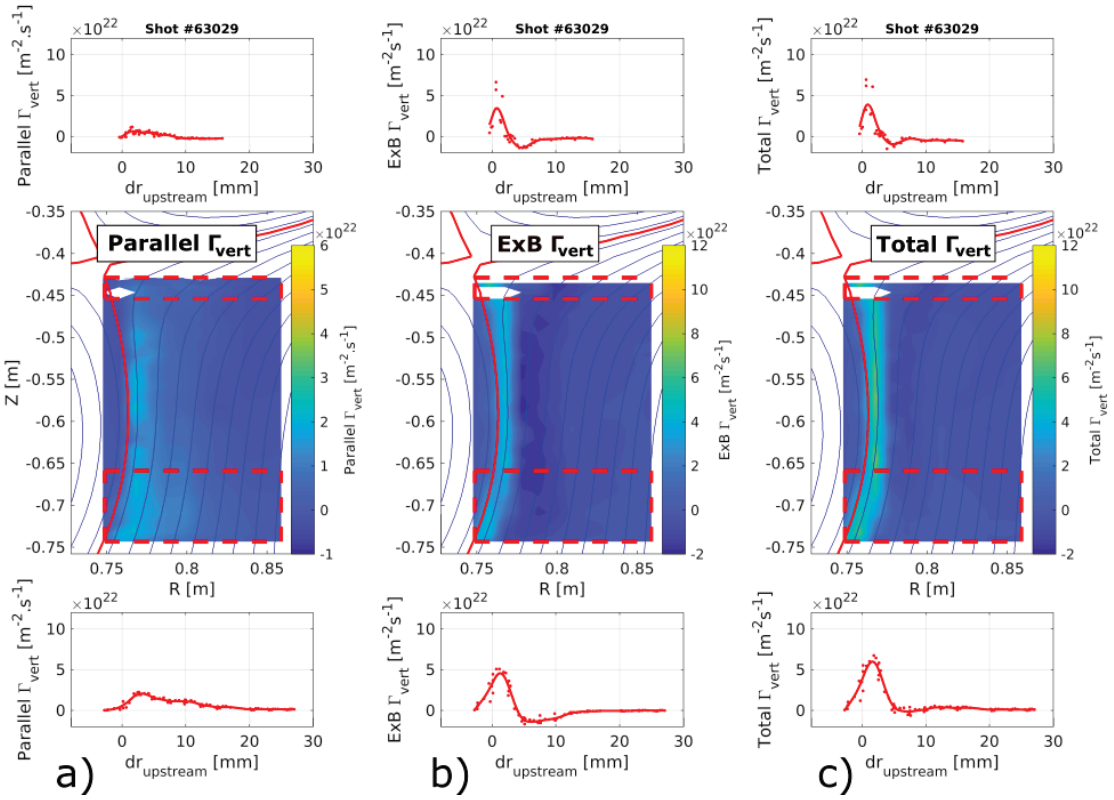

Figure 4.9: **a)** Vertical particle flux density from the parallel Mach measurement, **b)** Vertical ExB particle flux density and **c)** Total vertical particle flux density. Data from the same discharge as in FIG. 4.6 to 4.8.

core density. The strong $E \times B$ flux 'forces' the parallel flux to be reversed (directed to the inner target). The appellation of flow 'reversal' is not even well suited to the situation because the parallel flow seems to be directed upward even in the region near the target, i.e. the stagnation point of the parallel velocity is expected to be close to the pre-sheath region. In the region of upward $E \times B$ flow, a supersonic flow would instead be expected near the target but has so far not been observed experimentally. The difficulty to satisfy EQ. 4.14 also applies for the proud probes of the RDPA Mach measurement (rapid change in the incidence angle) and could possibly explain some of the underestimation of the Mach number in this situation. Reversal of the flows should be also studied in the future for attached forward field discharges to see if the same trend is still observed.

4.4 Divertor particle balance

4.4.1 The influence of core density on the divertor particle balance

In the following, we perform a $1D$ particle balance along the divertor leg, obtained by integrating the vertical ion flux densities due to the parallel and $E \times B$ flows, determinant from the

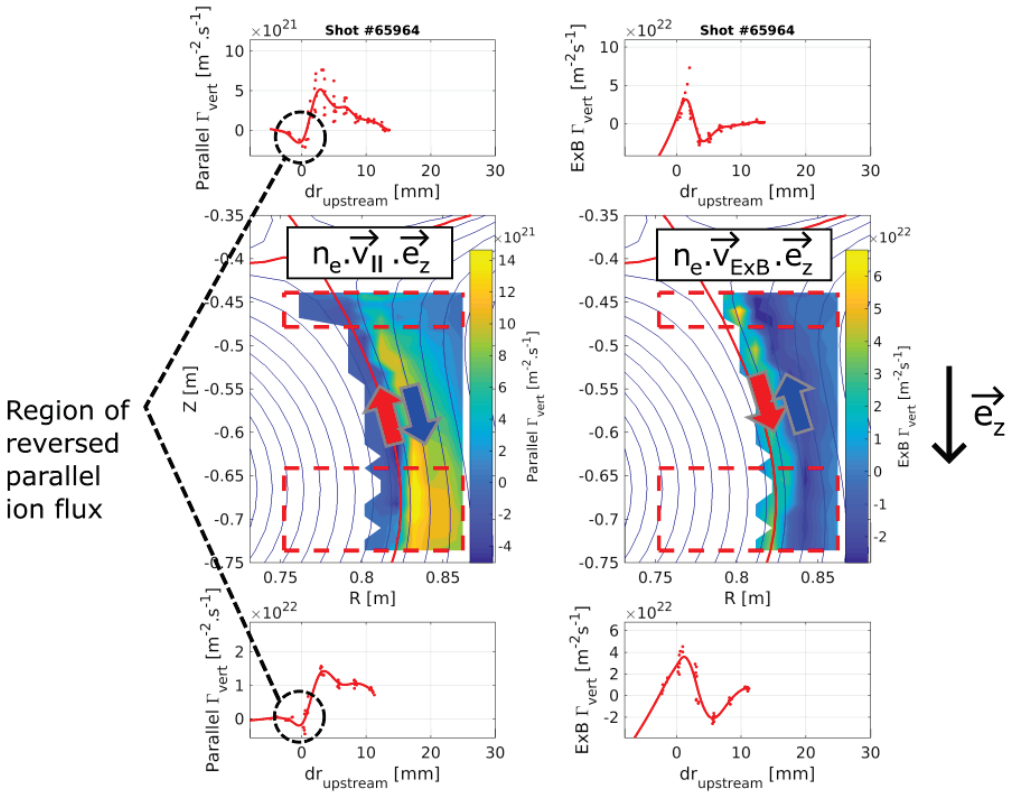

Figure 4.10: **a)** Vertical particle flux density from the parallel Mach number measurement, **b)** Vertical ExB particle flux density for the shot 65964, a non-baffled, LSN L-mode plasma, $I_p \approx 320\ kA$, $\langle n \rangle \approx 5.25 \cdot 10^{19}\ m^{-3}$.

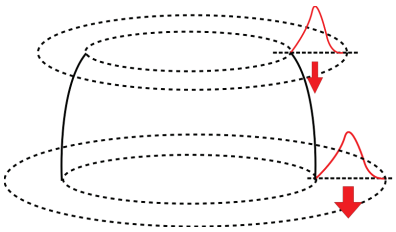

Figure 4.11: The total ion flux to the outer target is obtained from integrating the vertical flux density, represented by the red profiles, both radially and toroidally.

RDPA. The integration is performed both along the radial and the toroidal direction. Thus, this integration allows removing effects due to radial cross-field transport. The radial poloidal integration allows to neglect radial cross field transport. Indeed, radial transport leads to a wider spread in the profile but it does not change the overall poloidal ion flux along the leg. Only source and sink terms such as volumetric ionisation and recombination can change the overall ion flux. An illustration of the integration performed with the relevant geometry is shown in FIG. 4.11.

Results for the three non baffled experiments with different core density are shown in the FIG. 4.12. Reproducibility of the results between different RDPA plunges is usually excellent, as

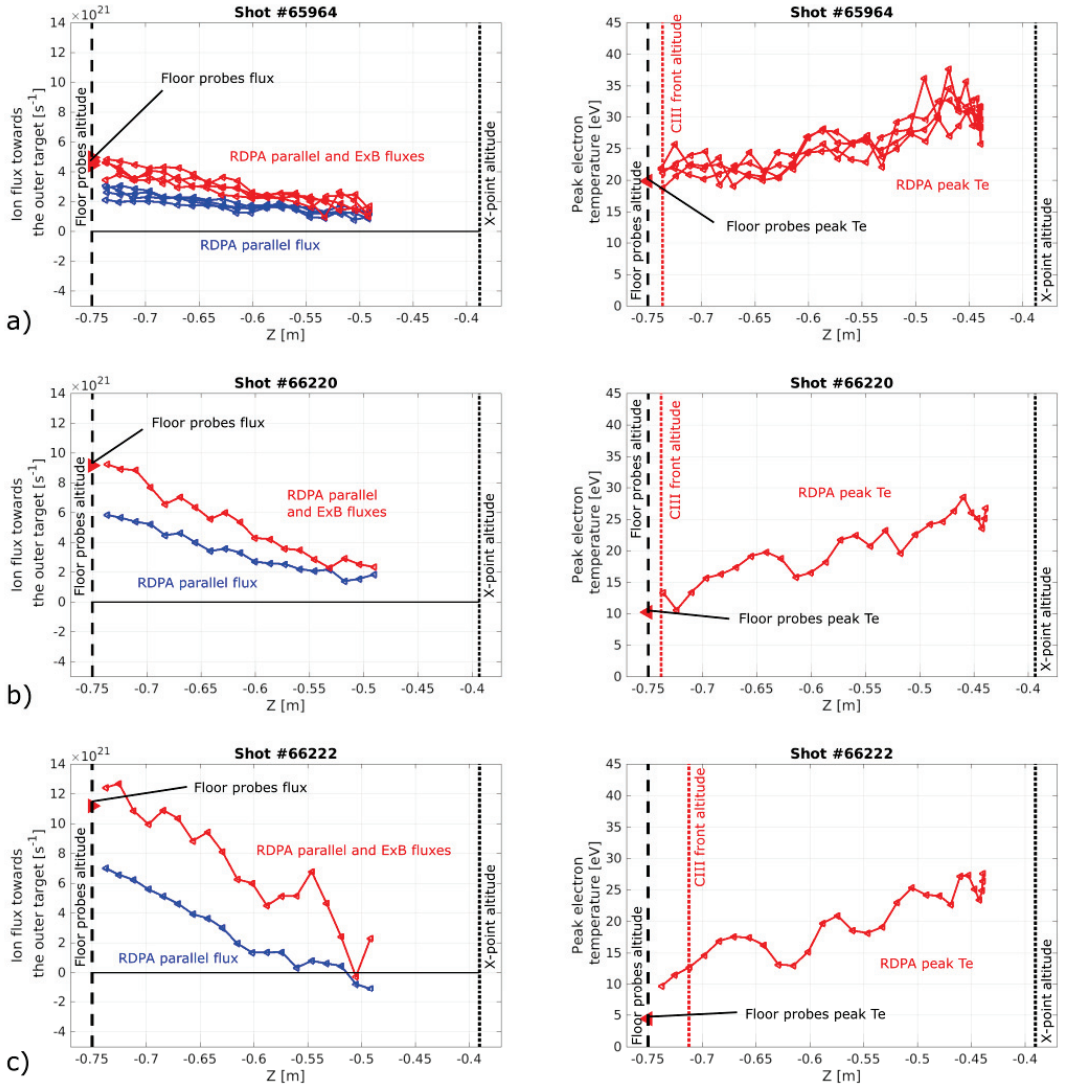

Figure 4.12: Profiles along the outer leg of the total vertical ion flux (left column) and the peak electron temperature (right column) for different discharges. **a)** Low core density references #65964 $\langle n_e \rangle \approx 5.5e19[m^{-3}]$, **b)** High core density reference #66220 $\langle n_e \rangle \approx 8.5e19[m^{-3}]$ and **c)** Highest core density reference #66222 $\langle n_e \rangle \approx 11e19[m^{-3}]$. The blue and red lines on the left plots correspond respectively to the integrated parallel flux and to the integrated total flux (parallel and $E \times B$) along the vertical divertor leg.

shown for the shot 65964, where 4 curves from two up-down plunges have been plotted in the same graph, see FIG. 4.12 **a)**.

The low density reference, see FIG. 4.12 **a)**, has a non negligible ion flux coming from the upstream SOL (above the RDPA coverage), $\iint \Gamma_{upstream} ds / \iint \Gamma_{target} ds \approx 20\%$. The proportion of ions coming from the upstream plasma is higher than for the baffled case, as shown later in SEC. 4.4.3. However, since the RDPA is not reaching all the way up to the X-point, it is possible

that the actual contribution from the upstream SOL is close to zero or even negative (net flow of particle towards the inner target via the common and/or the private flux region) in the plasma region above the RDPA coverage. The plasma shows a high peak electron temperature $T_{e,max} \approx 30\ eV$ and little electron temperature gradient, as expected from efficient electron heat conductivity in this high electron temperature range.

In all these shots, the electron temperature ($T_{e,max} > 15\ eV$) is high enough to ionise neutral particles along the entire divertor leg. The intermediate core density and the high density references, see FIG. 4.12 **b)** and **c)**, have a larger amount of divertor ionisation, attested by the steeper increase in the total ion flux towards the floor and by the higher flux measured by the floor probes. The parallel ion flux even slightly reverses near the top of the plunge for the highest density and is close to zero when including the $E \times B$ drift contribution. This observation would agree with the 'closed box' divertor approximation [124] [46], where most of the ionisation is assumed to happen in the divertor. More studies should be performed in this regard in TCV, taking advantage of the upstream fast scanning probe measurements to determine the source of particles originating from the core and the upstream SOL.

4.4.2 The influence of core density on the divertor particle balance in the presence of baffles

RDPA results (integrated ion flux and peak electron temperature) for three different baffled experiments with increasing core density are shown in FIG. 4.13. The fraction of the target ion flux coming from the upstream SOL (above the RDPA coverage) is $\Gamma_{upstream}/\Gamma_{target} \approx 15\%$ for the low density reference **a)**. The plasma shows a high peak electron temperature at the top of the plunge and a substantial temperature gradient from $T_{e,max} \approx 25\ eV$ down to $T_{e,max} \approx 12\ eV$.

The intermediate core density reference, see FIG. 4.13 **b)**, has the largest amount of divertor ionisation and reveals no ion flux coming from the upstream SOL. The parallel flux is directed upwards (negative parallel flux) and the total flux (including the $E \times B$ drift) is close to zero at the top of the RDPA scan. Note that the parallel flux is dominantly reversed in the region of downward $E \times B$ velocity, which is close to the separatrix in these discharges. The electron temperature is not high enough to ionise neutrals near the target. $T_e \approx 7\ eV$ according to the wall-embedded Langmuir probe measurement, however, $T_e < 5\ eV$ is expected because of the overestimation of T_e at high collisionnality [51]. The consequence of the absence of any ionisation near the target can be seen in the total ion flux curve, which remains flat due to the absence of any divergence term in this region.

The high core density reference, see FIG. 4.13 **c)**, has a negligible amount of divertor ionisation and the entire ion flux originates from the upstream SOL, above the RDPA coverage. This is apparent from the nearly flat total vertical ion flux along the entire outer divertor leg. The Mach number (not shown here) is fairly constant throughout the entire profile and stays within the 0.4 to 0.6 range. As opposed to the other discharges, the ion flux even slightly decreases

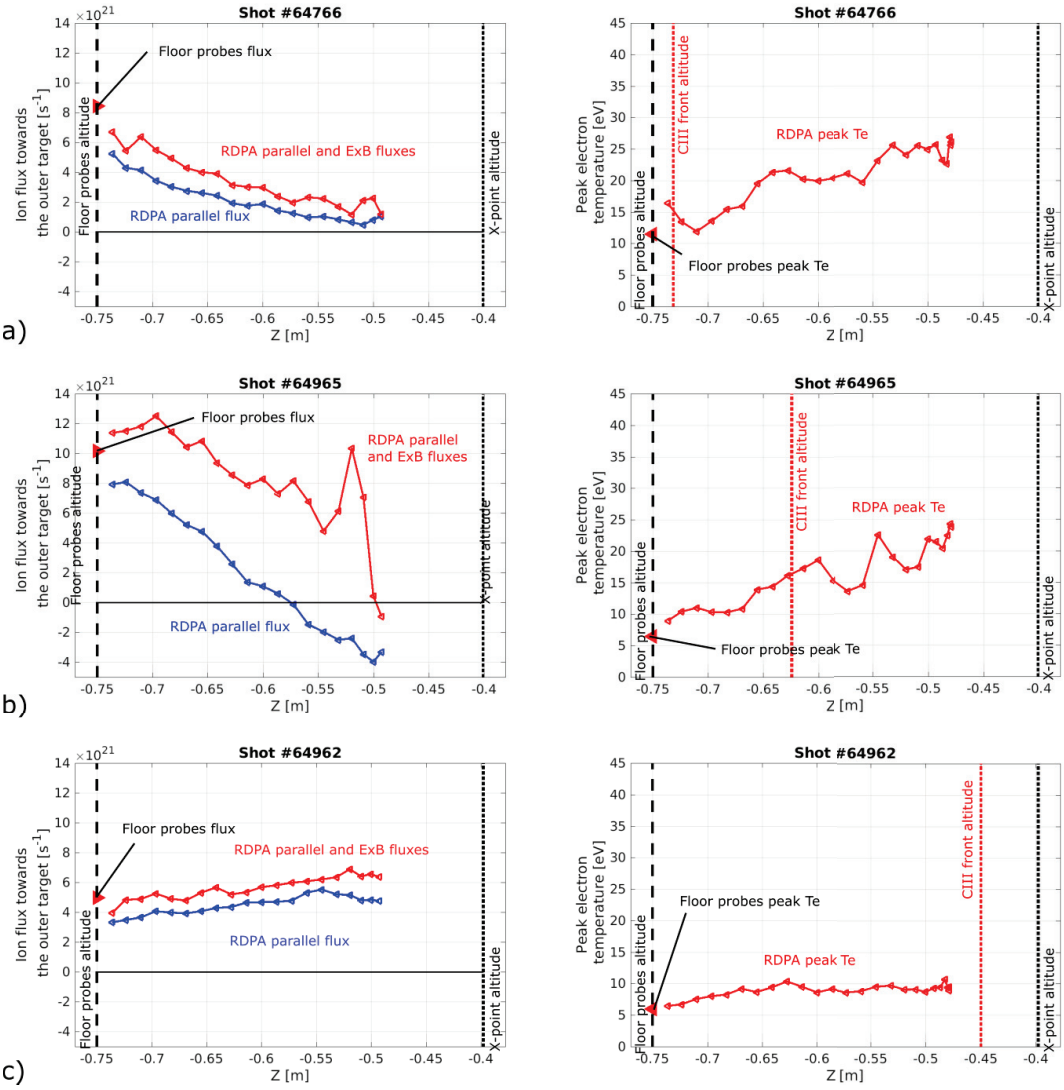

Figure 4.13: **a)** Low core density references #64766 $\langle n_e \rangle \approx 5.5e19[m^{-3}]$, **b)** High core density reference #64965 $\langle n_e \rangle \approx 10.5e19[m^{-3}]$ and **c)** Highest core density reference #64962 $\langle n_e \rangle \approx 11.5e19[m^{-3}]$ (beyond roll-over).

towards the target, with ≈ 20% of the flux missing. This missing flux could be attributed to volumetric recombination. Indeed, both spectroscopic studies [63] and SOLPS simulations [61] have shown the presence of modest levels of recombination for detached L-mode TCV plasmas. The probability for recombination becomes larger than the probability for ionisation below $T_e \approx 1.5\ eV$. However, molecular activated recombination (MAR) is a possible candidate to explain the missing ion flux [125] [126] occurring at higher electron temperatures, up to $T_e \approx 3\ eV$. It should be emphasized that the recombination measurement from the RDPA data is prone to a large error since any absolute error on the particle flux density measurement could lead to a much larger relative error on the recombination fraction estimation.

The electron temperature is not high enough to ionise neutral along the entire scan. $T_e \approx 6\ eV$ according to the Langmuir probe measurement, however due to the T_e overestimation in this regime, $T_e < 5\ eV$ is expected.

4.4.3 The effect of baffles for a given core density

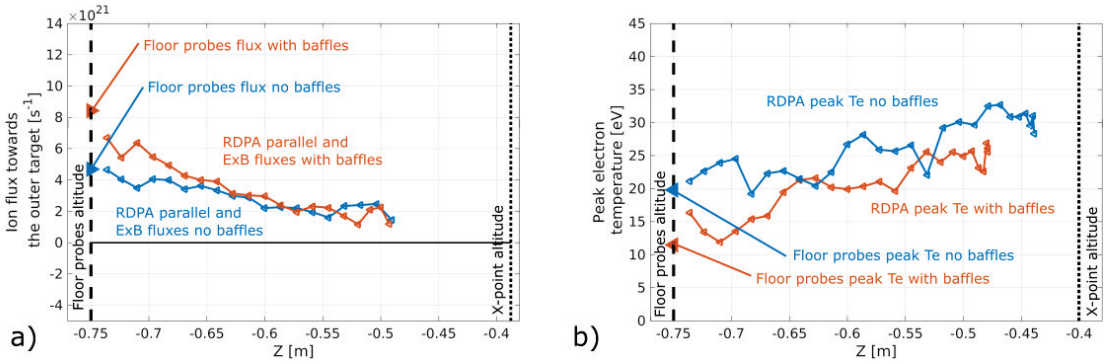

Figure 4.14: Low core density reference $\langle n_e \rangle \approx 5.5e19[m^{-3}]$ without baffles #65964 and with baffles #64766. **a)** Total ion flux to the outer target, integrated radially and toroidally, and **b)** Peak electron temperature value.

The effect of the baffles on the detachment onset, already seen in FIG. 4.4, became clearly apparent for the particle balance analysis shown in FIG. 4.12 and 4.13. Here, we compare in more detail the lowest density discharge, for which an excellent match of the core quantities was achieved, see FIG. 4.3. Indeed, in this figure, it can be seen that the significant differences between the non baffled reference and the baffled reference are present only in the radiated power, the gas flux required for fuelling and the divertor neutral pressure. Bolometry data shows that the increase in radiated power is mainly originating from the divertor (inner leg, outer leg and X-point region), whose lower temperature and higher density than the case without baffles are expected to enhance both carbon impurity and hydrogenic radiated power. However the carbon impurity fraction in both discharges is unknown and could also be a key player to explain the difference in radiated power.

The direct comparison enables to see clearly the higher level of divertor ionisation in the baffled case, see FIG. 4.14 **a)**: more flux arrives at the target. Similar or even slightly smaller amounts enter from upstream. This higher ionisation level is expected [61] because the larger neutral density combined with sufficient plasma temperature lead to a larger ionisation term. Moreover, the lower electron temperatures in the baffled case becomes explicitly apparent in FIG. 4.14 **b)**.

4.5 Conclusion

This chapter reported detailed 2D Langmuir probe measurements across a large part of the divertor region in TCV. The measured quantities include plasma density, temperature, potential and parallel Mach number. Deducing from these measurements vertical particle flux densities associated both with parallel flows and $E \times B$ flows allows for a particle balance analysis in the divertor. These measurements are applied to Ohmic L-mode plasmas in both baffled and non-baffled configurations and different divertor regime, are accessed by varying the plasma line-averaged density. In order to access high-density conditions, these experiments are performed at a relatively high plasma current of approx. 320 kA and in unfavourable ion-grad B drift direction to avoid transitions to H-mode.

The baffles are found to substantially increase divertor neutral pressure and to facilitate the detachment onset, effects similar yet even stronger as in recent experiments with the new TCV baffles in 250 kA L-mode plasmas [41] [120]. Results from density ramps and constant density shots agree, at corresponding densities, in terms of the integrated ion flux, the $CIII$ front position and the divertor neutral pressure.

This study reveals that the contributions of the $E \times B$ drift to the poloidal ion flux is comparable and sometimes larger than that due to the ion flux along the magnetic field, consistent with previous observations in $DIII-D$ [91] [92] [111]. Detailed particle balance in the divertor reveals that in most cases and both with and without baffles, most of the particle flux arriving at the outer target is due to ionization along the outer divertor leg. This justifies the closed-box approximation frequently used in detachment models [124] [46] and previously inferred on TCV from spectroscopic measurements [127]. Close to the detachment onset in these reversed field conditions, the integrated parallel flow is even 'reversed' just below the X-point, i.e ions are flowing upstream, while the total flow including the $E \times B$ drift remains positive, i.e. directed towards the target.

In the most detached conditions, the divertor leg become too cold for any ionization to occur. In this extreme case, achieved only with baffles in these experiments, the entire particle source is located around and above the X-point, and the flux along the divertor leg even drops slightly, ascribed to plasma recombination [125].

A close match between the attached, lowest density discharges with and without baffles, in terms of upstream properties such as line-averaged density, reveal a substantial increase of the divertor ionisation level in the presence of the baffles. In addition, divertor electron temperatures are reduced by approximately 35%.

5 Insights on the competition of conductive and convective heat fluxes in the TCV divertor

Following the detailed divertor particle balance study in the previous chapter, we explore here the different contributions to divertor heat fluxes in the outer divertor leg, along the vertical direction. As the outer divertor leg if nearly vertical, this heat flux analysis corresponds, to a good approximation, to a heat flux analysis in the poloidal direction. Similarly as for the particle fluxes, the heat flux terms considered include contributions due to parallel flows and $E \times B$ drifts. Furthermore, the contribution from parallel conductive heat transport is included, which, in many SOL models, is assumed to be the dominant contributor in attached divertor conditions [38]. Turbulent heat flux measurements are not accessible with RDPA. However, since they act mainly in the radial direction, their omission is not expected to have a large impact on the present study. A brief discussion on the model used to interpret the data is given in SEC. 5.1, followed by the presentation of an example result in SEC. 5.2 and a conclusion in SEC. 5.3. This chapter serves as a proof of principle, however, uncertainties on the results are high due to the limitations of the diagnostic (spatial resolution, error on the electron temperature measurement at high collisionnality).

5.1 Procedure for heat flux calculations

A formula for the heat flux equation in $1D$ along the magnetic field direction can be found in [38], section 9.9, for a fluid isothermal plasma:

$$\frac{d}{dx}\Big[(\frac{1}{2}m_i v_\parallel^2 + 5eT)nv_\parallel - \kappa_0 T_e^{5/2}\frac{dT_e}{dx}\Big] = Q_R + Q_E, \tag{5.1}$$

where $v_\parallel$ is the plasma fluid velocity, $T = T_i = T_e$ is the plasma temperature expressed here in $[eV]$, $\kappa_0 \approx 2000$ [38] is the thermal conductivity coefficient (thermal conduction is almost entirely due to electrons), Q_R is the volumetric joule heating (expected to be small in the SOL in TCV) and Q_E is the term accounting for other heat flux sources and sinks (power from neutrals being ionized, power lost to ionization, power lost to excitation, power lost to

impurities, etc...).

The kinetic energy term $\frac{1}{2} m_i v_\parallel^2$ can be neglected for typical TCV conditions ($M \leq 0.5$) when compared to the convective term $5eT$:

$$\frac{\frac{1}{2} m_i v_\parallel^2}{5eT} = \frac{\frac{1}{2} m_i \left(M \sqrt{\frac{2eT}{m_i}}\right)^2}{5eT} = \frac{M^2}{5} \leq 5\%. \tag{5.2}$$

The relevant formula for the parallel heat flux is then:

$$q_\parallel = 5eTnv_\parallel - \kappa_0 T_e^{5/2} \frac{dT_e}{dx} \tag{5.3}$$

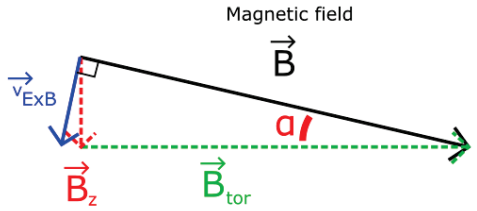

Figure 5.1: Illustration of the projection of the magnetic field vector onto the vertical vector.

The computations performed to obtain the n and $v_\parallel$ measurements are described in SEC. 4.3. Once we project the $1D$ equation in the vertical direction (close to the poloidal direction), the pitch angle of the magnetic field line must be taken into account, see FIG. 5.1. The parallel heat flux projection on the vertical direction becomes:

$$q_{z,\parallel} = q_\parallel \frac{\vec{B}}{\|\vec{B}\|} \cdot \frac{\vec{B}_z}{\|\vec{B}_z\|} = q_\parallel \sin\alpha. \tag{5.4}$$

In addition to the parallel heat fluxes due to convection and conduction, cross-field heat convection due to $E \times B$ drifts is also accounted for in the following. The computations performed to obtain $E \times B$ measurements are described in SEC. 4.3.2. If projected in the vertical direction, the $E \times B$ contribution to the heat flux is given by:

$$q_{z,E\times B} = 5eTn \frac{\vec{v}_{E\times B} \cdot \vec{B}_z}{\|\vec{B}_z\|} = 5eTn \|\vec{v}_{E\times B}\| \cos\alpha. \tag{5.5}$$

5.2 Heat flux profiles

In order to calculate the temperature gradient in the parallel direction, as needed for EQ. (5.3), the RDPA temperature matrix needs to be interpolated radially, see the transition from FIG. 5.2 **a)** to **b)** and then later interpolated in the parallel direction (interpolation of the data points with the same magnetic coordinate dr_{sep}). The second interpolation is necessary to avoid artificial bumps in the temperature gradient $\frac{dT_e}{dx}$. Such interpolations of the RPDA data have

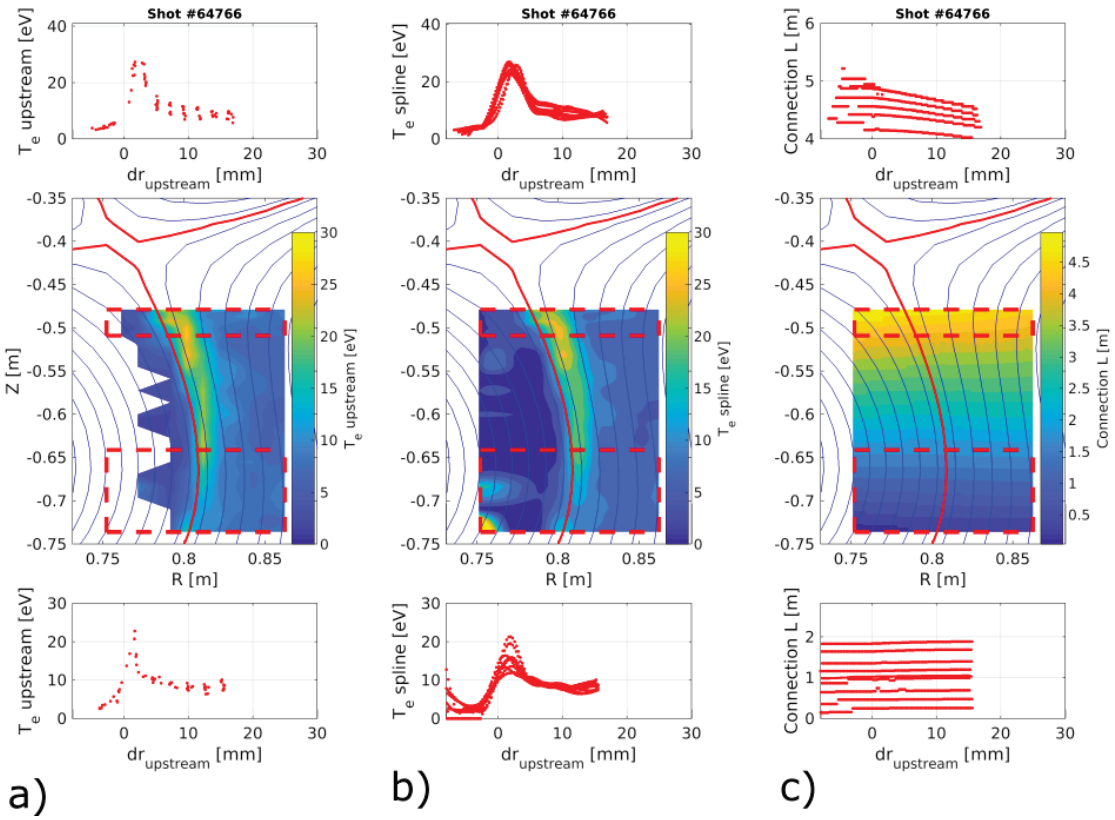

Figure 5.2: **a)** Electron temperature measurement from upstream tips of RDPA, **b)** spline interpolation of the data in **a)** necessary for the parallel temperature gradient calculation and **c)** parallel connection length obtained with the routine *sol _geometry.m* for the shot 64766 ($I_p \approx 320\ kA$, unfavourable field for H-mode access, with baffles, $\langle n_e \rangle \approx 5.5e19\ m^{-3}$).

been done here as an exception in this thesis, all the other results have been computed from the RDPA grid results.

The connection length as a function of R and Z coordinates is obtained for the main SOL from the routine *sol_geometry.m*. This routine does not track field lines in the private flux region and, therefore, the connection length values in the private flux region have been obtained from a constant extrapolation of the value at the separatrix. This simplification could lead to a large error on the connection length close to the X-point and should be improved in the future. However, this simplification is not expected to change the results for the example shown in this section, far from the X-point region. Eventually, to obtain the parallel electron temperature gradient, the finite difference along a flux surface of the electron temperature in FIG. 5.2 **b)** is divided by the finite difference along a flux surface of the connection length in FIG. 5.2 **c)**. Finally, the parallel heat flux evaluated in this way is projected along the z-axis.

The heat fluxes from parallel convection, $E \times B$ convection, electron conduction and the total heat flux, projected along the vertical direction, have been evaluated for the shot 64766 (attached L-mode, $I_p \approx 320\ kA$, unfavourable field for H-mode access, with baffles, $\langle n_e \rangle \approx$

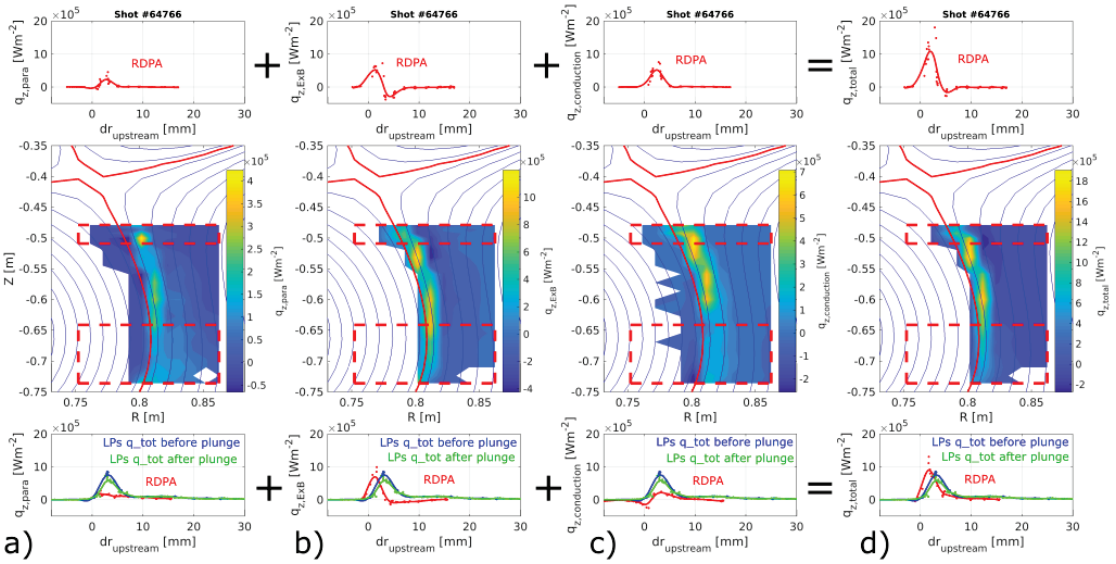

Figure 5.3: Different contributions to the heat fluxes projected onto the vertical direction (close to the poloidal direction): **a)** parallel convection, **b)** $E \times B$ convection, **c)** electron conduction and **d)** total heat flux for the shot 64766 ($I_p \approx 320\ kA$, unfavourable field for H-mode access, with baffles, $\langle n_e \rangle \approx 5.5e19\ m^{-3}$). The heat flux profile from floor LPs is shown in the bottom plots as a reference, calculated with a sheath heat transmission factor of $\gamma_{sh} = 6$.

$5.5e19\ m^{-3}$), see FIG. 5.3. Electron conduction and $E \times B$ convection represent the most important contributions to the overall heat flux. The peak heat flux is ≈ 20% lower at the target than near the X-point, possibly because of a heat sink and/or due to cross field radial heat transport. Interestingly, the total heat flux profile from RDPA agrees with the heat flux profile from the floor LPs, obtained with a sheath heat transmission factor of $\gamma_{sh} = 6$, see FIG. 5.3 **d)**. The same agreement is not always observed in other experiments, mostly because of the large uncertainties from electron temperature measurements, which has repercussion of the conductive and $E \times B$ convective heat fluxes.

An attempt at using the Eich fit [37] for the total heat flux profiles along the divertor leg was not successful for the example from FIG. 5.3: the scatter on the S and λ_q results from the fit was unacceptably large. The presence of negative heat flux values (directed towards the upstream SOL) caused by $E \times B$ drifts renders the fit and the interpretation of the S and λ_q results difficult.

5.3 Conclusion

A proof of principle test of divertor power balance with RDPA has been performed for an attached L-mode plasma. This reveals that, in the case of attached plasmas, the parallel conductive and the ExB convective heat fluxes have the most significant contribution to the total heat flux, while parallel convection plays a weaker role. The sum of all these heat fluxes agrees with heat flux measurements from the floor probes for the given example. However,

this is not always the case in other experiments, probably because of the large uncertainty of electron temperature measurements, which has direct repercussions on the conductive and $E \times B$ convective heat fluxes calculations. Future studies would benefit from a higher spatial resolution, achievable from grouping data from several RDPA plunges combined with slight divertor leg movements. Such a study could then also allow to evaluate the level of poloidal heat flux spreading along the divertor leg.

6 Insights on divertor fluctuations

Turbulence and related transport in the SOL and divertor of tokamaks and their dependence on divertor regime and magnetic geometry is one of the main open issues for the development of a robust exhaust solution. A key new feature of RDPA is to provide detailed, local measurements of fluctuation characteristics across the divertor volume of TCV, opening up new paths to experimentally explore divertor turbulence and provide stringent benchmarks for numerical simulations. These capabilities have only been started to be explored and a few examples and works in progress are presented in this final chapter.

6.1 Procedure for the calculations of the RDPA density fluctuations measurement

Performing electron temperature or even ion temperature measurements at the plasma turbulence timescale is not possible with the conventional single Langmuir probe electronics used in this study. Fortunately, density fluctuation measurements are more accessible because $J_{sat} \propto c_s n_e$ fluctuations are dominated by the density fluctuations [128], [129]. This observation can be partially explained by the relatively weak dependence of c_s on the electron temperature (square root dependence). It should, however, be noted here that the electron temperature fluctuations can not be neglected in the case of plasma potential fluctuations studies [128] [130].

Density fluctuations are calculated from the standard deviation of the I_{sat} time windows. The typical duration of a time window is approximatively 1 ms (equivalent to 2000 acquired time points at a 2 MHz frequency). The time windows can be recorded while operating the probe in I_{sat} mode or in voltage sweeping mode, considering only the intervals when the probe voltage is sufficiently negative for the probe to record I_{sat}. In the private flux region, the $\widetilde{J_{sat}}$ and $\widetilde{n_e}$ signals (the tilde symbol stands for the standard deviation of the signal) are dominated by the instrumental noise. The standard deviation of the noise is recorded before the plasma discharge and then subtracted assuming that the signal and the noise are independent random

variables, and therefore, the variance of their difference is given by:

$$\sigma_{signal} = \sqrt{\sigma^2_{measurement} - \sigma^2_{noise}} \tag{6.1}$$

The density fluctuations are given from the formula discussed in SEC. 4.3.1:

$$\widetilde{n_e} = \widetilde{\left(\frac{J_{sat1}/e}{c_s \exp(-1+1.1M)}\right)}. \tag{6.2}$$

Fluctuation levels are then approximated as follows:

$$\widetilde{n_e} \approx \frac{1}{\langle c_s \rangle} \widetilde{\left(\frac{J_{sat1}/e}{\exp(-1+1.1M)}\right)}, \tag{6.3}$$

where $\langle c_s \rangle$ is the time-averaged, local sound speed, obtained from processing the time averaged data from swept probes. The normalised fluctuation level is approximated as follows:

$$\frac{\widetilde{n_e}}{\langle n_e \rangle} = \widetilde{\left(\frac{J_{sat1}/e}{\exp(-1+1.1M)}\right)} / \frac{\langle J_{sat1} \rangle / e}{\exp(-1+1.1\langle M \rangle)}. \tag{6.4}$$

6.2 Effect of baffles and core density on fluctuation levels

The measurements enabled by RDPA allow us to gain insights on divertor density fluctuation levels in different divertor regimes. We will focus on two examples here: a well-attached, low density, non baffled discharge (#65964 in **a)**, **b)** and **c)** from FIG. 6.1) and a high density baffled discharge (#64965 in **d)**, **e)** and **f)** from FIG. (6.1), which is just at the onset of detachment.

In the low density example, fluctuation levels are almost constant along flux surface in the divertor leg, see FIG. 6.1 **c)**. The data has been arbitrarily divided in four distinct regions to facilitate the description of the results, see FIG. 6.2 and FIG. 6.1 **c)**: ① The first region, in the private plasma, is characterised by a relatively quiescent region with faint plasma. ② In the second region, close to the separatrix, on the left of the electron temperature peak (region of strong downward $E \times B$ drift), a large fluctuation level is surprisingly observed, with $\widetilde{n_e}/\langle n_e \rangle \approx 0.5$. The origin of the large fluctuation intensity is unknown. A hypothesis would be that the turbulence could be generated at the divertor inner leg and then be transported poloidally by the strong $E \times B$ drifts. Another hypothesis would be that the local shear properties can drive Kelvin-Helmholtz instabilities. ③ The third region is near the electron temperature peak. The density fluctuation level in this region is the lowest $\widetilde{n_e}/\langle n_e \rangle \approx 0.1$. ④ The fourth region is on the right of the electron temperature peak. The density fluctuation level increases gradually from $\widetilde{n_e}/\langle n_e \rangle \approx 0.1$ to $\widetilde{n_e}/\langle n_e \rangle \approx 0.25$ in the far SOL. The higher fluctuation level in the far SOL is believed to be caused by reconnection with upstream turbulence. Indeed, the reconnection process was recently shown in the far SOL of TCV in similar low collisionnality discharges by tracking convective cells with the Gas Puff Imaging (GPI) diagnostic [131] and with wall LPs at

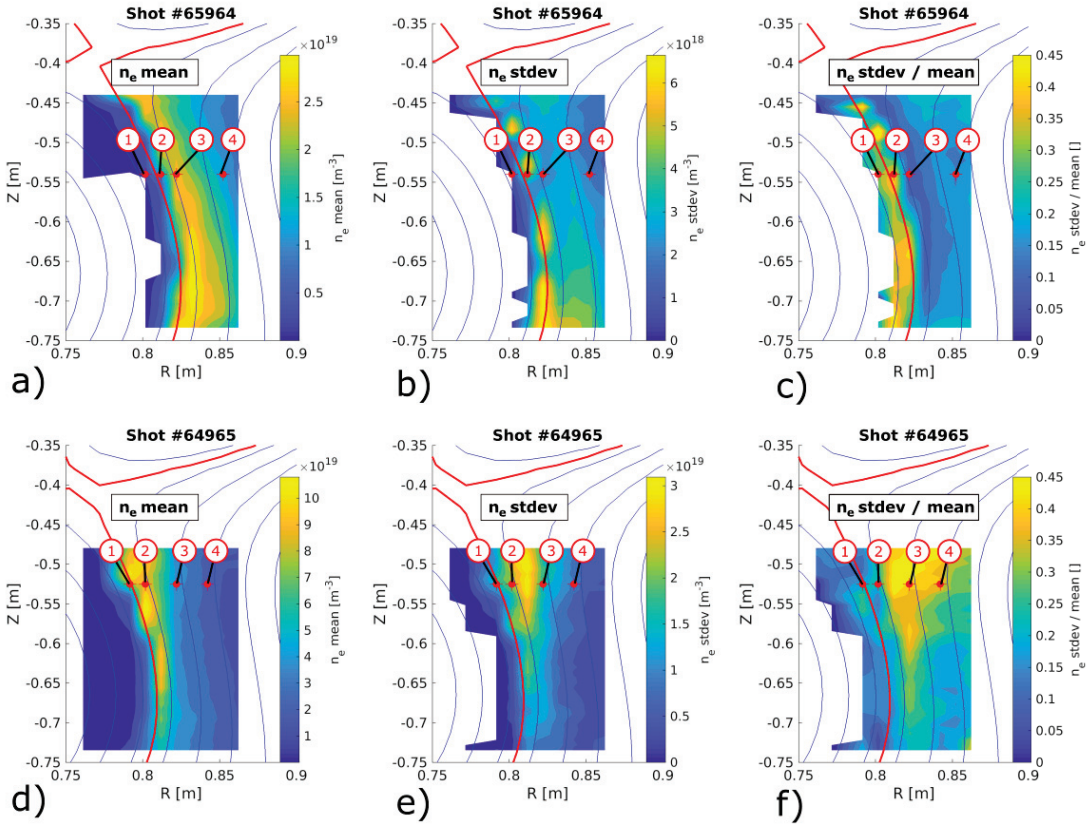

Figure 6.1: Data from the low density shot #65964 and the high density shot #64965 to illustrate the density fluctuation profiles in various conditions: **a)** and **d)** time averaged electron density, **b)** and **e)** standard deviation of the density and **c)** and **f)** standard deviation normalised by the time averaged density. The labels ① to ④ correspond to the position of the J_{sat} time traces shown in FIG. 6.2 and 6.3.

the same time and mapped along field lines.

In the high density example, the turbulence behaviour is very different than for the low collisionnality plasma. The relative fluctuation levels are not constant along flux surfaces, as shown in FIG. 6.1 **f)**. The data has been once again arbitrarily divided in four distinct regions, although at slightly different positions, to facilitate the description of the results, see FIG. 6.3 and FIG. 6.1 **f)**: ① As for the low density reference, the private plasma is characterised by a relatively quiescent region with faint plasma. ② The second region, on the left of the electron temperature peak, has little fluctuation level $\widetilde{n_e}/\langle n_e\rangle \approx 0.2$ which contrasts with the low density reference. The narrow, high fluctuation level feature, seen in the low density reference, seems to have disappeared with increasing collisionnality. ③ In the main SOL region, where fluctuations are believed to be related to the upstream turbulence, a strong reduction in fluctuation levels is observed from $\widetilde{n_e}/\langle n_e\rangle \approx 0.45$ near the X-point down to $\widetilde{n_e}/\langle n_e\rangle \approx 0.2$ near the target. This drop coincide with the electron temperature drop shown in

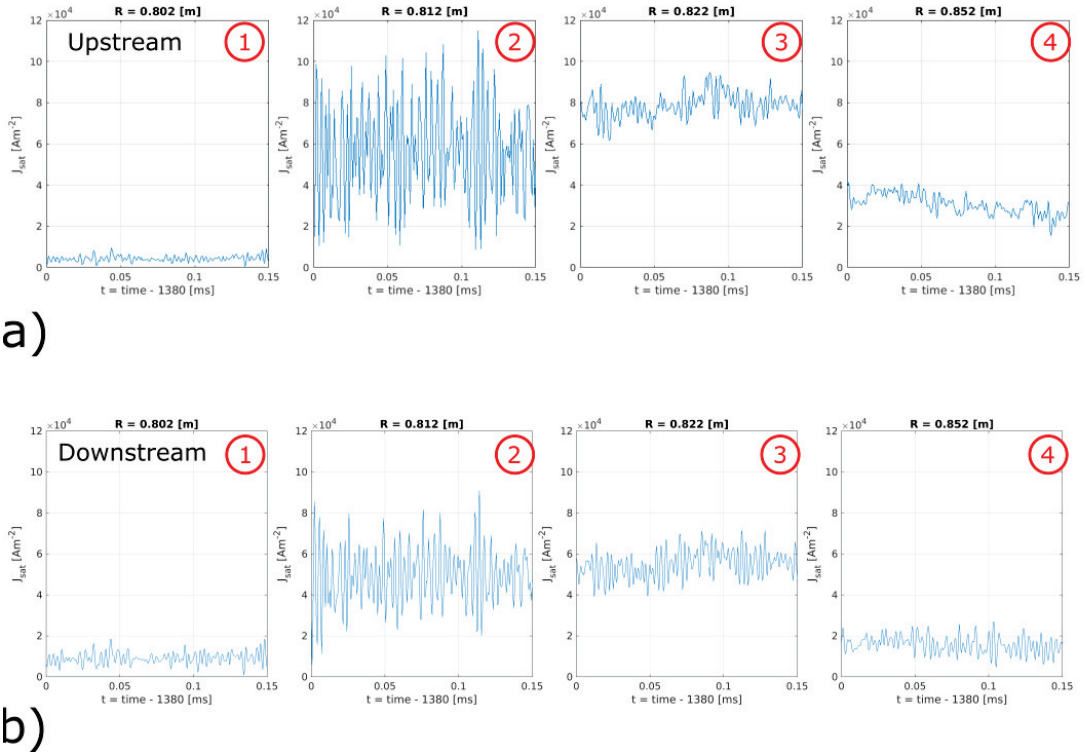

Figure 6.2: Ion saturation current density time traces from the low density shot without baffles #65964: signal from the **a)** upstream and **b)** downstream probe tips. The labels ① to ④ and the positions of the corresponding data point in the poloidal plane are shown in FIG. 6.1 **a)**.

FIG. 4.13 **b)** and with the associated increasing collisionnality. ④ Finally, in the fourth region, the far-SOL, turbulent events are less frequent, probably due to the lower probability for the blobs to arrive this far in the SOL.

6.3 Ongoing contributions to turbulence code validation studies

The global, two-fluid boundary turbulence codes GBS [67], developed at the SPC-EPFL, provides a first-principles approach to explore tokamak boundary physics. Relatively recently, the code has been updated in order to allow so simulate arbitrary, diverted tokamak geometries [132] [133]. Ongoing studies are carried out where divertor physics is explored in a combined effort of numerical simulations and dedicated experimental studies on TCV, and where data from the RDPA is playing a significant role.

These ongoing efforts include the modelling of a realistic TCV diverted L-mode plasma. Plasma density profiles for a forward field GBS simulation of TCV are shown in FIG. 6.4 **a)**, **b)** and **c)** and the RDPA results for the corresponding experiment are shown in FIG. 6.4 **d)**, **e)** and **f)**. The comparison is only qualitative in this case since the simulation has been performed on half the size of TCV, in order to reduce the computational time necessary to attain convergence of

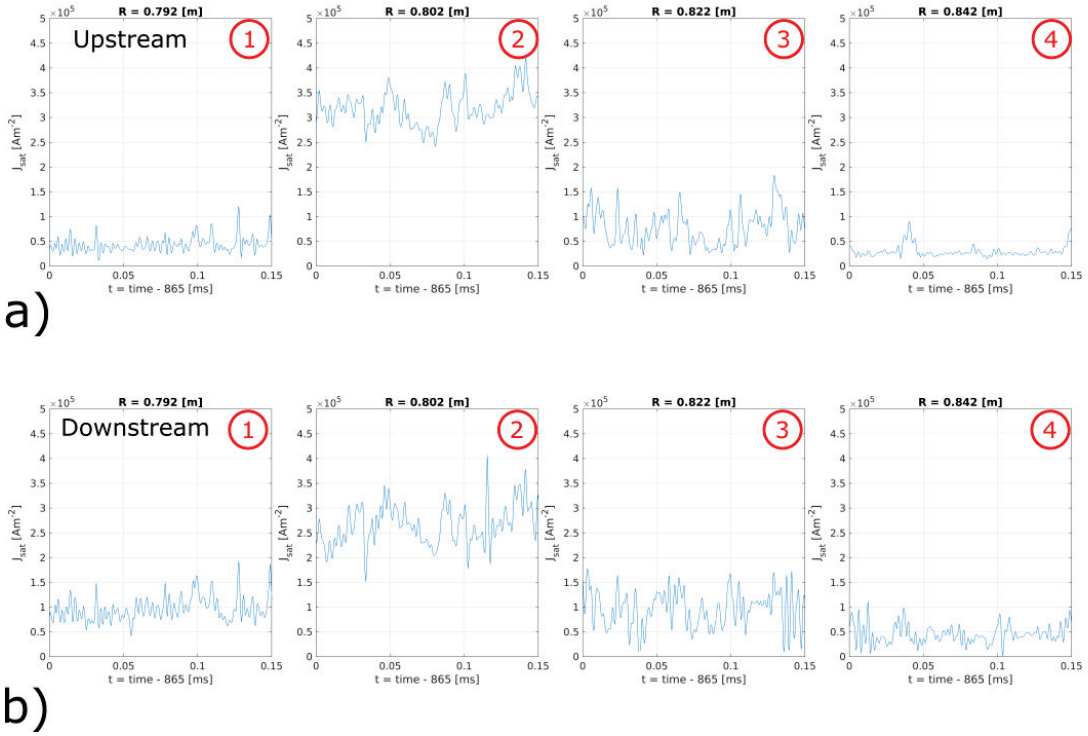

Figure 6.3: Ion saturation current density time traces from the high density shot with baffles #64965: signal from the **a)** upstream and **b)** downstream probe tips. The labels ① to ④ and the positions of the corresponding data point in the poloidal plane are shown in FIG. 6.1 **b)**.

the simulation. However, recent progress on the code will soon allow full size simulations of TCV. The toroidal field has been chosen experimentally to facilitate the simulation $B_{tor} = 0.9\ T$ instead of the commonly used value in TCV $B_{tor} = 1.4\ T$.

The time averaged density in the outer divertor leg is ≈ 2 times larger in the experiment than in the simulation, see FIG. 6.4 **a)** and **d)**. The relative fluctuation levels of the density in the experiment, $\widetilde{n_e}/\langle n_e \rangle \leq 0.4$, are comparable with that of the simulation snapshot $(n - \langle n_e \rangle)/\langle n_e \rangle \leq 0.3$. Interestingly, the high fluctuation level observed near the separatrix in the reversed field, high plasma current discharge in FIG. 6.1 **c)** is absent the present experiment in forward field, see FIG 6.4 **f)**. Instead, the separatrix region is quiescent and the fluctuation levels are the highest in the far-SOL. A quiescent plasma near the outer divertor leg separatrix and a turbulent far-SOL are also observed in the simulation, see 6.4 **b)** and **c)**.

6.4 Conclusion and future work

A variety of fluctuation results have been presented in this chapter, in order to introduce the capabilities of the RDPA. Some of the main observations include the development of a poloidal gradient of the fluctuation levels, observed with increasing collisionnality, and the surprising

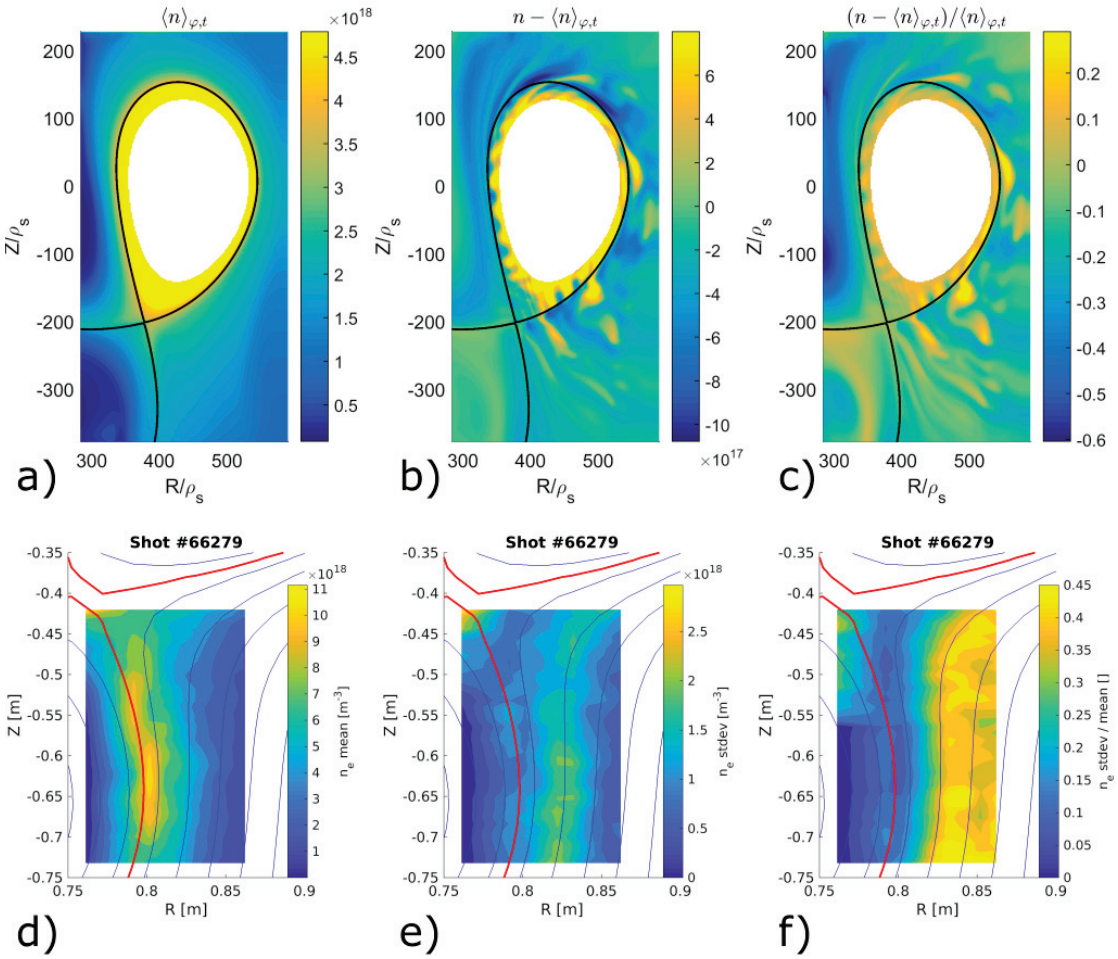

Figure 6.4: Results from a forward field GBS simulation of half-size TCV: **a)** time average density, **b)** difference between a density snapshot and the time averaged density and **c)** relative difference between the density snapshot and the time averaged density. RDPA results from one of the corresponding experiment ($I_p \approx 160\ kA$, $B_t \approx 0.9\ T$, $\langle n_e \rangle = 2.9e19\ m^{-3}$, favourable field direction for H-mode access): **d)** time averaged density, **e)** standard deviation of the density fluctuations and **f)** standard deviation of the density fluctuations divided by the time averaged density.

presence of a narrow, high fluctuation level, region in the downward $E \times B$ region for a well attached, reversed field, discharge.

Ongoing efforts focus on using RDPA results to validate the turbulent fluid code GBS. A first, qualitative, comparison between the density fluctuation profiles from a half-size TCV simulation and the RDPA results for the corresponding experiment has been given. The time averaged density in the divertor is higher in the experiment than in the simulation. However, the relative density fluctuations have similar values. Recent progress on the GBS code will permit full size TCV simulations and, therefore, an improved comparison in the future.

Several tasks could be initiated in the future to make progress in the description of the divertor fluctuation properties for RDPA such as: cross correlation with J_{sat} and V_{float} signals thanks the split Mach tip configuration, and the estimation of blob sizes, which could be approximated with the product of the fluctuation period and the cross field velocity, which is often dominated by $E \times B$ drifts.

7 Conclusion

The present thesis work includes operation, maintenance and upgrades of wall-embedded Langmuir probe system in the TCV tokamak. In particular, the TCV wall probe coverage has been extended from 114 to 194 probes. In order to operate all these probes simultaneously, rather than switching probe connections between different experiments, the array of Langmuir probe amplifiers has been extended from 48 to 216. Compared to the first generation amplifiers developed at the SPC-EPFL, the new set features a number of improvements. The higher number of amplifiers operated simultaneously results in a larger failure rate, occurring mostly during off-normal events such as disruptions and ELMs. Among the different solutions explored to date, the most efficient is the addition of extra resistors to avoid current surges in combination with surge protectors to avoid voltage spikes. The standard analysis for swept Langmuir probes on TCV has been extended to obtain inter-ELM profiles in H-mode plasmas, achieved by an interactive tool to correctly filter out the ELM periods from the raw data.

In parallel, a novel fast probe array, dubbed RDPA, has been designed, built and commissioned at TCV, providing unprecedented $2D$ Langmuir probe measurements across the divertor of quantities temporally resolved at the turbulence time scales , such as J_{sat}, M, $\Gamma_{\parallel}$, V_{float} and n_e (assuming a constant c_s), and time averaged quantities that necessitates a sweeping of the bias voltage, such as T_e, n_e, V_{plasma}, $v_{\parallel}$ and $v_{E\times B}$. In contrast to reciprocating probes accessing the divertor region of other major tokamaks, the RDPA provides $2D$ measurements in a single reciprocation, enabled by a radial array of probe tips moved vertically across an extended region of the divertor volume. No sign of damage could be seen on the probe after more than 200 experiments performed, including more than ≈ 20 disruptions happening while the diagnostic was in motion. The physics results are consistent with other reference diagnostics (electron Thomson scattering upstream and wall embedded Langmuir probes downstream) for most plasma conditions, showing that the design is sufficiently compact to provide measurements representative of the unperturbed plasma parameters. Further RDPA development and interpretation tasks have been identified such as improving the transmission

lines, lowering the amount of recycled neutrals in the measured flux tube to possibly improve the density measurement, and developing a model for the interpretation of the asymmetries between upstream and downstream floating potentials.

The RDPA capabilities have allowed for a detailed particle balance study in the outer TCV divertor in attached and detached conditions and both with and without the recently installed divertor baffles. These measurements are applied to Ohmic L-mode plasmas and different divertor regimes, accessed by varying the plasma line-averaged density. The baffles are found to substantially increase divertor neutral pressure and to facilitate the detachment onset, effects similar yet even stronger as in recent experiments with the new TCV baffles in 250 kA L-mode plasmas. The particle balance study reveals that the contributions of the $E \times B$ drift to the poloidal ion flux is comparable and sometimes larger than that due to the ion flux along the magnetic field, consistent with previous observations in the $DIII-D$ tokamak. Except for strongly detached conditions, most of the particle flux arriving at the outer target is due to ionization along the outer divertor leg. This justifies the closed-box approximation frequently used in detachment models and previously inferred on TCV from spectroscopic measurements. Indeed, in the most detached conditions, the divertor leg become too cold for any ionization to occur. In this extreme case, the entire particle source is located around and above the X-point, and the flux along the divertor leg even drops slightly, ascribed to plasma recombination. A close match between the attached, lowest density discharges with and without baffles, in terms of upstream properties such as line-averaged density, reveal a substantial increase of the divertor ionisation level in the presence of the baffles.

A proof of principle test of identifying the dominant divertor heat flux channels with RDPA has been performed for an attached L-mode plasma. This reveals that, in attached plasmas, the parallel conductive and the ExB convective heat fluxes have the most significant contribution to the total heat flux, while parallel convection plays a weaker role. The sum of all these heat fluxes agrees with heat flux measurements from the floor probes for the given example. However, this is not always the case in other experiments, probably because of the large uncertainty of electron temperature measurements, which has direct repercussions on the conductive and $E \times B$ convective heat flux calculations. Future studies would benefit from a higher spatial resolution, achievable through grouping data from several RDPA plunges, combined with slight divertor leg movements. Such a study could then also allow evaluating the level of poloidal heat flux spreading along the divertor leg.

Finally, a variety of fluctuation results have been presented, in order to introduce the capabilities of the RDPA in this respect. Some of the main observations include the development of a poloidal gradient of the fluctuation levels, observed with increasing collisionnality, and the surprising presence of a narrow, high fluctuation level region in the downward $E \times B$ region for a well attached, reversed field, discharge. Ongoing efforts focus on using RDPA results to validate the turbulent fluid code GBS. A first, qualitative comparison between the density fluctuation profiles from a half-size TCV simulation and the RDPA results for the corresponding experiment has been presented. Recent progress on the GBS code will permit full size

TCV simulations and, therefore, an improved comparison in the future. Several tasks could be initiated to improve the description of the divertor fluctuation properties for RDPA such as: cross correlation with J_{sat} and V_{float} signals thanks to the split Mach tip configuration, and the estimation of blob sizes, which could be approximated with the product of the fluctuation period and the cross field velocity, which is often dominated by $E \times B$ drifts.

To conclude, strong enhancements of the wall-embedded Langmuir probe system in the TCV tokamak and the design and construction of a novel fast probe array, dubbed RDPA, have enabled a better description of the plasma properties in the TCV divertor as well as advanced physics studies, such as a divertor particle balance, a first assessment of the nature of the dominant poloidal heat flux channels in the TCV divertor and the measurement of 2D turbulent fluctuation profiles in the divertor volume.

A Appendix: RDPA user manual

A.1 RDPA disassembly in TCV

a. Remove all the Plexiglas protections.

b. Remove all the aluminum structure in order to clear access.

c. Disconnect the safety switches. There is a 24 V tension across the safety line with ≈ 8 safety switches in series. If the line is open, the contactor will cut the high voltage 220 V supply to the motor driver, resulting in the fault "Amplifier fault" on the Soloist® software as soon as the motor is enabled. This is not a problem since using the motor is not required during disassembly.

d. Disconnect cables from the BNC patch panel and from the atmospheric side of the SMA feedthrough.

e. OPTIONAL STEP: The vacuum technician can go in the torus in order to install the red plastic protection around RDPA. This protection serves as a sliding layer between the rectangular vacuum vessel extension and the RDPA graphite PFCs during disassembly. This step is optional and should be discarded in the future.

f. A rope (climbing rope) is attached around the TF coil from sector 3.b. A manual hoist is attached to the rope. The rope length must be chosen in order for the hoist chain to span the range of movement necessary for the disassembly.

g. At the end of the manual hoist chain, a carabiner is attached to the metallic structure of the moving assembly of RDPA, near the entrance of the cable chain. Sometimes the carabiner is stopped by the RDPA aluminum structure. It is therefore important to clear the path for the carabiner motion.

h. The manual hoist is set slightly under tension before removing the brake.

i. The manual switch on the RDPA Plexiglas is turned on in order to be able to remove the

brake by typing the command “BRAKE OFF” on the Soloist® software.

j. The moving assembly of RDPA should now be at a position $Z_{motor} \approx -5\ mm$ due to the tension in the rope/chain released from the position $Z_{motor} = 0\ mm$.

k. Remove the stop at $Z_{motor} \approx 5\ mm$ by removing the 6 screws on the vertical plate.

l. The RDPA moving assembly is slowly lowered by releasing the chain of the manual hoist until the length is sufficient to install the wooden support. This wooden support is necessary to support the weight the flange that will be unscrewed in the next step. If the wooden support is not installed, the flange would fall and compress the vacuum bellow.

m. Unscrew the vacuum flange at the beginning of the rectangular vacuum vessel extension.

n. The RPDA moving assembly is lowered $\approx 5\ cm$, until there is enough space to screw the wooden support to the flange with M8 screws on top of plastic washers to protect the flange knife. The wooden support can stand without these two screws. However it could quickly fall in case of a wrong movement.

o. The RDPA moving assembly is lowered $\approx 50\ cm$ until the aluminum part holding the motor will hit the lower stop (the lower stop is never disassembled). At this point all of the RDPA system should be out of the rectangular vacuum vessel extension.

p. The manual power switch on the RDPA Plexiglas is turned off. The system will automatically turn the brake once the power switch is turned off.

q. The optional tape around the red plastic protection is removed and the RDPA Plasma Facing Components (PCFS) are now visible.

r. A plastic cover is installed on the vacuum vessel extension in order to protect the stainless steel knife of the flange.

s. All the RDPA PFCS are covered with a thick layer of bubble wrap packing to avoid any damage to the PFCS in the next disassembly steps.

t. The 3 M5 screws responsible for holding the Shapal® electrical insulation in between the titanium structure and the shaft are unscrewed with a torque meter screwdriver. It must be checked that the applied torque was still above $5\ Nm$.

u. The titanium structure is now rotated 180 degrees in order to have the RDPA beam touching the flange previously disconnected and the RDPA pole touching the bearing supports. During the rotation, the bending radius of the Thermocoax® cables must always be larger than a few centimeters in order to avoid fatigue failure of the cables.

v. The titanium structure (covered with bubble wrap packing at this point) is tied to the bearings support with electrical scotch tape.

w. Unscrew the 6 screws connecting the motor moving part to the vacuum assembly. Collect the 6 glass reinforced epoxy washers and the star shaped PEEK insulation. The 6 PEEK tubes in the stainless steel connection part have been forced in place and are not supposed to move.

x. WARNING DANGEROUS STEP: Two people can manually lift the vacuum assembly out of the RDPA aluminum structure and place it onto a cart. The vacuum assembly is quite heavy $\approx 20\ kg$ and could quickly hurt someone or being damaged if dropped on the floor. Do not hesitate to use a fork lifter to bring it down to a cart.

A.2 RDPA disassembly in the vacuum workshop

a. Remove all the graphite PFCS on the RPDA pole. In order to do so, unscrew the 2 M4 screws with a torque meter screw driver. It must be checked that the applied torque was still above 2.5 Nm.

b. In the process of removing the pole graphite PFCS, mica spacers, silicon nitride rods and two stainless steel spacers will fall off. They should be collected and stored for the next assembly. Using a white piece of paper on the table enables to clearly see all the mica spacers.

c. Unscrew the 8 stainless steel M2 screws on the vertical bar in the titanium structure in order to release 2 Macor® insulation parts. This step will free the Thermocoax® cables from the titanium structure throughout the pole. The cable will still be held in place by the beam.

d. Unscrew the flange of the SMA vacuum feedthrough and pull the Thermocoax® cables on 30 cm in order to get access to the vacuum side of the SMA vacuum feedthrough.

e. A M8 modified open end wrench is used to disconnect the SMA connectors from the feedthrough.

f. Warning: delicate step. The Thermocoax® cables are now pulled once at a time out of the RDPA shaft. This step is delicate since the SMA connectors often get stuck due to the interweaving of Thermocoax® cables inside the shaft. Applying force would make the problem worse by bending the Thermocoax® cables and reinforcing the interweaving process.

g. The titanium structure with the Thermocoax® cables are now free from the vacuum assembly and are mounted on a table using a thick wooden piece and two clamps, one attached to the table and the other to the lower part of the titanium structure.

h. The RDPA beam can now be disassembled by unscrewing 4 M5 screws from the side graphite PFCS with a torque meter screw driver on one side of the beam. It must be checked that the applied torque was still above 0.25 Nm. The beam side disassembled should be close to the vertical pole in order to be able to remove the bridge mica insulation through the vertical slits. The beam side mica sheet will fall after unscrewing the side graphite PFCS. Collect it for future assembly.

i. The first Bridge boron nitride PFC can be slid out, dragging the graphite tips, the spring contactors and the inter graphite tips mica insulation along. The first side boron nitride PFCs can be slid out right after.

j. Warning: delicate step. The bridge mica insulation can only be removed from the vertical slits in the titanium structure after bending the copper connectors upward. The process must be gentle in order to avoid any damage to the copper connectors or to the inner conductor of the Thermocoax® cable. In the case of a failure, reparation is often possible (see next steps). Once the bridge mica insulation is removed, the copper connectors must be bent to their original orientation in the horizontal plane in order to permit motion for the bridge boron nitride PFCS.

k. Repeat the last two steps until disassembly is completed.

l. The copper connectors at the end of the Thermocoax® cables can be repaired or silver brazed after being properly tied in place by using thin copper wire. Doing the reparation on the titanium structure is less time-consuming than unfastening all the Thermocoax® cables and repairing them one at a time.

A.3 RDPA assembly in the vacuum workshop

a. Clean all parts with isopropanol.

b. Clean the vacuum bellow in the ultrasound ethanol bath (impossible to clean it from the outside). Cleaning is not necessary if the probe has been kept in a cleaned environment after disassembly.

c. Place the titanium horizontal part in the titanium structure with the two stainless steel shims on both sides. Mica sheets on both sides of the stainless steel shims ensure electrical insulation from the titanium structure. The stainless steel shims have a rectangular section with two chamfers. These chamfers must be oriented towards the mica sheets in order to avoid the possibility to generate any electrical arc in between the edges of the stainless steel shims and the titanium structure.

d. Place the 2 copper undulating shims in between the stainless steel shims and the Thermocoax® cables in order to push the cables toward the symmetry axis of the probe. This step will facilitate the next assembly steps.

e. Make sure that the titanium horizontal part is in contact with the bottom of the titanium structure. It the contact is not perfect, it will be impossible to slide in place the boron nitride plasma facing components. Placing custom made shims to force a good contact can facilitate the process but it is not mandatory to do so.

f. It is now time to slide in place all the components starting from the side of the beam next to

the vertical RDPA pole towards the side of the beam opposite to the vertical RDPA pole.

g. Warning: delicate step. The boron nitride plasma facing component will suffer wear from the friction with the titanium structure, with the copper conductors and with the Thermocoax® cables resulting in the formation of a white powder. This white boron nitride powder is not problematic to the diagnostic operation of to the TCV operation.

h. Warning: delicate step. Make sure the copper conductors at the end of the Thermocoax® cables are not interrupting the motion of the boron nitride plasma facing components. If it is the case, use a small instrument such as a fine spatula to temporarily bend the copper conductors at the end of the Thermocoax® cables.

i. Slide the first side boron nitride PFCS in place.

j. Place the spring contactors and the inter probe tips mica insulation. There is a risk to lose the spring contactors if they fall inside the titanium horizontal part. Placing small flexible plastic foam parts on the top of the holes is effective at avoiding the problem. The spring contactors should be placed in the middle of the copper connectors. Any movement will results in misalignments in between the spring contactors and the copper connectors.

k. Warning: delicate step. The graphite tips are forced below the side boron nitride plasma facing components. The graphite tips are held only from one side and will tip over. It is preferable in order not to avoid complete compression of the spring contactors. Sometimes the side boron nitride PFCS can break during the process. It seems like the mechanical failure is always catastrophic and the probability to generate hidden cracks during the assembly is low.

l. Warning: delicate step. Use a tool with a straight edge such as the flat side from a spatula to push on the horizontal part of the probe tips in order to compress the spring contactors. Hold the force while sliding the bridge boron nitride PFC in place. Remove the applied force once the bridge boron nitride PFC can hold the compressive force of the spring contactors.

m. Warning: delicate step. The bridge mica insulation can only be slid in place through the vertical slits in the titanium structure after bending the copper connectors upward. The process must be gentle in order to avoid any damage to the copper connectors or to the inner conductor of the Thermocoax® cable. In the case of a failure, reparation is often possible. Once the bridge mica insulation is removed, the copper connectors must be bent to their original orientation in the horizontal plane in order to permit motion for the bridge boron nitride PFCS.

n. Repeat the last 5 steps until assembly is completed.

o. Test the electrical properties of the lines before closing the beam. 5 values must be evaluated with the 4 points measurement device from the electronics lab at low frequency (100 Hz for example):

1. Resistance in between Mach probe tips should be higher than 1 $MOhm$.

2. Probe tips resistance to ground should be higher than 50 $kOhm$ (this resistance is only dependent on the moisture intake in the magnesium oxide powder in between the conductor and the sheath of the Thermocoax® cables).

3. Probe tips resistance to the titanium structure should be higher than 1 $MOhm$.

4. Probe tips resistance to the inner conductor of the corresponding SMA connector should be lower than 2 Ohm (a good contact with the copper spring is required in order to provide $R < 2\ Ohm$).

5. Titanium structure resistance to ground should be higher than 1 $MOhm$.

p. Use a file to plane the vertical face of the last bridge boron nitride PFC. Indeed it is important at the end of the assembly that the last part should be at the same position as the end of the titanium structure. In that case, there would not be any gap in between the side graphite PFCS and the last bridge boron nitride PFC.

q. Close the beam by screwing in place the 4 M2 screws onto the side graphite PFCS with a torque meter screw drive. At least 4 layers of Mica washers must be placed in between the screw and the side graphite PFCS. Make sure that the applied torque is 0.3 Nm. Make sure that the side graphite PFCS are levelled and make sure that there is proper contact in between the bridge boron nitride PFC and the side graphite PFCS.

r. Check the protruding height of each set of probe tips with a dial indicator. Write the values into a table in order to determine the probe surface and therefore the ion saturation current density [A/m2] during experiment with more accuracy.

s. Warning: delicate step. Straighten all the 24 Thermocoax® cables and separate them into 2 groups (1-12, 13-24) prior to insertion in the shaft. This step will facilitate disassembly if properly executed.

t. Connect the vacuum flange in between the vacuum bellow and the flange corresponding to the vacuum vessel extension.

u. Place the 3 copper rings (3 flanges below the vacuum bellow) around the Thermocoax® cables.

v. Connect the 24 SMA connectors on the vacuum side of the SMA feedthrough.

w. Tighten the 3 flanges below the vacuum bellow.

x. Bend the Thermocoax cables to conform the titanium structure shape and close again the Macor® insulator around the cable by screwing the 8 stainless steel M2 screws on the vertical bar in the titanium structure with a 0.3 Nm torque.

y. Place all the graphite PFCS on the vertical part of the titanium structure. The stainless steel spacers are placed first with the silicon nitride rods. The silicon nitride rods have various lengths. Make sure to choose them in order to obtain the proper length when they are put end to end. The graphite PFCS are slid in place once at a time interleaved with mica spacers. A proper clamp can be used to place the mica spacers because fingers are too large to access the limited space. Warning: when manipulating the mica spacers with the clamp make sure not to crack the edges of the mica spacers. Otherwise they could escape from the silicon nitride rods during operation. If such an event would happen, there is a risk that the whole assembly would become loose. The risk of losing a graphite PFCS would still remain very low. Visual inspection of the gap in between graphite PFCS enables to quickly know if a mica spacer has been forgotten.

z. Screw in place all the boron nitride PFCS, making sure that a tiny space is left in between them for thermal expansion. A stainless steel M2 washer must be placed in between the boron nitride PFCS and the titanium structure.

aa. The assembly is now ready to be covered with bubble wrap packing in order to be shipped to the TCV building.

A.4 RDPA assembly in TCV

In this section, the same steps as for the RDPA disassembly apply in reversed order. Nevertheless, two steps are different because they require a visual inspection of the adjustment before screwing RDPA in place:

a. Adjustment of the vertical alignment. A straight and rigid bar should be clamped to the vertical stainless steel part hosting the vacuum bearings. The titanium structure is screwed in place and the vertical alignment can be visually checked thanks to the rigid bar. Once the nominal torque is applied on the three M5 screws responsible for holding the Shapal® electrical insulation, the position is set and the rigid bar is no longer needed.

b. Adjustment of the rotational alignment. Once RDPA is in the TCV vacuum vessel, it is possible that the RDPA beam is not rotated properly (purely radial direction). A vacuum technician should check in the machine that the alignment is correct before using the RDPA motor.

A.5 Components relevant to RDPA operation

The SOLOIST controller $Hpe100$ is fed with a single phase from a 3 phase socket. Connecting all three phases will result in damaging the electronics since the controller can only work at $220VAC$ and not at three phases $380VAC$ (the three phase feed is designed for American three phase $240VAC$). It does not matter to use a single phase since the current is rectified and

stored in a capacitance inside the device.

The motor could not provide more than three plunges in a row with the following parameters: $a = 85\ m/s2\ v = 3\ m/s$ and $dx = 380\ mm$. It is possibly due to the limit of the capacitance in the controller. Increasing the current feed to US three phase 240 VAC with large current possibility ($\approx 50\ A$) could maybe help increasing both speed and acceleration? However a large transformer would be required.

A contactor has been put in order to cut the high voltage feed from the motor in case of emergency. The voltage is cut in the case where the 24 V safety line is interrupted (if someone removed a Plexiglas panel) or if the emergency button is pushed. The contactor has not been installed on the motor high voltage feed since this could lead to some damage to the power electronics of the controller.

The brake Brake Zimmer LCE 20 is controlled with the Soloist software with the command BRAKE ON and BRAKE OFF. When the controller is no longer fed with diagnostic voltage 220 VAC (normal socket), the brake will clamp the probe by default. Therefore one must turn on the voltage of the structure if motion is required, such as during the assembly.

The trigger is a +5 V on/off signal from the Langmuir cubicles 3 and 4. The longer on/off signal has been chosen because the TCV triggers are too fast to be detected by the J205 input of the Soloist controller. The trigger signal is at the torus ground, unlike RDPA motor and controller that are both at the building ground. This is not an issue because the differential input J205 of the controller is isolated. Moreover, an optical fiber has been installed for the trigger. During experiment, it is highly recommended to arm the motor ≈ 3 minutes before the shot in order to avoid any early trigger, e.g. triggers from diagnostic shots.

The linear encoder reads a scale and count the number of lines on the scale. At both ends of the scale, there are small magnets strongly glued with epoxy. These magnets will disable the motor if crossed. During operation at TCV, the magnetic limits can be disabled through the software, otherwise the magnetic field given by the central solenoid can trigger these limits. WARNING: these magnetic limits must be enabled in order to successfully home the motor with the HOME command in the beginning of the day for example. The limits are by default automatically turned on before the homing process by the software.

A.6 Software

List of software relevant to the RDPA operation installed on the RDPA PC: **Soloist digital scope**: similar to jScope, showing the results from the motor after the shot. **Soloist motion composer**: software to program and execute the movement.

When launching RDPA, use the connect button in both **Soloist digital scope** and **Soloist motion composer**. Check if the Ethernet connection is properly working because some Ethernet sockets are sometimes malfunctioning in the TCV control room.

List of programs written in the Aero-basic language that can be executed in **Soloist motion composer**: **GUI_interaction_ascii_2** : main program to execute the RDPA motion. **Check_CW_CCW_limits**: program to check that limits for magnets are turned on (commentary in the script).

GUI for the RDPA operation written in MATLAB language:

/home/oliveira/Matlab/12_RDPA_Control_GUI/RDPA_Control_GUI.m

Magnetic limits need to be disabled once motor has been homed. It is to avoid any false end of travel limit from the TCV magnetic field. This is done automatically when enabling motion with the GUI MATLAB script. When homing the motor, the CW/CCW limits should be on.

To do list to execute RDPA motion:

1. Start program GUI_interactive_ASCII_2 in Soloist motion composer.

2. Launch MATLAB GUI.

3. 'Enable motor' on the MATLAB GUI (RDPA head will go in machine, so don't do that during a shot).

4. 'Ping motor' to check the Ethernet connection with the Soloist.

5. Set distance, speed, acceleration (usually at the maximum values).

6. Step 4 : calculate and save plunge.

7. Step 5: save plunge time 1 ($t = 0$ s reference is equivalent to $t = 0$ s of the TCV shot).

8. Repeat the same sequence for plunge 2 and 3 if wanted.

9. Start shot procedure.

10. Confirm (GUI will then stop responding). If something needs to be changed after this step, the Aero-basic program and the MATLAB GUI must be stopped (requires improvement in the future).

11. After the shot, the system will send back data to be saved by the MATLAB script on MDS. Sometimes, the connection with SOLOIST fails, usually because LAC machines are highly used in the post shot process. In that case, the MATLAB GUI crashes and must be close. The data from **Soloist digital scope** should be exported and saved on MDS manually (requires improvement in the future). Writing the GUI in python language could possibly solve this issue.

12. To turn RDPA off : check that the motor 'pings' response is correct and click 'disable motor'. Check on **Soloist motion composer** that the brake is on, stop the program, lock the computer and turn off the screen.

Bibliography

[1] Jean-Marc Jancovici, "Éléments de base sur l'énergie au xxie siècle," 2019. https://jancovici.com/wp-content/uploads/2020/07/Jancovici_Mines_ParisTech_cours_1.pdf.

[2] M. Meinshausen, E. Vogel, A. Nauels, K. Lorbacher, N. Meinshausen, D. M. Etheridge, P. J. Fraser, S. A. Montzka, P. J. Rayner, C. M. Trudinger, P. B. Krummel, U. Beyerle, J. G. Canadell, J. S. Daniel, I. G. Enting, R. M. Law, C. R. Lunder, S. O'Doherty, R. G. Prinn, S. Reimann, M. Rubino, G. J. M. Velders, M. K. Vollmer, R. H. J. Wang, and R. Weiss, "Historical greenhouse gas concentrations for climate modelling (CMIP6)," *Geoscientific Model Development*, vol. 10, pp. 2057–2116, May 2017.

[3] J. M. Guinotte and V. J. Fabry, "Ocean acidification and its potential effects on marine ecosystems," *Annals of the New York Academy of Sciences*, vol. 1134, pp. 320–342, June 2008.

[4] Comité Suisse des Barrages, "La suisse, pays de barrages," 2020. http://www.swissdams.ch/fr/les-barrages/la-suisse-pays-de-barrages.

[5] P.-F. Bach, "Towards 50% wind electricity in denmark: Dilemmas and challenges," *The European Physical Journal Plus*, vol. 131, May 2016.

[6] Swiss Federal Office of Energy, "Large-scale hydropower," 2018. https://www.bfe.admin.ch/bfe/en/home/supply/renewable-energy/hydropower/large-scale-hydropower.html.

[7] IEA, "Energy storage more efforts needed tracking report - june 2020," 2020. https://www.iea.org/reports/energy-storage.

[8] World Nuclear Association, "Supply of uranium (updated december 2020)," 2020. https://www.world-nuclear.org/information-library/nuclear-fuel-cycle/uranium-resources/supply-of-uranium.aspx.

[9] World Nuclear Association, "Nuclear share figures, 2009-2019," 2020. https://www.world-nuclear.org/information-library/facts-and-figures/nuclear-generation-by-country.aspx.

[10] Afrikantov OKBM, "Sodium-cooled fast reactors," 2020. http://www.okbm.nnov.ru/en/business-directions/fast-neutron-reactors/.

[11] ANDRA, "Projet français de centre de stockage profond de déchets radioactifs.," 2020. https://www.andra.fr/cigeo.

[12] World Nuclear Association, "Nuclear power in germany," 2019. https://www.world-nuclear.org/information-library/country-profiles/countries-g-n/germany.aspx.

[13] B. R. Sehgal, "Light water reactor safety," in *Nuclear Safety in Light Water Reactors*, pp. 1–88, Elsevier, 2012.

[14] World Nuclear Association, "Uranium enrichment," 2020. https://www.world-nuclear.org/information-library/nuclear-fuel-cycle/conversion-enrichment-and-fabrication/uranium-enrichment.aspx.

[15] UKAEA, "Eddington's dream becoming reality: 100th anniversary of the discovery of solar fusion," 2020. https://ccfe.ukaea.uk/.

[16] Chemistry Libretexts, "25: Nuclear chemistry 25.6: Energetics of nuclear reactions," 2019. https://chem.libretexts.org/Bookshelves/General_Chemistry/.

[17] K. S. Krane, *Introductory Nuclear Physics*. Wiley, 1987.

[18] J. Wesson, *Tokamaks, fourth edition*. Oxford university press, 2011.

[19] Richard Rhodes, *Dark sun : the making of the hydrogen bomb*. New York : Simon and Schuster, 1996.

[20] J. B. Jason Parisi, *The Future of Fusion Energy*. World Scientific Publishing Europ Ltd., 2019.

[21] The New York Times, "Arthur r. kantrowitz, whose wide-ranging research had many applications, is dead at 95," 2008. https://www.nytimes.com/2008/12/09/science/09kantrowitz.html.

[22] W. Baumjohann and R. A. Treumann, *Basic Space Plasma Physics*. IMPERIAL COLLEGE PRESS, Mar. 2012.

[23] ITER, "Twist and fuse," 2015. https://www.iter.org/newsline/-/2314.

[24] Thomas Klinger, "Colloquium at cern: The long way to steady-state fusion plasma - the superconducting stellarator device wendelstein 7-x," 2016. https://indico.cern.ch/event/540787/attachments/1286722/1931349/CERN_W7X.pdf.

[25] ITER, "La fusion, une source d'Énergie durable," 2020. https://www.iter.org/fr/faq.

[26] G. Federici, W. Biel, M. Gilbert, R. Kemp, N. Taylor, and R. Wenninger, "European DEMO design strategy and consequences for materials," *Nuclear Fusion*, vol. 57, p. 092002, June 2017.

[27] MIT - Zach Hartwig, "Mit's pathway to fusion energy (iap 2017) - zach hartwig," 2017. https://library.psfc.mit.edu/catalog/online_pubs/iap/iap2017/hartwig.pdf.

[28] G. Federici, C. Bachmann, L. Barucca, W. Biel, L. Boccaccini, R. Brown, C. Bustreo, S. Ciattaglia, F. Cismondi, M. Coleman, V. Corato, C. Day, E. Diegele, U. Fischer, T. Franke, C. Gliss, A. Ibarra, R. Kembleton, A. Loving, F. Maviglia, B. Meszaros, G. Pintsuk, N. Taylor, M. Tran, C. Vorpahl, R. Wenninger, and J. You, "DEMO design activity in europe: Progress and updates," *Fusion Engineering and Design*, vol. 136, pp. 729–741, Nov. 2018.

[29] EURO fusion, "The demonstration power plant: Demo," 2021. https://www.euro-fusion.org/programme/demo/.

[30] RTS, "L'assemblage du gigantesque réacteur à fusion nucléaire iter a débuté en france," 2020. https://www.rts.ch/info/sciences-tech.

[31] R. Wenninger, M. Bernert, T. Eich, E. Fable, G. Federici, A. Kallenbach, A. Loarte, C. Lowry, D. McDonald, R. Neu, T. Pütterich, P. Schneider, B. Sieglin, G. Strohmayer, F. Reimold, and M. Wischmeier, "DEMO divertor limitations during and in between ELMs," *Nuclear Fusion*, vol. 54, p. 114003, Nov. 2014.

[32] R. Pitts, X. Bonnin, F. Escourbiac, H. Frerichs, J. Gunn, T. Hirai, A. Kukushkin, E. Kaveeva, M. Miller, D. Moulton, V. Rozhansky, I. Senichenkov, E. Sytova, O. Schmitz, P. Stangeby, G. D. Temmerman, I. Veselova, and S. Wiesen, "Physics basis for the first ITER tungsten divertor," *Nuclear Materials and Energy*, vol. 20, p. 100696, Aug. 2019.

[33] R. A. Pitts, R. Chavan, and J.-M. Moret, "The design of central column protection tiles for the TCV tokamak," *Nuclear Fusion*, vol. 39, pp. 1433–1449, Oct. 1999.

[34] K. L. Holtrop, G. L. Jackson, A. G. Kellman, R. L. Lee, and M. A. Hollerbach, "Operation of DIII-D with all-graphite walls," *Journal of Vacuum Science Technology*, vol. 12, pp. 1269–1274, July 1994.

[35] L. Spitzer, "The stellarator concept," *Physics of Fluids*, vol. 1, no. 4, p. 253, 1958.

[36] C. Theiler, B. Lipschultz, J. Harrison, B. Labit, H. Reimerdes, C. Tsui, W. A. J. Vijvers, J. A. Boedo, B. P. Duval, S. Elmore, P. Innocente, U. Kruezi, T. Lunt, R. Maurizio, F. Nespoli, U. Sheikh, A. J. Thornton, S. H. M. van Limpt, K. Verhaegh, N. Vianello, the TCV Team, and the EUROfusion MST1 Team, "Results from recent detachment experiments in alternative divertor configurations on TCV," *Nuclear Fusion*, vol. 57, p. 072008, July 2017.

[37] T. Eich, A. W. Leonard, R. A. Pitts, W. Fundamenski, R. J. Goldston, T. K. Gray, A. Herrmann, A. Kirk, A. Kallenbach, O. Kardaun, A. S. Kukushkin, B. LaBombard, R. Maingi, M. A. Makowski, A. Scarabosio, B. Sieglin, J. Terry, A. Thornton, ASDEX Upgrade Team,

and J. EFDA Contributors, "Scaling of the tokamak near the scrape-off layer H-mode power width and implications for ITER," *Nuclear Fusion*, vol. 53, p. 093031, Sept. 2013.

[38] P. C. Stangeby, *The Plasma Boundary of Magnetic Fusion Devices*. Series in Plasma Physics and Fluid Dynamics, Taylor and Francis, 2000.

[39] M. Greenwald, J. Terry, S. Wolfe, S. Ejima, M. Bell, S. Kaye, and G. Neilson, "A new look at density limits in tokamaks," *Nuclear Fusion*, vol. 28, pp. 2199–2207, Dec. 1988.

[40] B. Lipschultz, B. LaBombard, J. L. Terry, C. Boswell, and I. H. Hutchinson, "Divertor physics research on alcator c-mod," *Fusion Science and Technology*, vol. 51, pp. 369–389, Apr. 2007.

[41] H. Reimerdes, B. Duval, H. Elaian, A. Fasoli, O. Février, C. Theiler, F. Bagnato, M. Baquero-Ruiz, P. Blanchard, D. Brida, C. Colandrea, H. D. Oliveira, D. Galassi, S. Gorno, S. Henderson, M. Komm, B. Linehan, L. Martinelli, R. Maurizio, J.-M. Moret, A. Perek, H. Raj, U. Sheikh, D. Testa, M. Toussaint, C. Tsui, M. Wensing, the TCV team, and the EUROfusion MST1 team, "Initial TCV operation with a baffled divertor," *Nuclear Fusion*, vol. 61, p. 024002, Jan. 2021.

[42] H. Guo, D. Hill, A. Leonard, S. Allen, P. Stangeby, D. Thomas, E. Unterberg, T. Abrams, J. Boedo, A. Briesemeister, D. Buchenauer, I. Bykov, J. Canik, C. Chrobak, B. Covele, R. Ding, R. Doerner, D. Donovan, H. Du, D. Elder, D. Eldon, A. Lasa, M. Groth, J. Guterl, A. Jarvinen, E. Hinson, E. Kolemen, C. Lasnier, J. Lore, M. Makowski, A. McLean, B. Meyer, A. Moser, R. Nygren, L. Owen, T. Petrie, G. Porter, T. Rognlien, D. Rudakov, C. Sang, C. Samuell, H. Si, O. Schmitz, A. Sontag, V. Soukhanovskii, W. Wampler, H. Wang, and J. Watkins, "Developing and validating advanced divertor solutions on DIII-d for next-step fusion devices," *Nuclear Fusion*, vol. 56, p. 126010, Sept. 2016.

[43] F. Hitzler, M. Wischmeier, F. Reimold, D. P. Coster, and The ASDEX Upgrade Team, "Impurity transport and divertor retention in Ar and N seeded SOLPS 5.0 simulations for ASDEX Upgrade," *Plasma Physics and Controlled Fusion*, vol. 62, p. 085013, Aug. 2020.

[44] S. I. Krasheninnikov, M. Rensink, T. D. Rognlien, A. S. Kukushkin, J. A. Goetz, B. LaBombard, B. Lipschultz, J. L. Terry, and M. Umansky, "Stability of the detachment front in a tokamak divertor," *Journal of Nuclear Materials*, vol. 266, pp. 251–257, Jan. 1999.

[45] C. S. Pitcher and P. C. Stangeby, "REVIEW ARTICLE: Experimental divertor physics," *Plasma Physics and Controlled Fusion*, vol. 39, pp. 779–930, June 1997.

[46] S. I. Krasheninnikov, A. S. Kukushkin, W. Lee, A. A. Phsenov, R. D. Smirnov, A. I. Smolyakov, A. A. Stepanenko, and Y. Zhang, "Edge and divertor plasma: detachment, stability, and plasma-wall interactions," *Nuclear Fusion*, vol. 57, p. 102010, Oct. 2017.

[47] S. Coda, M. Agostini, R. Albanese, S. Alberti, E. Alessi, S. Allan, J. Allcock, R. Ambrosino, H. Anand, Y. Andrèbe, H. Arnichand, F. Auriemma, J. M. Ayllon-Guerola, F. Bagnato,

J. Ball, M. Baquero-Ruiz, A. A. Beletskii, M. Bernert, W. Bin, P. Blanchard, T. C. Blanken, J. A. Boedo, O. Bogar, T. Bolzonella, F. Bombarda, N. Bonanomi, F. Bouquey, C. Bowman, D. Brida, J. Bucalossi, J. Buermans, H. Bufferand, P. Buratti, G. Calabró, L. Calacci, Y. Camenen, D. Carnevale, F. Carpanese, M. Carr, L. Carraro, A. Casolari, F. Causa, J. Čeřovský, O. Chellaï, P. Chmielewski, D. Choi, N. Christen, G. Ciraolo, L. Cordaro, S. Costea, N. Cruz, A. Czarnecka, A. Dal Molin, P. David, J. Decker, H. De Oliveira, D. Douai, M. B. Dreval, B. Dudson, M. Dunne, B. P. Duval, T. Eich, S. Elmore, O. Embréus, B. Esposito, M. Faitsch, M. Farník, A. Fasoli, N. Fedorczak, F. Felici, S. Feng, X. Feng, G. Ferró, O. Février, O. Ficker, A. Fil, M. Fontana, L. Frassinetti, I. Furno, D. S. Gahle, D. Galassi, K. Gałązka, A. Gallo, C. Galperti, S. Garavaglia, J. Garcia, M. Garcia-Muñoz, A. J. Garrido, I. Garrido, J. Gath, B. Geiger, G. Giruzzi, M. Gobbin, T. P. Goodman, G. Gorini, M. Gospodarczyk, G. Granucci, J. P. Graves, M. Gruca, T. Gyergyek, A. Hakola, T. Happel, G. F. Harrer, J. Harrison, E. Havlíčková, J. Hawke, S. Henderson, P. Hennequin, L. Hesslow, D. Hogeweij, J. P. Hogge, C. Hopf, M. Hoppe, J. Horáček, Z. Huang, A. Hubbard, A. Iantchenko, V. Igochine, P. Innocente, C. Ionita Schrittwieser, H. Isliker, R. Jacquier, A. Jardin, A. Kappatou, A. Karpushov, P. V. Kazantzidis, D. Keeling, N. Kirneva, M. Komm, M. Kong, J. Kovacic, N. Krawczyk, O. Kudlacek, T. Kurki-Suonio, R. Kwiatkowski, B. Labit, E. Lazzaro, B. Linehan, B. Lipschultz, X. Llobet, R. Lombroni, V. P. Loschiavo, T. Lunt, E. Macusova, J. Madsen, E. Maljaars, P. Mantica, M. Maraschek, C. Marchetto, A. Marco, A. Mariani, C. Marini, Y. Martin, F. Matos, R. Maurizio, B. Mavkov, D. Mazon, P. McCarthy, R. McDermott, V. Menkovski, A. Merle, H. Meyer, D. Micheletti, F. Militello, K. Mitosinkova, J. Mlynář, V. Moiseenko, P. A. Molina Cabrera, J. Morales, J. M. Moret, A. Moro, R. T. Mumgaard, V. Naulin, R. D. Nem, F. Nespoli, A. H. Nielsen, S. K. Nielsen, M. Nocente, S. Nowak, N. Offeddu, F. P. Orsitto, R. Paccagnella, A. Palha, G. Papp, A. Pau, R. O. Pavlichenko, A. Perek, V. Pericoli Ridolfini, F. Pesamosca, V. Piergotti, L. Pigatto, P. Piovesan, C. Piron, V. Plyusnin, E. Poli, L. Porte, G. Pucella, M. E. Puiatti, T. Pütterich, M. Rabinski, J. Juul Rasmussen, T. Ravensbergen, M. Reich, H. Reimerdes, F. Reimold, C. Reux, D. Ricci, P. Ricci, N. Rispoli, J. Rosato, S. Saarelma, M. Salewski, A. Salmi, O. Sauter, M. Scheffer, C. Schlatter, B. S. Schneider, R. Schrittwieser, S. Sharapov, R. R. Sheeba, U. Sheikh, R. Shousha, M. Silva, J. Sinha, C. Sozzi, M. Spolaore, L. Stipani, P. Strand, T. Tala, A. S. Tema Biwole, A. A. Teplukhina, D. Testa, C. Theiler, A. Thornton, G. Tomaž, M. Tomes, M. Q. Tran, C. Tsironis, C. K. Tsui, J. Urban, M. Valisa, M. Vallar, D. Van Vugt, S. Vartanian, O. Vasilovici, K. Verhaegh, L. Vermare, N. Vianello, E. Viezzer, W. A. J. Vijvers, F. Villone, I. Voitsekhovitch, N. M. T. Vu, N. Walkden, T. Wauters, M. Weiland, H. Weisen, M. Wensing, M. Wiesenberger, G. Wilkie, M. Wischmeier, K. Wu, M. Yoshida, R. Zagorski, P. Zanca, J. Zebrowski, A. Zisis, and M. Zuin, "Physics research on the TCV tokamak facility: from conventional to alternative scenarios and beyond," *Nuclear Fusion*, vol. 59, p. 112023, Nov. 2019.

[48] A. Fasoli, H. Reimerdes, S. Alberti, M. Baquero-Ruiz, B. P. Duval, E. Havlikova, A. Karpushov, J. M. Moret, M. Toussaint, H. Elaian, M. Silva, C. Theiler, D. Vaccaro, and the TCV team, "TCV heating and divertor upgrades," *Nuclear Fusion*, vol. 60, p. 016019, Jan. 2020.

[49] R. A. Pitts, B. P. Duval, A. Loarte, J. M. Moret, J. A. Boedo, D. Coster, I. Furno, J. Horacek, A. S. Kukushkin, D. Reiter, J. Rommers, and TCV Team, "Divertor geometry effects on detachment in TCV," *Journal of Nuclear Materials*, vol. 290-293, pp. 940–946, Mar. 2001.

[50] H. Reimerdes, B. P. Duval, J. R. Harrison, B. Labit, B. Lipschultz, T. Lunt, C. Theiler, C. K. Tsui, K. Verhaegh, W. A. J. Vijvers, J. A. Boedo, G. Calabro, F. Crisanti, P. Innocente, R. Maurizio, V. Pericoli, U. Sheikh, M. Spolare, N. Vianello, the TCV Team, and the EUROfusion MST1 Team, "TCV experiments towards the development of a plasma exhaust solution," *Nuclear Fusion*, vol. 57, p. 126007, Dec. 2017.

[51] O. Février, C. Theiler, H. De Oliveira, B. Labit, N. Fedorczak, and A. Baillod, "Analysis of wall-embedded Langmuir probe signals in different conditions on the Tokamak à Configuration Variable," *Review of Scientific Instruments*, vol. 89, p. 053502, May 2018.

[52] B. LaBombard and L. Lyons, "Mirror Langmuir probe: A technique for real-time measurement of magnetized plasma conditions using a single Langmuir electrode," *Review of Scientific Instruments*, vol. 78, pp. 073501–073501–9, July 2007.

[53] J. A. Boedo, N. Crocker, L. Chousal, R. Hernandez, J. Chalfant, H. Kugel, P. Roney, J. Wertenbaker, and NSTX Team, "Fast scanning probe for the NSTX spherical tokamak," *Review of Scientific Instruments*, vol. 80, pp. 123506–123506–10, Dec. 2009.

[54] C. K. Tsui, J. A. Boedo, P. C. Stangeby, and TCV Team, "Accounting for Debye sheath expansion for proud Langmuir probes in magnetic confinement fusion plasmas," *Review of Scientific Instruments*, vol. 89, p. 013505, Jan. 2018.

[55] D. Brunner, A. Q. Kuang, B. LaBombard, and W. Burke, "Linear servomotor probe drive system with real-time self-adaptive position control for the alcator c-mod tokamak," *Review of Scientific Instruments*, vol. 88, p. 073501, July 2017.

[56] J. Bak, R. Pitts, H. Kim, H. Lee, C. Bin, J. Juhn, S. Hong, O. Garcia, R. Kube, and D. Seo, "Measurement of inner wall limiter sol widths in kstar tokamak," *Nuclear Materials and Energy*, vol. 12, pp. 1270 – 1276, 2017. Proceedings of the 22nd International Conference on Plasma Surface Interactions 2016, 22nd PSI.

[57] C. K. Tsui, J. A. Boedo, J. R. Myra, B. Duval, B. Labit, C. Theiler, N. Vianello, W. A. J. Vijvers, H. Reimerdes, S. Coda, O. Février, J. R. Harrison, J. Horacek, B. Lipschultz, R. Maurizio, F. Nespoli, U. Sheikh, K. Verhaegh, N. Walkden, and and, "Filamentary velocity scaling validation in the TCV tokamak," *Physics of Plasmas*, vol. 25, p. 072506, July 2018.

[58] B. LaBombard, T. Golfinopoulos, J. L. Terry, D. Brunner, E. Davis, M. Greenwald, and J. W. H. and, "New insights on boundary plasma turbulence and the quasi-coherent mode in alcator c-mod using a mirror langmuir probe," *Physics of Plasmas*, vol. 21, p. 056108, May 2014.

[59] J. Gunn, J. Stöckel, J. Adámek, I. Ďuran, J. Horáček, M. Hron, K. Jakubka, L. Kryška, F. Žáček, and G. van Oost, "Direct Measurements of E×B Flow and Its Impact on Edge

Turbulence in the CASTOR Tokamak Using an Optimized Gundestrup Probe," *Czechoslovak Journal of Physics*, vol. 51, pp. 1001–1010, Oct. 2001.

[60] R. Maurizio, S. Elmore, N. Fedorczak, A. Gallo, H. Reimerdes, B. Labit, C. Theiler, C. Tsui, W. Vijvers, and and, "Divertor power load studies for attached l-mode single-null plasmas in TCV," *Nuclear Fusion*, vol. 58, p. 016052, Dec. 2017.

[61] M. Wensing, B. P. Duval, O. Février, A. Fil, D. Galassi, E. Havlickova, A. Perek, H. Reimerdes, C. Theiler, K. Verhaegh, M. Wischmeier, the EUROfusion MST1 team, and the TCV team, "SOLPS-ITER simulations of the TCV divertor upgrade," *Plasma Physics and Controlled Fusion*, vol. 61, p. 085029, Aug. 2019.

[62] H. Arnichand, Y. Andrebe, P. Blanchard, S. Antonioni, S. Couturier, J. Decker, B. P. Duval, F. Felici, C. Galperti, P. F. Isoz, P. Lavanchy, X. Llobet, B. Marlétaz, P. Marmillod, and J. Masur, "New capabilities of the incoherent Thomson scattering diagnostics in the TCV tokamak: divertor and real-time measurements," *Journal of Instrumentation*, vol. 14, p. C09013, Sept. 2019.

[63] K. Verhaegh, B. Lipschultz, B. P. Duval, A. Fil, M. Wensing, C. Bowman, and D. S. Gahle, "Novel inferences of ionisation and recombination for particle/power balance during detached discharges using deuterium Balmer line spectroscopy," *Plasma Physics and Controlled Fusion*, vol. 61, p. 125018, Dec. 2019.

[64] A. Perek, W. A. J. Vijvers, Y. Andrebe, I. G. J. Classen, B. P. Duval, C. Galperti, J. R. Harrison, B. L. Linehan, T. Ravensbergen, K. Verhaegh, M. R. de Baar, and E. M. T. TCV Team, "MANTIS: A real-time quantitative multispectral imaging system for fusion plasmas," *Review of Scientific Instruments*, vol. 90, p. 123514, Dec. 2019.

[65] B. L. Linehan, R. T. Mumgaard, M. Wensing, K. Verhaegh, Y. Andrebe, J. R. Harrison, B. P. Duval, C. Theiler, and TCV Team, "The multi-spectral imaging diagnostic," *Review of Scientific Instruments*, vol. 89, p. 103503, Oct. 2018.

[66] U. A. Sheikh, B. P. Duval, B. Labit, and F. Nespoli, "A novel carbon coating technique for foil bolometers," *Review of Scientific Instruments*, vol. 87, p. 11D431, Aug. 2016.

[67] P. Ricci, F. D. Halpern, S. Jolliet, J. Loizu, A. Mosetto, A. Fasoli, I. Furno, and C. Theiler, "Simulation of plasma turbulence in scrape-off layer conditions: the GBS code, simulation results and code validation," *Plasma Physics and Controlled Fusion*, vol. 54, p. 124047, Nov. 2012.

[68] H. D. Oliveira, P. Marmillod, C. Theiler, R. Chavan, O. Février, B. Labit, P. Lavanchy, B. Marlétaz, and R. A. Pitts, "Langmuir probe electronics upgrade on the tokamak à configuration variable," *Review of Scientific Instruments*, vol. 90, p. 083502, Aug. 2019.

[69] H. M. Mott-Smith and I. Langmuir, "The Theory of Collectors in Gaseous Discharges," *Physical Review*, vol. 28, pp. 727–763, Oct. 1926.

[70] I. H. Hutchinson, *Principles of Plasma Diagnostics*. Cambridge University Press, 2005.

[71] D. Brida, D. Silvagni, T. Eich, M. Faitsch, and P. McCarthy, "Role of electric currents for the SOL and divertor target heat fluxes in ASDEX Upgrade," *Plasma Physics and Controlled Fusion*, vol. 62, p. 105014, Oct. 2020.

[72] J. Marki, R. A. Pitts, T. Eich, A. Herrmann, J. Horacek, F. Sanchez, and G. Veres, "Sheath heat transmission factors on TCV," *Journal of Nuclear Materials*, vol. 363, pp. 382–388, June 2007.

[73] R. Chodura, "Plasma–wall transition in an oblique magnetic field," *Physics of Fluids*, vol. 25, no. 9, p. 1628, 1982.

[74] J. Loizu, P. Ricci, F. D. Halpern, and S. Jolliet, "Boundary conditions for plasma fluid models at the magnetic presheath entrance," *Physics of Plasmas*, vol. 19, p. 122307, Dec. 2012.

[75] J. P. Gunn, C. Boucher, B. L. Stansfield, and S. Savoie, "Flush-mounted probes in the divertor plates of tokamak de varennes," *Review of Scientific Instruments*, vol. 66, pp. 154–159, Jan. 1995.

[76] R. Chavan, R. Pitts, F. Hofmann, C. Hollenstein, J.-M. Moret, R. Rage, and G. Tonetti, "First wall components for the TCV tokamak," *Proceedings of the 17th Symposium on Fusion Technology, Rome, Italy, 14 - 18 September*, pp. 222–227, 1992.

[77] R. A. Pitts, S. Alberti, P. Blanchard, J. Horacek, H. Reimerdes, and P. C. Stangeby, "ELM driven divertor target currents on TCV," *Nuclear Fusion*, vol. 43, pp. 1145–1166, Oct. 2003.

[78] R. A. Pitts and P. C. Stangeby, "Experimental tests of Langmuir probe theory for strong magnetic fields," *Plasma Physics and Controlled Fusion*, vol. 32, pp. 1237–1248, Dec. 1990.

[79] M. Mitov, A. Bankova, M. Dimitrova, P. Ivanova, K. Tutulkov, N. Djermanova, R. Dejarnac, J. Stöckel, and T. K. Popov, "Electronic system for Langmuir probe measurements," in *Journal of Physics Conference Series*, vol. 356 of *Journal of Physics Conference Series*, p. 012008, Mar. 2012.

[80] W. Bussière, "Estimation of the burn-back rate in high breaking capacity fuses using fast imagery," *Journal of Physics D Applied Physics*, vol. 34, pp. 1007–1016, Mar. 2001.

[81] J. Boedo, G. Gunner, D. Gray, and R. Conn, "Robust Langmuir probe circuitry for fusion research," *Review of Scientific Instruments*, vol. 72, pp. 1379–1382, Feb. 2001.

[82] J.-M. Moret, B. Duval, H. Le, S. Coda, F. Felici, and H. Reimerdes, "Tokamak equilibrium reconstruction code LIUQE and its real time implementation," *Fusion Engineering and Design*, vol. 91, pp. 1–15, Feb. 2015.

[83] H. Weisen, F. Hofmann, M. J. Dutch, Y. Martin, A. Pochelon, J.-M. Moret, B. P. Duval, A. Hirt, J. B. Lister, C. Nieswand, R. A. Pitts, Z. A. Pietrzyk, M. Anton, R. Behn, G. Besson, F. Bühlmann, R. Chavan, D. Fasel, A. Favre, S. Franke, P. Isoz, P. Lavanchy, B. Joye, X. Llobet, P. Mandrin, B. Marletaz, P. Marmillod, J. C. Magnin, J.-M. Mayor, P. J. Paris, A. Perez, O. Sauter, W. van Toledo, G. Tonetti, M. Q. Tran, F. Troyon, and D. J. Ward, "Ohmic h-modes in the TCV tokamak," *Plasma Physics and Controlled Fusion*, vol. 38, pp. 1137–1148, Aug. 1996.

[84] F. Nespoli, H. Bufferand, M. Valentinuzzi, N. Fedorczak, G. Ciraolo, E. Serre, Y. Marandet, R. Maurizio, H. De Oliveira, B. Labit, M. Komm, M. Faitsch, and S. Elmore, "Application of a two-fluid two-point model to soledge2d-eirene simulations of tcv h-mode plasma," *Nuclear Materials and Energy*, vol. 18, pp. 29 – 34, 2019.

[85] R. Maurizio, B. Duval, B. Labit, H. Reimerdes, M. Faitsch, M. Komm, U. Sheikh, C. Theiler, and the TCV team and, "H-mode scrape-off layer power width in the TCV tokamak," *Nuclear Fusion*, vol. 61, p. 024003, Jan. 2021.

[86] H. De Oliveira, C. Theiler, H. Elaian, and TCV team, "A fast-reciprocating probe array for two-dimensional measurements in the divertor region of the tokamak à confi guration variable," *Submitted to Review of Scientific Instruments*, 2021.

[87] J. G. Watkins, J. Hunter, B. Tafoya, M. Ulrickson, R. D. Watson, R. A. Moyer, J. W. Cuthbertson, G. Gunner, R. Lehmer, P. Luong, D. N. Hill, M. Mascaro, J. I. Robinson, R. Snider, and R. Stambaugh, "Fast reciprocating Langmuir probe for the DIII-D divertor," *Review of Scientific Instruments*, vol. 68, pp. 373–376, Jan. 1997.

[88] M. Tsalas, N. Tsois, V. Rohde, J. Neuhauser, and ASDEX Upgrade Team, "Langmuir probe measurements in the lower x-point vicinity of the ASDEX Upgrade divertor," *Journal of Nuclear Materials*, vol. 337, pp. 751–755, Mar. 2005.

[89] C. S. Pitcher, H. S. Bosch, A. Carlson, C. Dorn, A. Field, A. Herrmann, J. Neuhauser, T. Richter, and W. Schneider, "First results with the in-vessel probe on ASDEX-Upgrade," Dec 1993.

[90] N. Asakura, S. Sakurai, N. Hosogane, M. Shimada, K. Itami, Y. Koide, and O. Naito, "Heat and particle transport of SOL and divertor plasmas in the W shaped divertor on JT-60U," *Nuclear Fusion*, vol. 39, pp. 1983–1994, Nov. 1999.

[91] J. A. Boedo, R. Lehmer, R. A. Moyer, J. G. Watkins, G. D. Porter, T. E. Evans, A. W. Leonard, and M. J. Schaffer, "Measurements of flows in the DIII-D divertor by Mach probes," *Journal of Nuclear Materials*, vol. 266, pp. 783–787, Jan. 1999.

[92] J. A. Boedo, M. J. Schaffer, R. Maingi, and C. J. Lasnier, "Electric field-induced plasma convection in tokamak divertors," *Physics of Plasmas*, vol. 7, pp. 1075–1078, Apr. 2000.

[93] S. J. Zweben, "Search for coherent structure within tokamak plasma turbulence," *Physics of Fluids*, vol. 28, pp. 974–982, Mar. 1985.

[94] S. Marsen, M. Otte, and F. Wagner, "Three Dimensional Structure of Turbulence in the WEGA Stellarator," *Contributions to Plasma Physics*, vol. 48, pp. 467–472, July 2008.

[95] M. Hubeny, D. Höschen, M. Rack, O. Neubauer, S. Bozhenkov, G. Czymek, B. Unterberg, R. König, D. Hathiramani, S. Brezinsek, and C. Linsmeier, "Diagnostic setup for the divertor manipulator at wendelstein 7-x," *Nuclear Materials and Energy*, vol. 18, pp. 77–81, 2019.

[96] M. Baquero-Ruiz, F. Avino, O. Chellai, A. Fasoli, I. Furno, R. Jacquier, F. Manke, and S. Patrick, "Dual Langmuir-probe array for 3D plasma studies in TORPEX," *Review of Scientific Instruments*, vol. 87, p. 113504, Nov. 2016.

[97] P. Manz, M. Ramisch, and U. Stroth, "Poloidal mode structure of long-distance correlation of fluctuations under strong e×b shear in the torsatron TJ-k," *Physics of Plasmas*, vol. 16, p. 042309, Apr. 2009.

[98] C. S. MacLatchy, C. Boucher, D. A. Poirier, and J. Gunn, "Gundestrup: A Langmuir/Mach probe array for measuring flows in the scrape-off layer of TdeV," *Review of Scientific Instruments*, vol. 63, pp. 3923–3929, Aug. 1992.

[99] N. Smick, B. Labombard, B. Lipschultz, J. Rice, K. Marr, R. McDermott, A. Ince-Cushman, and A. Graff, "Parallel and Perpendicular Plasma Flows in Alcator C-Mod," in *APS Division of Plasma Physics Meeting Abstracts*, vol. 50 of *APS Meeting Abstracts*, p. PP6.085, Nov. 2008.

[100] J. Horacek, R. A. Pitts, and J. P. Graves, "Overview of edge electrostatic turbulence experiments on TCV," *Czechoslovak Journal of Physics*, vol. 55, pp. 271–283, Mar. 2005.

[101] C. K. Tsui, D. A. Taussig, M. G. Watkins, R. L. Boivin, and P. C. Stangeby, "Swinging reciprocating Mach probes for the high field side scrape-off layer in DIII-Da)," *Review of Scientific Instruments*, vol. 83, p. 10D723, Oct. 2012.

[102] A. Gallo, N. Fedorczak, R. Maurizio, C. Theiler, S. Elmore, B. Labit, H. Reimerdes, F. Nespoli, P. Ghendrih, and T. Eich, "Effect of plasma geometry on divertor heat flux spreading: Monalisa simulations and experimental results from tcv," *Nuclear Materials And Energy*, vol. 12, pp. 6. 893–898, 2017.

[103] V. Barabash, M. Akiba, I. Mazul, M. Ulrickson, and G. Vieider, "Selection, development and characterisation of plasma facing materials for ITER," *Journal of Nuclear Materials*, vol. 233-237, pp. 718–723, Oct. 1996.

[104] R. Chavan, "A thermo-mechanical analysis of the central column tiles (TCV)," *Internal SPC report*, 1999.

[105] R. Behn, A. Alfier, S. Y. Medvedev, G. Zhuang, R. Pasqualotto, P. Nielsen, Y. Martin, and TCV Team, "Edge profiles of electron temperature and density during ELMy H-mode in ohmically heated TCV plasmas," *Plasma Physics and Controlled Fusion*, vol. 49, pp. 1289–1308, Aug. 2007.

[106] K. Lackner, S. Guenter, P. Lauber, G. Pautasso, B. Scott, and M. Tran, *Equilibrium and Macroscopic Stability of Tokamaks*. International Atomic Energy Agency (IAEA), International Atomic Energy Agency, 2012.

[107] E. L. Murphy and R. H. Good, "Thermionic emission, field emission, and the transition region," *Phys. Rev.*, vol. 102, pp. 1464–1473, Jun 1956.

[108] B. J. Stagg and T. T. Charalampopoulos, "Refractive indices of pyrolytic graphite, amorphous carbon, and flame soot in the temperature range 25 to 600c," *Combustion and Flame; (United States)*, 9 1993.

[109] G. Cappellini, G. Satta, M. Palummo, and G. Onida, "Optical properties of bn in cubic and layered hexagonal phases," *Phys. Rev. B*, vol. 64, p. 035104, Jun 2001.

[110] I. A. Morozov, R. A. Morozova, T. V. Dubovik, A. I. Itsenko, V. M. Panashenko, A. A. Rogozinskaya, V. S. Tsyganenko, and V. V. Lychko, "Investigation of hydrogen-thermal treatment influence on the properties of boron nitride based materials," in *Carbon Nanomaterials in Clean Energy Hydrogen Systems* (B. Baranowski, S. Y. Zaginaichenko, D. V. Schur, V. V. Skorokhod, and A. Veziroglu, eds.), (Dordrecht), pp. 461–466, Springer Netherlands, 2008.

[111] A. E. Järvinen, S. L. Allen, A. W. Leonard, A. G. McLean, A. L. Moser, T. D. Rognlien, and C. M. Samuell, "Role of Poloidal $\mathbf{E} \times \mathbf{B}$ Drift in Divertor Heat Transport in DIII-D," *arXiv e-prints*, p. arXiv:1909.09190, Sept. 2019.

[112] J. Gunn, C. Boucher, M. Dionne, I. Ďuran, V. Fuchs, T. Loarer, I. Nanobashvili, R. Pánek, J.-Y. Pascal, F. Saint-Laurent, J. Stöckel, T. V. Rompuy, R. Zagórski, J. Adámek, J. Bucalossi, R. Dejarnac, P. Devynck, P. Hertout, M. Hron, G. Lebrun, P. Moreau, F. Rimini, A. Sarkissian, and G. V. Oost, "Evidence for a poloidally localized enhancement of radial transport in the scrape-off layer of the tore supra tokamak," *Journal of Nuclear Materials*, vol. 363-365, pp. 484–490, June 2007.

[113] N. Smick, B. LaBombard, and I. Hutchinson, "Transport and drift-driven plasma flow components in the alcator c-mod boundary plasma," *Nuclear Fusion*, vol. 53, p. 023001, Jan. 2013.

[114] S. Krasheninnikov, "On scrape off layer plasma transport," *Physics Letters A*, vol. 283, pp. 368–370, May 2001.

[115] T. Rognlien, G. Porter, and D. Ryutov, "Influence of exb and gradb drift terms in 2-d edge sol transport simulations," *Journal of Nuclear Materials*, vol. 266-269, pp. 654–659, Mar. 1999.

[116] R. Pitts, J. Horacek, W. Fundamenski, O. Garcia, A. Nielsen, M. Wischmeier, V. Naulin, and J. J. Rasmussen, "Parallel SOL flow on TCV," *Journal of Nuclear Materials*, vol. 363-365, pp. 505–510, June 2007.

[117] N. Christen, C. Theiler, T. Rognlien, M. Rensink, H. Reimerdes, R. Maurizio, and B. Labit, "Exploring drift effects in TCV single-null plasmas with the UEDGE code," *Plasma Physics and Controlled Fusion*, vol. 59, p. 105004, Aug. 2017.

[118] M. Wensing, H. de Oliveira, J. Loizu, C. Colandrea, O. Février, S. Gorno, H. Reimerdes, C. Theiler, A. Smolders, B. Duval, C. Tsui, M. Wischmeier, D. Brida, S. Henderson, and M. Komm, "Experimental verification of x-point potential well formation in unfavorable magnetic field direction," *Nuclear Materials and Energy*, vol. 25, p. 100839, Dec. 2020.

[119] M. Wensing, J. Loizu, H. Reimerdes, B. Duval, M. Wischmeier, and the TCV teama, "X-point potential well formation in diverted tokamaks with unfavorable magnetic field direction," *Nuclear Fusion*, vol. 60, p. 054005, apr 2020.

[120] O. Fevrier, H. Reimerdes, C. Theiler, D. Brida, C. Colandrea, B. P. Duval, H. De Oliveira, D. Galassi, S. Gorno, S. Henderson, M. Komm, B. Labit, B. Linehan, L. Martinelli, A. Perek, H. Raj, U. Sheikh, C. K. Tsui, M. Wensing, the TCV team, and the Eurofusion MST1 team, "Divertor closure effects on the TCV boundary plasma," *Submitted to Nuclear Materials and Energy*, 2021.

[121] I. H. Hutchinson, "Oblique ion collection in the drift approximation: How magnetized Mach probes really work," *Physics of Plasmas*, vol. 15, p. 123503, Dec. 2008.

[122] A. E. Jaervinen, S. L. Allen, D. Eldon, M. E. Fenstermacher, M. Groth, D. N. Hill, A. W. Leonard, A. G. McLean, G. D. Porter, T. D. Rognlien, C. M. Samuell, and H. Q. Wang, "E ×B Flux Driven Detachment Bifurcation in the DIII-D Tokamak," *Physical Review Letters*, vol. 121, p. 075001, Aug. 2018.

[123] P. C. Stangeby and A. V. Chankin, "The ion velocity bohm chodura boundary condition at the entrance to the magnetic presheath in the presence of diamagnetic and exb drifts in the scrape-off layer," *Physics of Plasmas*, vol. 2, pp. 707–715, Mar. 1995.

[124] S. Krasheninnikov, A. Kukushkin, V. Pistunovich, and V. Pozharov, "Self-sustained oscillations in the divertor plasma," *Nuclear Fusion*, vol. 27, pp. 1805–1816, Nov. 1987.

[125] A. Kukushkin, S. Krasheninnikov, A. Pshenov, and D. Reiter, "Role of molecular effects in divertor plasma recombination," *Nuclear Materials and Energy*, vol. 12, pp. 984 – 988, 2017. Proceedings of the 22nd International Conference on Plasma Surface Interactions 2016, 22nd PSI.

[126] E. M. Hollmann, S. Brezinsek, N. H. Brooks, M. Groth, A. G. McLean, A. Y. Pigarov, and D. L. Rudakov, "Spectroscopic measurement of atomic and molecular deuterium fluxes in the DIII-D plasma edge," *Plasma Physics and Controlled Fusion*, vol. 48, pp. 1165–1180, Aug. 2006.

[127] K. Verhaegh, B. Lipschultz, B. P. Duval, O. Février, A. Fil, C. Theiler, M. Wensing, C. Bowman, D. S. Gahle, J. R. Harrison, B. Labit, C. Marini, R. Maurizio, H. de Oliveira,

H. Reimerdes, U. Sheikh, C. K. Tsui, N. Vianello, and W. A. J. Vijvers, "An improved understanding of the roles of atomic processes and power balance in divertor target ion current loss during detachment," *Nuclear Fusion*, vol. 59, p. 126038, Dec. 2019.

[128] B. Nold, T. T. Ribeiro, M. Ramisch, Z. Huang, H. W. Müller, B. D. Scott, U. Stroth, and the ASDEX Upgrade Team, "Influence of temperature fluctuations on plasma turbulence investigations with Langmuir probes," *New Journal of Physics*, vol. 14, p. 063022, June 2012.

[129] N. Mahdizadeh, F. Greiner, M. Ramisch, U. Stroth, W. Guttenfelder, C. Lechte, and K. Rahbarnia, "Comparison of Langmuir and emissive probes as diagnostics for turbulence studies in the low-temperature plasma of the torsatron TJ-K," *Plasma Physics and Controlled Fusion*, vol. 47, pp. 569–579, Apr. 2005.

[130] C. Theiler, I. Furno, A. Kuenlin, P. Marmillod, and A. Fasoli, "Practical solutions for reliable triple probe measurements in magnetized plasmas," *Review of Scientific Instruments*, vol. 82, p. 013504, Jan. 2011.

[131] N. Offeddu, W. Han, C. Theiler, T. Golfinopoulos, C. Galperti, B. Duval, J. Terry, and the TCV Team, "Plasma edge turbulence characterization using gas puff imaging on the tcv tokamak," *46th EPS Conference on Plasma Physics*, 2019.

[132] P. Paruta, P. Ricci, F. Riva, C. Wersal, C. Beadle, and B. Frei, "Simulation of plasma turbulence in the periphery of diverted tokamak by using the GBS code," *Physics of Plasmas*, vol. 25, p. 112301, Nov. 2018.

[133] M. Giacomin, L. Stenger, and P. Ricci, "Turbulence and flows in the plasma boundary of snowflake magnetic configurations," *Nuclear Fusion*, vol. 60, p. 024001, Jan. 2020.

Acknowledgements

This work was supported in part by the Swiss National Science Foundation. This work has been carried out within the framework of the EUROfusion Consortium and has received funding from the Euratom research and training program 2014 - 2018 and 2019 - 2020 under grant agreement No 633053. The views and opinions expressed herein do not necessarily reflect those of the European Commission.

Remerciements

J'aimerais remercier particulièrement mon superviseur de thèse Christian Theiler pour son aide, son partage de connaissances, et son soutien bienveillant tout au long du doctorat. Je voudrais remercier le jury de cette thèse, Paolo Ricci, Jaimie Gunn et Daniel Brunner, pour leur attention attribuée à la lecture de celle-ci. Je remercie également le reste de l'équipe scientifique proche pour leur travail et leur compagnie : Olivier, Sophie, Nico, Curdin, Harshita, Diego, Davide, Mirko, Cédric, Basil, Holger, Lorenzo, Arthur, Bryan, Benoît, Claudia, Umar, Roberto et Kevin.

Un remerciement pour les experts sur TCV et d'autres tokamaks qui m'ont donné de précieux conseils : René Chavan, Philippe Marmillod, Richard Pitts, Bryan Labombard, Dan Brunner et Theodore Golfinopoulos. J'aimerai aussi remercier l'équipe des ingénieurs du bureau de conception, de l'atelier et des services sans qui la conception et la fabrication de RDPA n'aurait pas été possible : Hammam, Jean-Marc T., Tibor, David, Christian M., Blaise, Severino, Pierre, Maxime, Pierre-François, Xavier, Mateusz, Stefano B., Omar, Damien, Steve, Thierry, Régis, Guillaume, Nelson et William.

Merci aux collègues du laboratoire avec qui j'ai interagit à plusieurs occasions et qui ont été toujours sympathiques avec moi, je pense à Edith, Jean-Marc M., Laurie, Stefano C., Stefano A., Yves, Ambrogio et Paolo. Merci à l'équipe de la cafétéria, particulièrement Ugo, Roxanne et Stéphane qui font un travail volontaire de qualité et ont pu financer les évènements comme la visite de ITER et la sortie au vélodrome de Aigle. Merci également aux organisateurs de ces sorties.

J'ai eu beaucoup de plaisir à discuter et à partager des apéritifs avec mes collègues de bureau, malheureusement la covid a eu raison de nos rassemblements tout au long de ma dernière année dans le laboratoire : Jérémy, Guillaume, Emmanuel, Noé, Mathilde, Arsène, Matteo, Oulfa, Dahye, Samuel, Sophie, Federico, Curdin, Lorenzo, Roberto, Himank et Filippo. Merci aux amis avec qui j'ai beaucoup rigolé et/ou beaucoup réfléchi : Paola, Justin, Hamish, Timothée, Dario, Hugo, Jean, Aylwin, Simon, André.

Finalement, le plus grand des remerciements est adressé à ma famille, mes parents, mon frère et mes grands-parents que j'aime très fort.

Remerciements

Lausanne, May 3, 2021 Hugo De Oliveira

Hugo DE OLIVEIRA
34 Avenue d'Echallens 1004, Lausanne, Switzerland
hugo74800@gmail.com
+33626671626
Born on the 20th of April 1992
French nationality

PHD student at EPFL

Professional experiences

2017-2021	PHD (ongoing) in physics at the Swiss research laboratory on plasmas and nuclear fusion (SPC). Design, fabrication and analysis of the results of a new prototype of electrostatic probe in the TCV nuclear fusion reactor: https://www.youtube.com/watch?v=_8yVmABXc_s https://www.youtube.com/watch?v=0DctagZXYp8&t=1275s
2016	4 months professional experience as a CNC machine adjuster at Minesco (CNC lathe) in Haute-Savoie, France.
2014-2015	6-month internship at the ABB research center located in Wettingen, Switzerland, within the electrical insulation department. Accelerated ageing tests performed on insulation material candidates for large motor windings.

Studies and degrees

2017-2021	PHD (ongoing) in physics at the Swiss Plasma Research Laboratory (SPC).
04.2016	Master in Materials Science and Engineering at EPFL. Master's project carried out at the SKKU University in South Korea in organic chemistry on the synthesis of plant-based polyester resin.
08.2013	Bachelor in Materials Science and Engineering from EPFL. Third year at KTH University in Sweden.

Technical competences:
Optimization and design of systems under thermal, mechanical and electrical constraints.
Analysis of large data samples and development of dedicated software.
Advanced knowledge in metallurgical processes, chemical processes and composite materials processing.
Software and programming:
C, Python, MATLAB.
Experience with both Windows and Linux environments.
Experiences with CAD software (Catia, Solid Edge, Inventor, Sketchup).
Languages:
French, English (fluent, several years in an English-speaking environment), German (basic knowledge, foreign language at school).

Hobbies

Manufacture of lightweight fast pedal boats in composite material and navigation on the lakes of my region: https://www.youtube.com/watch?v=F4xxHcaP6Bo

Participation in conferences

Presentation at the Joint Annual Meeting of SPS and ÖPG, 21 - 25 August 2017, Geneva: ¨ Reciprocating array of Langmuir probes for the divertor region in TCV tokamak¨.

Participation to the poster session of the 46th European Physical Society Conference on Plasma Physics, July 8 to 12, 2019, *¨Insights into divertor profiles from two-dimensional probe measurements on the TCV tokamak.* ¨ Price obtained for the second place in the EPL Research Video and Communication Skills Award 2019.

Invited talk at the High-Temperature Plasma Diagnostics Conference, December 14-17, 2020 *¨A compact, fast-moving probe array for full diagnostic coverage of the tokamak divertor region.* ¨

Oral contribution accepted for the 47th European Physical Society Conference on Plasma Physics, "Heat exhaust capabilities of the recently upgraded TCV divertor", reported to June 2021.

Published paper as first author

H. De Oliveira et al, Rev. Sci. Instrum. 90, 083502 https://doi.org/10.1063/1.5108876

H. De Oliveira et al, Rev. Sci. Instrum. 92, 043547 https://doi.org/10.1063/5.0043523

First author papers in progress

H. De Oliveira et al, in preparation for submission to Nucl. Fusion. ¨ *New insights on divertor parallel flows, ExB drifts, and fluctuations from in situ, two-dimensional probe measurement in the tokamak à configuration variable*¨

Published papers as co-author

O. Février et al, 2018 Rev. Sci. Instrum. 89 053502 https://doi.org/10.1063/1.5022459

K. Verhaegh et al, 2019 Nucl. Fusion 59 126038 https://doi.org/10.1088/1741-4326/ab4251

R. Maurizio et al, 2019 Nuclear Materials and Energy 19 372-377 https://doi.org/10.1016/j.nme.2019.03.020

F. Nespoli et al, 2019 Nuclear Materials and Energy 18 29-34 https://doi.org/10.1016/j.nme.2018.11.026

J. R. Harrison et al, 2019 Plasma Phys. Control. Fusion 61 065024 https://doi.org/10.1088/1361-6587/ab140e

N. Vianello et al, 2020 Nucl. Fusion 60 016001 https://doi.org/10.1088/1741-4326/ab423e

A. Smolders et al, 2020 Plasma Phys. Control. Fusion 62 125006 https://doi.org/10.1088/1361-6587/abbcc5

O. Février et al, 2020 Plasma Phys. Control. Fusion 62 035017 https://doi.org/10.1088/1361-6587/ab6b00

M. Wensing et al, 2020 Nuclear Materials and Energy 25 100839 https://doi.org/10.1016/j.nme.2020.100839

H. Reimerdes et al, 2021 Nucl. Fusion 61 024002 https://doi.org/10.1088/1741-4326/abd196

Ce document a été imprimé au Centre d’impression EPFL,
imprimerie climatiquement neutre, certifiée myClimate.